

COMPUTATIONAL PARAMETRIC ANALYSES OF ENERGY ABSORPTION  
CAPACITIES OF DIFFERENT LATTICE STRUCTURES

A THESIS SUBMITTED TO  
THE GRADUATE SCHOOL OF NATURAL AND APPLIED SCIENCES  
OF  
MIDDLE EAST TECHNICAL UNIVERSITY

BY

ISMAIL SAFA KARACA

IN PARTIAL FULFILLMENT OF THE REQUIREMENTS  
FOR  
THE DEGREE OF MASTER OF SCIENCE  
IN  
AEROSPACE ENGINEERING

DECEMBER 2024



Approval of the thesis:

**COMPUTATIONAL PARAMETRIC ANALYSES OF ENERGY  
ABSORPTION CAPACITIES OF DIFFERENT LATTICE STRUCTURES**

submitted by **ISMAIL SAFA KARACA** in partial fulfillment of the requirements for the degree of **Master of Science in Aerospace Engineering Department, Middle East Technical University** by,

Prof. Dr. Naci Emre Altun  
Dean, Graduate School of **Natural and Applied Sciences**

\_\_\_\_\_

Prof. Dr. Serkan Ozgen  
Head of Department, **Aerospace Engineering**

\_\_\_\_\_

Prof. Dr. Ercan Gürses  
Supervisor, **Aerospace Engineering, METU**

\_\_\_\_\_

**Examining Committee Members:**

Prof. Dr. Demirkan Çöker  
Aerospace Engineering, METU

\_\_\_\_\_

Prof. Dr. Ercan Gürses  
Aerospace Engineering, METU

\_\_\_\_\_

Assist. Prof. Dr. Görkem Eğemen Güloğlu  
Aerospace Engineering, METU

\_\_\_\_\_

Prof. Dr. Serdar Göktepe  
Civil Engineering, METU

\_\_\_\_\_

Assoc. Prof. Dr. Recep Muhammet Görgülüarslan  
Mechanical Engineering, TOBB ETU

\_\_\_\_\_

Date:06.12.2024

**I hereby declare that all information in this document has been obtained and presented in accordance with academic rules and ethical conduct. I also declare that, as required by these rules and conduct, I have fully cited and referenced all material and results that are not original to this work.**

Name, Surname: Ismail Safa Karaca

Signature :

## **ABSTRACT**

### **COMPUTATIONAL PARAMETRIC ANALYSES OF ENERGY ABSORPTION CAPACITIES OF DIFFERENT LATTICE STRUCTURES**

Karaca, Ismail Safa  
M.S., Department of Aerospace Engineering  
Supervisor: Prof. Dr. Ercan Gürses

December 2024, 140 pages

In this thesis study, the energy absorption capacities of three different lattice structures were calculated depending on variable parameters. The three lattice structures were created using hexagonal, re-entrant, and chiral unit cells. Five different parametric studies were conducted for each model by making thickness changes, angle changes of unit cells, and adding elements to unit cells. The first study engendered changes in the thickness of the horizontal and vertical edges relative to each other while keeping the weight in each model constant. The second and third studies were created by adding horizontal and vertical elements to the unit cells and changing their thickness, keeping the weight constant. In the fourth study, the angles of the unit cells were altered, and their thickness was kept constant. The weight remained steady in this case, but the relative density changed. In the fifth study, while the angles of the unit cells were changed, their thickness was also changed. In this case, while the weight varied from model to model, the relative density was kept constant.

Compression analyses of all created models were conducted in mode with ABAQUS/Explicit. Then, force-displacement and stress-strain curves of the structures are generated. The locking strains, critical stresses, and plateau stresses

were calculated from these curves. These values were then used to compare the energy absorption capacities for each structure, depending on the parameters. The Poisson's ratios at different strain values were computed, the effects of parameter changes on Poisson's ratios were examined, and the relationship between Poisson's ratios and energy absorption capacities was investigated.

The structures with the highest energy absorption capacities were identified for each model. Interestingly, in most cases, the structures with Poisson's ratio close to zero also have the highest energy absorption capacity. This finding has significant implications for designing and optimizing lattice structures for energy absorption.

**Keywords:** Auxetic Lattice Structure, Specific Energy Absorption, Plateau Stress, Locking Strain

## ÖZ

### **FARKLI KAFES YAPILARIN ENERJİ SOĞURMA KAPASİTELERİNİN HESAPLAMALI PARAMETRİK ANALİZİ**

Karaca, Ismail Safa

Yüksek Lisans, Havacılık ve Uzay Mühendisliği Bölümü

Tez Yöneticisi: Prof. Dr. Ercan Gürses

Aralık 2024 , 140 sayfa

Bu tez çalışmasında üç farklı kafes yapının enerji soğurma kapasiteleri değişken parametrelere bağlı olarak hesaplanmıştır. Kullanılan üç kafes yapısı altıgen, girintili ve kiral birim hücreler kullanılarak oluşturulmuştur. Her model için beş farklı parametrik çalışma yapılmış olup bu çalışmalar bölgesel kalınlık değişimlerinden, birim hücrelerin açı değişimlerinden ve birim hücrelere eleman eklenmesinden oluşturulmuştur. İlk çalışma her modeldeki ağırlık sabit tutularak yatay ve dikey kenarların kalınlıklarının birbirine göre değişimlerinden ortaya çıkmıştır. İkinci ve üçüncü çalışma yine ağırlık sabit tutularak birim hücrelere yatay ve dikey elemanlar ekleyip modelin bölgesel kalınlıklarının değişmesiyle oluşturulmuştur. Dördüncü çalışmada birim hücrelerin açıları değiştirilmiş, kalınlıkları sabit tutulmuştur. Bu durumda ağırlık sabit kalmıştır ancak bağıl yoğunluk değişmiştir. Beşinci çalışmada ise birim hücrelerin açıları değiştirilirken kalınlıkları da değiştirilmiştir. Bu durumda ise ağırlık modelden modele değişkenlik gösterirken bağıl yoğunluk sabit tutulmuştur.

Oluşturulan tüm modellerin sıkışma analizleri ABAQUS/Explicit yardımıyla yapılmış, analiz sonuçlarından yapıların tepki kuvvetleri ölçülmüştür. Ölçülen tepki

kuvvetlerinden yapıların gerilim-gerinim eğrileri çıkartılıp bu eğriler üzerinden yoğunlaşma gerinimleri, kritik gerilim değerleri ve plato gerilimleri hesaplanmıştır. Bu değerlerin sonucunda her yapı için enerji soğurma kapasiteleri parametrelere bağlı olarak karşılaştırılmıştır. Tepki kuvvetlerine ek olarak yapının farklı gerinim değerlerindeki Poisson oranları hesaplanmıştır. Parametre değişimlerinin Poisson oranlarına etkisi ve Poisson oranları ile enerji soğurma kapasiteleri arasındaki ilişki incelenmiştir.

Her model için enerji soğurma kapasitelerinin en yüksek olduğu yapılar çıkarılmıştır. Poisson oranı sıfıra yakın olan yapıların çoğu durumda aynı zamanda en yüksek enerji soğurma kapasitesine sahip olan yapılar olduğu orataya çıkmıştır. Latis yapıların enerji soğurma kapasitelerini arttırmak için bu sonuç önemli olacaktır.

Anahtar Kelimeler: Ökzetik Kafes Yapılar, Özgül Enerji Emilimi, Plato Gerilmesi, Yoğunlaşma Gerinimi



For My Beloved Family,

## ACKNOWLEDGMENTS

I would like to express my heartfelt thanks to Prof. Dr. Ercan Gürses for his valuable support, guidance, and mentorship during this study.

I would like to extend my appreciation for the constructive evaluation made by the thesis examining committee members and Prof. Dr. Cihan Tekođlu, as their feedback and assessment have significantly enriched the outcome of this thesis.

I am thankful to my family for their unwavering love, encouragement, and understanding. My deepest thanks go to my mother, Emine Karaca, my father, Burhan Karaca, and my sister, Merve Karaca, for their support and belief in my abilities.

I would like to thank my colleagues at Turkish Aerospace for their understanding. I am incredibly thankful to my lead engineer, Fırat Dođangün, and other employees of the KC&T team.

## TABLE OF CONTENTS

ABSTRACT . . . . .	v
ÖZ . . . . .	vii
ACKNOWLEDGMENTS . . . . .	x
TABLE OF CONTENTS . . . . .	xi
LIST OF TABLES . . . . .	xiv
LIST OF FIGURES . . . . .	xviii
LIST OF ABBREVIATIONS . . . . .	xxvii
LIST OF SYMBOLS . . . . .	xxviii
CHAPTERS	
1 INTRODUCTION . . . . .	1
1.1 Lattice Structures . . . . .	1
1.2 Literature Review . . . . .	8
1.3 The Outline of the Thesis . . . . .	23
2 COMPARISON STUDIES . . . . .	25
2.1 Introduction . . . . .	25
2.2 In-plane dynamic crushing of honeycombs—a finite element study . . . . .	25
2.3 In-plane dynamic crushing behavior and energy absorption of honeycombs with a novel type of multi-cells . . . . .	36

3	FINITE ELEMENT MODELS AND METHODS OF COMPUTATION . . .	41
3.1	Introduction . . . . .	41
3.2	Models . . . . .	41
3.2.1	Boundary Conditions for All Models . . . . .	44
3.2.2	Mesh Properties and Convergence Study . . . . .	47
3.2.3	Hexagonal Lattice Structures . . . . .	50
3.2.4	Re-entrant Lattice Structures . . . . .	56
3.2.5	Chiral Lattice Structures . . . . .	60
3.3	Methods of Computation . . . . .	66
3.3.1	Computation of Plateau Stress, EA, and SEA . . . . .	66
3.3.2	Computation of Poisson's Ratio . . . . .	70
4	RESULTS . . . . .	73
4.1	Introduction . . . . .	73
4.2	Results of Hexagonal Lattices . . . . .	75
4.3	Results of Re-entrant Lattices . . . . .	80
4.4	Results of Chiral Lattices . . . . .	83
5	CONCLUSION . . . . .	91
	REFERENCES . . . . .	95
A	RESULTS OF ALL PARAMETRIC MODELS . . . . .	97
A.1	Hexagonal Lattice . . . . .	98
A.2	Re-entrant Lattice . . . . .	103
A.3	Chiral Lattice . . . . .	108
B	ENERGY CONSERVATION AND SEA CALCULATION . . . . .	113

C	COMPUTATION OF POISSON RATIO FROM AREA AND AREA CHANGE OF DEFORMED SHAPE FOR THE PARAMETRIC HEXAGONAL STUDY . . . . .	117
D	EFFECT OF FRICTION COEFFICIENT ON PLATEAU STRESS AND SEA FOR HEXAGONAL BASE MODEL . . . . .	125
E	ELASTIC POISSON'S RATIOS OF UNIT CELLS . . . . .	127
F	COMPARISON OF EXPLICIT AND IMPLICIT ANALYZES FOR BASE HEXAGONAL MODEL . . . . .	133
G	ILLUSTRATION OF SOME DEFORMED HEXAGONAL LATTICES . . .	135

## LIST OF TABLES

### TABLES

Table 3.1	Properties of base hexagonal lattice . . . . .	51
Table 3.2	Properties of base re-entrant lattice . . . . .	56
Table 3.3	Properties of base chiral lattice . . . . .	61
Table 4.1	Model parameters and outputs of the first parametric study of the hexagonal lattice . . . . .	76
Table 4.2	Model parameters and outputs of the second parametric study of the hexagonal lattice . . . . .	77
Table 4.3	Model parameters and outputs of the third parametric study of the hexagonal lattice . . . . .	78
Table 4.4	Model parameters and outputs of the fourth parametric study of the hexagonal lattice . . . . .	79
Table 4.5	Model parameters and outputs of the fifth parametric study of the hexagonal lattice . . . . .	80
Table 4.6	Model parameters and outputs of the second parametric study of the re-entrant model . . . . .	81
Table 4.7	Model parameters and outputs of the fourth parametric study of the re-entrant model . . . . .	82
Table 4.8	Model parameters and outputs of the fifth parametric study of the re-entrant model . . . . .	83

Table 4.9 Model parameters and outputs of the second parametric study of the chiral model . . . . .	84
Table 4.10 Model parameters and outputs of the third parametric study of the chiral model . . . . .	85
Table 4.11 Model parameters and outputs of the fourth parametric study of the chiral model . . . . .	86
Table 4.12 Model parameters and outputs of the fifth parametric study of the chiral model . . . . .	87
Table A.1 Model parameters, SEA, and Poisson's ratio for 0.004, 0.015, 0.05, and 0.1 strains of the first parametric study of the hexagonal lattice . . . .	98
Table A.2 Model parameters, SEA, and Poisson's ratio for 0.004, 0.015, 0.05, and 0.1 strains of the second parametric study of the hexagonal lattice . . . .	99
Table A.3 Model parameters, SEA, and Poisson's ratio for 0.004, 0.015, 0.05, and 0.1 strains of the third parametric study of the hexagonal lattice . . . .	100
Table A.4 Model parameters, SEA, and Poisson's ratio for 0.004, 0.015, 0.05, and 0.1 strains of the fourth parametric study of the hexagonal lattice . . . .	101
Table A.5 Model parameters, SEA, and Poisson's ratio for 0.004, 0.015, 0.05, and 0.1 strains of the fifth parametric study of the hexagonal lattice . . . .	102
Table A.6 Model parameters, SEA, and Poisson's ratio for 0.004, 0.015, 0.05, and 0.1 strains of the first parametric study of the re-entrant lattice . . . .	103
Table A.7 Model parameters, SEA, and Poisson's ratio for 0.004, 0.015, 0.05, and 0.1 strains of the second parametric study of the re-entrant lattice . . . .	104
Table A.8 Model parameters, SEA, and Poisson's ratio for 0.004, 0.015, 0.05, and 0.1 strains of the third parametric study of the re-entrant lattice . . . .	105
Table A.9 Model parameters, SEA, and Poisson's ratio for 0.004, 0.015, 0.05, and 0.1 strains of the fourth parametric study of the re-entrant lattice . . . .	106

Table A.10 Model parameters, SEA, and Poisson's ratio for 0.004, 0.015, 0.05, and 0.1 strains of the fifth parametric study of the re-entrant lattice . . . . .	107
Table A.11 Model parameters, SEA, and Poisson's ratio for 0.004, 0.015, 0.05, and 0.1 strains of the first parametric study of the chiral lattice . . . . .	108
Table A.12 Model parameters, SEA, and Poisson's ratio for 0.004, 0.015, 0.05, and 0.1 strains of the second parametric study of the chiral lattice . . . . .	109
Table A.13 Model parameters, SEA, and Poisson's ratio for 0.004, 0.015, 0.05, and 0.1 strains of the third parametric study of the chiral lattice . . . . .	110
Table A.14 Model parameters, SEA, and Poisson's ratio for 0.004, 0.015, 0.05, and 0.1 strains of the fourth parametric study of the chiral lattice . . . . .	111
Table A.15 Model parameters, SEA, and Poisson's ratio for 0.004, 0.015, 0.05, and 0.1 strains of the fifth parametric study of the chiral lattice . . . . .	112
Table B.1 Energy values in milijoules of the base hexagonal model at different strains . . . . .	114
Table B.2 Energy values in milijoules of the base re-entrant model at different strains . . . . .	114
Table B.3 Energy values in milijoules of the base chiral model at different strains	114
Table C.1 Poisson's ratio calculation from area change for the models of the first parametric study of the hexagonal lattice . . . . .	119
Table C.2 Poisson's ratio calculation from area change for the models of the second parametric study of the hexagonal lattice . . . . .	120
Table C.3 Poisson's ratio calculation from area change for the models of the third parametric study of the hexagonal lattice . . . . .	120
Table C.4 Poisson's ratio calculation from area change for the models of the fourth parametric study of the hexagonal lattice . . . . .	121



Table C.5 Poisson’s ratio calculation from area change for the models of the fifth parametric study of the hexagonal lattice . . . . .	121
Table C.6 Area changes for 0.004, 0.015, 0.05, and 0.1 strains of the first parametric study of the hexagonal lattice . . . . .	122
Table C.7 Area changes for 0.004, 0.015, 0.05, and 0.1 strains of the fourth parametric study of the hexagonal lattice . . . . .	123
Table D.1 Effect of friction coefficient on Plateau Stress and SEA in hexagonal base model . . . . .	125
Table E.1 Analytical elastic Poisson’s ratio and Poisson’s ratio from unit cell analyses for hexagonal shape . . . . .	128
Table E.2 Analytical elastic Poisson’s ratio and Poisson’s ratio from unit cell analyses for hexagonal shape . . . . .	129
Table E.3 Poisson’s ratio from unit cell analyses for chiral shape . . . . .	130
Table F.1 Explicit and implicit analyzes results for the hexagonal base model at 0.02, 0.04, 0.16, and 0.2 strains . . . . .	133

## LIST OF FIGURES

### FIGURES

Figure 1.1	Honeycomb Structure from [2] . . . . .	2
Figure 1.2	Illustration of Cortical and Cancellous Bone from [3] . . . . .	3
Figure 1.3	Some types of lattice structures from [4]; (a) Foam structure, (b) Honeycomb structures, (c) Auxetic structure (d) Lattice structure arrangement, (e) Periodic lattice structure, (f) Gradient by cell size and (g) Gradient by lattice thickness, (h) Conformal lattice (i) Stochastic lattice structure, (j) Hybrid lattice (Gyroid + BCC) . . . . .	5
Figure 1.4	Stress-strain diagram of honeycombs from [5] . . . . .	7
Figure 1.5	Schematic diagrams of (a) conventional materials with a positive Poisson's ratio and (b) auxetic materials with a negative Poisson's ratio under tensile loading from [6] (Solid line and dash line respectively describe the materials before and after deformation). . . . .	8
Figure 1.6	Illustration of auxeticity for auxetic nails: (a) during push-in; (b) during pull-out. (The nails in grey and red colour represent the configurations of the nails before and after deformation, respectively) from [7]. . . . .	9
Figure 1.7	Bending characteristic of sandwich composite specimens. (a) Load-deflection curves; (b) the images of deformed configuration of each sandwich specimen at a deflection of 8 mm from [8]. . . . .	10

Figure 1.8	A) Schematic illustrating the SLS fabrication process and printed implants with geometry mimicking the rabbit IVD, B) The stress and deformation distribution within natural IVD, TPU-X and TPU-A under compression (the mid-sagittal plane of 3D analyses), C) The behavior of TPU-X and TPU-A under compression using a commercial lumbar disc herniation model from [9]. . . . .	11
Figure 1.9	A) Optical images showing TPU-X and TPU-A in compression, B) The Poisson's ratio of TPU-X and TPU-A during compression testing, C) The compressive stress-strain curves, D) The global energy absorption curves of TPU-X and TPU-A from [9]. . . . .	12
Figure 1.10	Schematic design of 2D auxetic unit cell (AU) (a) and honeycomb unitcell (HU) (b) from [10]. . . . .	13
Figure 1.11	An application of lightweight hybrid auxetic composite panels to improve the blast resistance of armoured vehicles and protective structures from [10]. . . . .	13
Figure 1.12	Designed structure in [11] . . . . .	14
Figure 1.13	Effects of geometry parameters $r_1$ and $t$ on: (a) specific energy absorption and (b) Poisson's ratio from [11] . . . . .	15
Figure 1.14	Effects of geometry parameters: (a) $r_5$ and $t$ on specific energy absorption and (b) $r_5$ and $r_1$ on Poisson's ratio from [11] . . . . .	16
Figure 1.15	Schematic illustrations of re-entrant honeycomb and hierarchical honeycombs. (a) RH. (b) RHH. (c) RHT from [12] . . . . .	16
Figure 1.16	SEA and Poisson's ratio with respect to strain curves of RH, RHH and RHT from [12]. . . . .	17
Figure 1.17	Unit cells of re-entrant (a), re-entrant diamond without cross-link (b), and re-entrant diamond with cross-link (c) geometries from [13]. . . . .	18

Figure 1.18	FE simulated stress–strain curves (a) and Poisson’s ratio (b) of re-entrant diamond structures with and without cross-link members from [13]. . . . .	19
Figure 1.19	(a) Stress–strain curves; (b) Poisson’s ratio of re-entrant diamond structures with cross-links for different diamond angles ( $\theta_2$ ) from [13]. . . . .	20
Figure 1.20	(a) Stress–strain curves; (b) Poisson’s ratio of re-entrant diamond structures with cross-links for different length ratios ( $L_2/L_1$ ) from [13]. . . . .	21
Figure 1.21	Unit cell of the octet truss lattice material from [14]. . . . .	22
Figure 2.1	FE model and a rigid impact plate used in the simulation of hexagonal lattice from [18] . . . . .	26
Figure 2.2	Comparison between Ruan et al. [18] and current study of crushing of honeycomb with thickness = 0.2 mm, impact velocity = 3.5 m/s . . . . .	27
Figure 2.3	Comparison between Ruan et al. [18] and current study of crushing of honeycomb with thickness = 0.2 mm, impact velocity = 14 m/s . . . . .	28
Figure 2.4	Comparison between Ruan et al. [18] and current study of crushing of honeycomb with thickness = 0.2 mm, impact velocity = 70 m/s . . . . .	29
Figure 2.5	Comparison between Ruan et al. [18] and current study of crushing of honeycomb with thickness = 0.5 mm, impact velocity = 14 m/s . . . . .	30
Figure 2.6	Comparison between Ruan et al. [18] and current study of crushing of honeycomb with thickness = 0.08 mm, impact velocity = 14 m/s . . . . .	31

Figure 2.7	Comparison of force-displacement, $h= 0.2$ mm, $v= 14$ m/s between the referenced study [18] and the current study . . . . .	32
Figure 2.8	Plateau stress change in the $x_1$ direction with the impact velocity with analyses of the current study . . . . .	34
Figure 2.9	Plateau stress change in the $x_1$ direction with the impact velocity with analyses of the referenced study [18] . . . . .	35
Figure 2.10	3D view of the numerical models from [20] . . . . .	36
Figure 2.11	Comparison of force results of circular lattice in compression with the studies of Wang et al. [21], and Zhang et al. [20] . . . . .	38
Figure 2.12	Comparison of stress-strain diagrams with the reference study [20]	39
Figure 3.1	Illustration of units of lattice structures . . . . .	42
Figure 3.2	Boundary condition of hexagonal lattice structure . . . . .	45
Figure 3.3	Boundary condition of fixed plate . . . . .	46
Figure 3.4	Boundary condition of moving plate . . . . .	46
Figure 3.5	Boundary condition of lattice structure . . . . .	47
Figure 3.6	SEA outputs of the three lattices according to element sizes . . . .	48
Figure 3.7	Mesh densities of the lattices . . . . .	49
Figure 3.8	Hexagonal lattice structure . . . . .	50
Figure 3.9	Sections of hexagonal lattice structure for vertical and horizontal thickness variation . . . . .	52
Figure 3.10	Sections of hexagonal lattice structure of the model with horizontal edges added . . . . .	53
Figure 3.11	Sections of hexagonal lattice structure for additional vertical edge thickness variation . . . . .	54

Figure 3.12	Difference of hexagonal lattice geometries with two different angles . . . . .	55
Figure 3.13	Re-entrant lattice structure . . . . .	56
Figure 3.14	Sections of re-entrant lattice structure for vertical and horizontal thickness variation . . . . .	57
Figure 3.15	Sections of re-entrant lattice structure for additional horizontal edge thickness variation . . . . .	58
Figure 3.16	Sections of re-entrant lattice structure for additional vertical edge thickness variation . . . . .	59
Figure 3.17	Difference of hexagonal geometries with two different angles . . .	60
Figure 3.18	Chiral lattice structure . . . . .	61
Figure 3.19	Sections of chiral lattice structure for vertical and horizontal thickness variation . . . . .	62
Figure 3.20	Sections of chiral lattice structure for additional horizontal edge thickness variation . . . . .	63
Figure 3.21	Sections of chiral lattice structure for additional vertical edge thickness variation . . . . .	64
Figure 3.22	Difference of chiral geometries with two different angles . . . . .	65
Figure 3.23	Stress strain diagram of the chiral angular model ( $145^\circ$ ) with thickness of 0.15 mm and its densification slopes, with limitation three locking strain correction is applied . . . . .	68
Figure 3.24	Stress strain diagram of the chiral angular model ( $145^\circ$ ) with thickness of 0.15 mm and its densification slopes, without limitation one locking strain correction is applied . . . . .	68
Figure 3.25	Plateau stress of the chiral angular model ( $145^\circ$ ) with thickness of 0.15 mm . . . . .	69

Figure 3.26	Nodes for Poisson's ratio calculation of hexagonal lattice . . . . .	71
Figure 4.1	Variation of Poisson's ratio of the hexagonal base model with strain . . . . .	74
Figure 4.2	Variation of Poisson's ratio and SEA values with the thickness change for the first parametric study of the hexagonal lattice . . . . .	76
Figure 4.3	Variation of Poisson's ratio and SEA values with the thickness change for the second parametric study of the hexagonal lattice . . . . .	77
Figure 4.4	Variation of Poisson's ratio and SEA values with the thickness change for the third parametric study of the hexagonal lattice . . . . .	78
Figure 4.5	Variation of Poisson's ratio and SEA values with the angle change for the fourth parametric study of the hexagonal lattice . . . . .	79
Figure 4.6	Variation of Poisson's ratio and SEA values with the angle change for the fifth parametric study of the hexagonal lattice . . . . .	80
Figure 4.7	Variation of Poisson's ratio and SEA values with the thickness change for the second parametric study of the re-entrant model . . . . .	81
Figure 4.8	Variation of Poisson's ratio and SEA values with the angle change for the fourth parametric study of the re-entrant model . . . . .	82
Figure 4.9	Variation of Poisson's ratio and SEA values with the angle change for the fifth parametric study of the re-entrant model . . . . .	83
Figure 4.10	Variation of Poisson's ratio and SEA values with the thickness change for the second parametric study of the chiral model . . . . .	84
Figure 4.11	Variation of Poisson's ratio and SEA values with the thickness change for the third parametric study of the chiral model . . . . .	85
Figure 4.12	Variation of Poisson's ratio and SEA values with the angle change for the fourth parametric study of the chiral model . . . . .	86

Figure 4.13	Variation of Poisson's ratio and SEA values with the angle change for the fifth parametric study of the chiral model . . . . .	87
Figure A.1	Variation of Poisson's ratio and SEA values with the thickness change for the first parametric study of the hexagonal lattice . . . . .	98
Figure A.2	Variation of Poisson's ratio and SEA values with the thickness change for the second parametric study of the hexagonal lattice . . . . .	99
Figure A.3	Variation of Poisson's ratio and SEA values with the thickness change for the third parametric study of the hexagonal lattice . . . . .	100
Figure A.4	Variation of Poisson's ratio and SEA values with the thickness change for the fourth parametric study of the hexagonal lattice . . . . .	101
Figure A.5	Variation of Poisson's ratio and SEA values with the thickness change for the fifth parametric study of the hexagonal lattice . . . . .	102
Figure A.6	Variation of Poisson's ratio and SEA values with the thickness change for the first parametric study of the re-entrant lattice . . . . .	103
Figure A.7	Variation of Poisson's ratio and SEA values with the thickness change for the second parametric study of the re-entrant lattice . . . . .	104
Figure A.8	Variation of Poisson's ratio and SEA values with the thickness change for the third parametric study of the re-entrant lattice . . . . .	105
Figure A.9	Variation of Poisson's ratio and SEA values with the thickness change for the fourth parametric study of the re-entrant lattice . . . . .	106
Figure A.10	Variation of Poisson's ratio and SEA values with the thickness change for the fifth parametric study of the re-entrant lattice . . . . .	107
Figure A.11	Variation of Poisson's ratio and SEA values with the thickness change for the first parametric study of the chiral lattice . . . . .	108
Figure A.12	Variation of Poisson's ratio and SEA values with the thickness change for the second parametric study of the chiral lattice . . . . .	109



Figure A.13	Variation of Poisson's ratio and SEA values with the thickness change for the third parametric study of the chiral lattice . . . . .	110
Figure A.14	Variation of Poisson's ratio and SEA values with the thickness change for the fourth parametric study of the chiral lattice . . . . .	111
Figure A.15	Variation of Poisson's ratio and SEA values with the thickness change for the fifth parametric study of the chiral lattice . . . . .	112
Figure C.1	Undeformed base hexagonal lattice . . . . .	117
Figure C.2	Base hexagonal lattice compressed by 0.2 strain . . . . .	118
Figure C.3	Geometric parameters related with the initial and deformed structure . . . . .	118
Figure E.1	Undeformed and deformed hexagonal unit cell at 0.005 strain . .	128
Figure E.2	Undeformed and deformed re-entrant unit cell at 0.005 strain . .	130
Figure E.3	Undeformed and deformed chiral unit cell at 0.005 strain . . . .	131
Figure G.1	Deformed geometry of the base hexagonal lattice . . . . .	135
Figure G.2	Deformed geometry of hexagonal lattice of the first parametric study with the inclined edge thickness of 0.397 mm . . . . .	136
Figure G.3	Deformed geometry of hexagonal lattice of the first parametric study with the inclined edge thickness of 0.446 mm . . . . .	136
Figure G.4	Deformed geometry of hexagonal lattice of the second parametric study with the additional edge thickness of 0.1 mm . . . . .	137
Figure G.5	Deformed geometry of hexagonal lattice of the second parametric study with the additional edge thickness of 0.25 mm . . . . .	137
Figure G.6	Deformed geometry of hexagonal lattice of the third parametric study with the additional edge thickness of 0.15 mm . . . . .	138

Figure G.7	Deformed geometry of hexagonal lattice of the third parametric study with the additional edge thickness of 0.475 mm . . . . .	138
Figure G.8	Deformed geometry of hexagonal lattice of the fourth parametric study with the angle of 70° . . . . .	139
Figure G.9	Deformed geometry of hexagonal lattice of the fourth parametric study with the angle of 90° . . . . .	139
Figure G.10	Deformed geometry of hexagonal lattice of the fifth parametric study with the angle of 70° . . . . .	140
Figure G.11	Deformed geometry of hexagonal lattice of the fifth parametric study with the angle of 90° . . . . .	140

## LIST OF ABBREVIATIONS

2D	2 Dimensional
3D	3 Dimensional
AU	2D Auxetic Unit Cell
BCC	Body-Centered Cubic
EA	Energy Absorption
EPPs	Conventional Honeycomb Panels
EPR	Effective Poisson's Ratio
FCC	Face-Centered Cubic
FE	Finite Element
HACPs	Hybrid Auxetic Composite Panels
HU	Honeycomb Unitcell
IVD	Inter-vertebral Disc
MDF	Medium Density Fiberboard
NPR	Negative Poisson's Ratio
RH	Re-entrant Honeycombs
RHH	Re-entrant Hierarchical Hexagonal
RHT	Re-entrant Hierarchical Triangular
SEA	Specific Energy Absorption
SLM	Selective Laser Melting
TPMS	Triply Periodic Minimal Surfaces

## LIST OF SYMBOLS

$A$	Deformed Area
$A_0$	Initial Area
$c_0$	Longitudinal Elastic Stress Wave Speed
$\Delta\rho - \bar{\rho}$	Relative Density
$\Delta A$	Area Change
$\delta_x$	Displacement in Lateral Direction
$\delta_y$	Displacement in Longitudinal Direction
$E_A$	Artificial Strain Energy
$E_{CD}$	Energy Dissipated by Viscoelasticity
$E_E$	Elastic Strain Energy
$E_{FD}$	Frictional Dissipated Energy
$E_I$	Internal Energy
$E_{KE}$	Kinetic Energy
$E_P$	Plastic Dissipated Energy
$E_{TOTAL}$	Total Energy
$E_V$	Viscous Dissipated Energy
$E_W$	External Work
$\epsilon$	Strain
$\epsilon_{cr}$	Critical Strain
$\epsilon_d$	Locking Strain
$\epsilon_y$	Yield Strain
$E_s$	Young's Modulus
$L_{0x}$	Initial Lateral Length

$L_{0y}$	Initial Longitudinal Length
$L_x$	Deformed Lateral Length
$L_y$	Deformed Longitudinal Length
$\lambda$	Coefficient of Locking Strain
$l_e$	Edge Length
$\nu$	Poisson's Ratio
$\rho_s$	Material Density
$\rho^*$	Volumetric Density of Cellular Unit Cell
$s$	Second
$\sigma$	Stress
$\sigma_0$	Static Plateau Stress
$\sigma_p$	Plateau Stress
$\sigma_y$	Yield Stress
$t_h$	Horizontal or Close to Horizontal Edge Thickness
$t_v$	Vertical or Close to Vertical Edge Thickness
$\theta$	Unit Angle
$v$	Compression Velocity
$\bar{V}$	Relative Velocity
$V_0$	Compression Speed
$V_y$	Yield Velocity
$x$	Lateral Direction
$y$	Longitudinal Direction
$z$	Out of Plane Direction



# CHAPTER 1

## INTRODUCTION

### 1.1 Lattice Structures

Energy absorption is a critical issue for protecting the structures of vehicles like aircraft and automobiles. For example, when an aircraft or a spacecraft touches the ground during landing, the landing gear system needs to absorb a certain amount of energy. However, weight is a parameter that seriously affects the vehicle's performance, especially in aviation structures. According to Schöder et al. [1], shock absorbers integrated into the landing legs handle the impact during touchdown for medium and large landers. However, alternative shock-reduction methods are necessary for smaller landers, as the landing gear becomes disproportionately heavy relative to the lander's size. Cellular structures are widely used to keep the weight constant or reduce it while increasing the energy absorption efficiency. In nature, there are a lot of examples of the cellular structure that are suitable for shock-reduction efficiency. The most famous examples are honeycombs and spongy bones. The honeycomb structure shown in Figure 1.1, composed of periodic thin-walled hollow cells, is a lightweight design inspired by nature and can be made from materials like aluminum, carbon, steel, and fiberglass. Referenced studies in Mohammadi et al. [2] conclude that it is highly effective for energy absorption, making it an excellent and cost-efficient choice for crashworthiness applications. The hexagonal cells in the honeycombs are incredibly efficient in terms of material usage while providing strength and rigidity. The hexagonal pattern allows the honeycomb to absorb energy and distribute loads evenly, which is crucial for the hive's stability and protection against external forces.



Figure 1.1: Honeycomb Structure from [2]

Spongy bones, also known as trabecular or cancellous bones, are found at the ends of long bones and in the vertebrae. It consists of a porous, lattice-like structure less dense than compact bone. The trabecular structure is designed to absorb shock and reduce the skeleton's weight while providing enough strength to support the body's load. This ability to absorb energy helps protect the bone from fractures during impacts. A demonstration of the difference between cancellous and cortical bone, which is the dense and rigid outer layer of bone tissue that forms the outer shell of most bones in the human body can be seen in Figure 1.2.



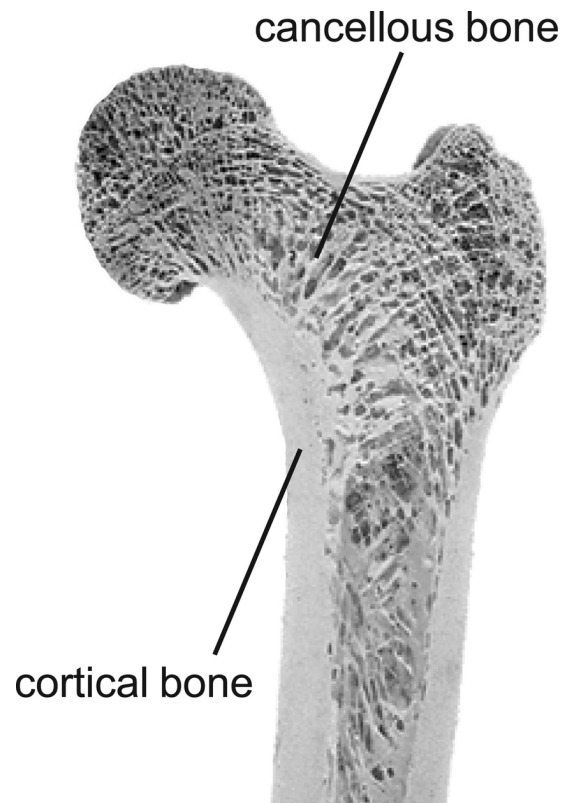


Figure 1.2: Illustration of Cortical and Cancellous Bone from [3]

A lattice structure is a geometric framework composed of a repetitive pattern of interconnected nodes and struts or beams, forming an open, cellular architecture. These structures can vary in complexity, ranging from simple cubic or hexagonal arrangements to more intricate designs with irregular or graded patterns. The defining characteristic of lattice structures is their regular, repeating units, which can be tailored to achieve specific mechanical properties, such as strength, stiffness, and lightweight efficiency.

Lattice structures are particularly valued in engineering and material science because they combine high strength with low weight. It makes them ideal for applications where minimizing material use while maximizing load-carrying capacity is critical. Additionally, the open-cell design of lattice structures allows them to show energy absorption ability, as they can deform in controlled ways under stress, effectively dissipating energy and reducing the force transmitted through the structure.

Energy absorption efficiency in lattice structures is primarily due to their ability to

undergo both elastic and plastic deformation. When a lattice structure is compressed, the struts or beams that make up the cells bend, buckle, or collapse, dissipating energy through these mechanisms. The specific pattern of the lattice, such as the size and shape of the cells, can be optimized to maximize energy absorption while maintaining structural integrity.

Lattice structures, designed for high strength-to-weight ratios, are categorized into foams, honeycombs, and lattice architectures in the review study of Khan and Riccio [4]. Foams consist of randomly oriented unit cells with high porosity, as seen in materials like cork and bone. Honeycombs feature uniform, extruded cells such as hexagonal prisms and include auxetic structures with a negative Poisson's ratio, enhancing stiffness and resistance to indentation. Lattice structures, distinguished by their periodic or pseudo-periodic arrangements, include gradients in size or thickness, conformal lattices adapting to part boundaries, stochastic lattices with random variations, and hybrid lattices combining different cell types for tailored properties. Unit cell topologies are further classified as strut-based, like BCC and FCC trusses, or surface-based, such as triply periodic minimal surfaces (TPMS) like Gyroid and Diamond, offering reduced stress concentrations and enhanced strength. Some types of lattice structures are shown in Figure 1.3. This diversity enables precise customization for applications demanding lightweight and high-performance designs, particularly in aerospace.

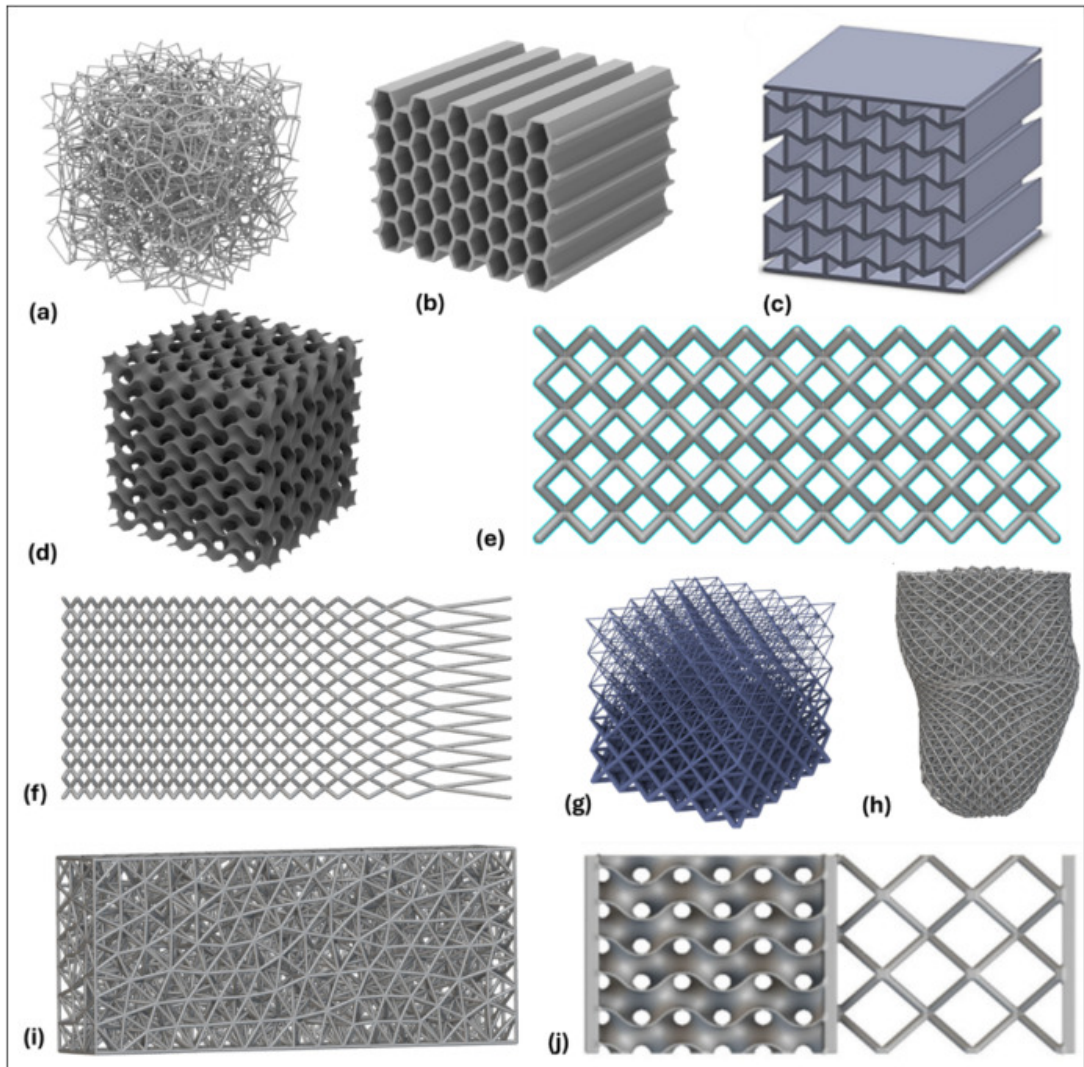


Figure 1.3: Some types of lattice structures from [4]; (a) Foam structure, (b) Honeycomb structures, (c) Auxetic structure (d) Lattice structure arrangement, (e) Periodic lattice structure, (f) Gradient by cell size and (g) Gradient by lattice thickness, (h) Conformal lattice (i) Stochastic lattice structure, (j) Hybrid lattice (Gyroid + BCC)

As mentioned in [4], recent advances in additive manufacturing, such as 3D printing, have significantly expanded the potential of lattice structures. These technologies enable the creation of complex geometries that were previously difficult or impossible to produce with traditional manufacturing methods. As a result, lattice structures can now be tailored with unprecedented precision, allowing for customized energy absorption characteristics tailored to specific applications.

Figure 1.4 shows the stress-strain diagram of any cellular structure.  $\sigma_p$  in Figure 1.4 is plateau stress refers to the relatively constant stress exhibited during the intermediate stages of deformation when the structure absorbs energy through mechanisms like strut buckling, bending, or collapse. This behavior is critical for ensuring controlled energy dissipation and minimizing force transmission during impact. The region where plateau stress is calculated, and the stress graph is considered relatively constant, is called the plateau region. The boundaries of this region are formed by critical strain and locking strain. Critical strain and locking strain are shown in Figure 1.4 as  $\epsilon_{cr}$  and  $\epsilon_d$  respectively. Locking strain is the strain level at which the structure transitions from the plateau phase to densification, where the cells collapse completely, causing a rapid increase in stress. This point marks the limit of effective energy absorption in the material. Critical strain, on the other hand, indicates the onset of significant deformation, typically when the structure begins to lose its load-bearing capacity. The region between critical strain and locking strain is where the majority of energy absorption occurs. Energy absorption (EA) quantifies the total energy dissipated by the structure during deformation derived from the area under the stress-strain curve. This parameter is essential for evaluating the effectiveness of lattice structures in mitigating impact forces. To compare the energy absorption capabilities of different geometries with different weights, energy absorption (EA) is divided by weight to give specific energy absorption (SEA). The calculation of EA and SEA is explained in detail in Section 3.3.1.

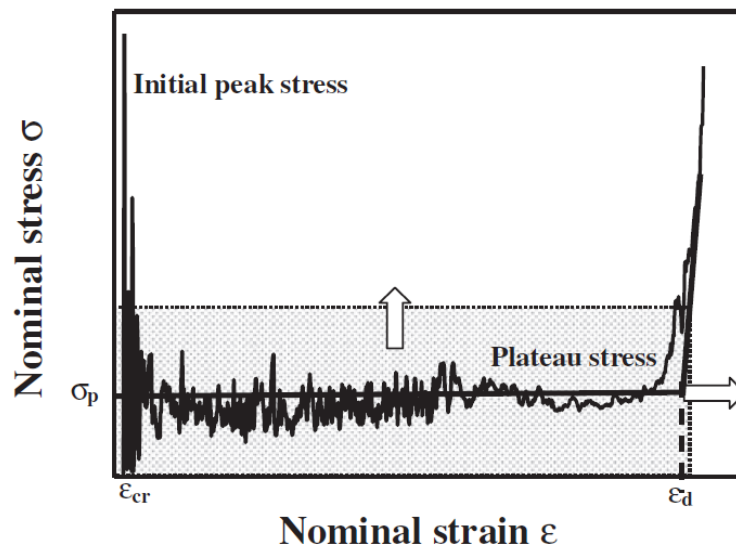


Figure 1.4: Stress-strain diagram of honeycombs from [5]

According to Zhang et al. [6], energy absorption in lattice structures is more efficient in structures with a negative Poisson's ratio. Structures with a negative Poisson's ratio can be called auxetic, expand transversely under stretching, or shrink under compression, which allows them to exhibit enhanced energy-absorbing properties. Auxetic material behavior is shown in Figure 1.5. Since these materials contact while compression, the relative density of deformed geometry increases. Also, the edges of auxetic structures start touching each other at small strains, creating frictional energy. Therefore, the energy absorption of auxetic materials is expected to be efficient. However, while the auxetic property increases, the stiffness of the global lattice structure can be decreased. Thus, it should be examined in detail.

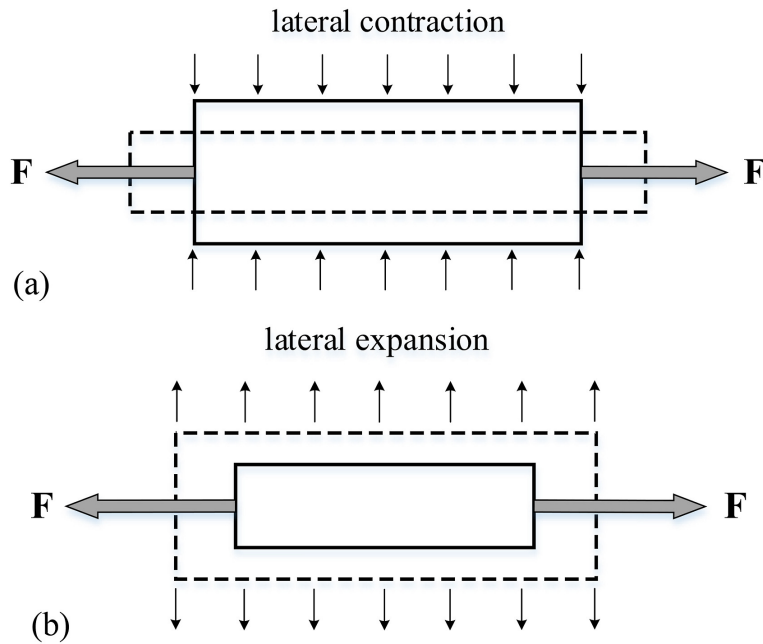


Figure 1.5: Schematic diagrams of (a) conventional materials with a positive Poisson's ratio and (b) auxetic materials with a negative Poisson's ratio under tensile loading from [6] (Solid line and dash line respectively describe the materials before and after deformation).

## 1.2 Literature Review

Ren et al. [7] explores the design, fabrication, and testing of auxetic nails. These nails are specialized with negative Poisson's ratio properties, designed to improve push-in and pull-out performance in timber and medium-density fiberboard (MDF). These nails, characterized by a shrinking lateral dimension under compression and expansion under tension as shown in Figure 1.6, aim to reduce insertion resistance while enhancing retention. Experimental comparisons between auxetic and non-auxetic nails showed that auxetic nails do not consistently outperform traditional designs, partly due to material inhomogeneity, surface roughness variations, and limited deformation under loading. Finite element analysis confirmed minimal auxetic deformation, prompting suggestions for enhanced designs with higher compressive stiffness and improved tensile auxeticity. The study highlights both the potential and challenges of applying auxetic materials in practical applications.

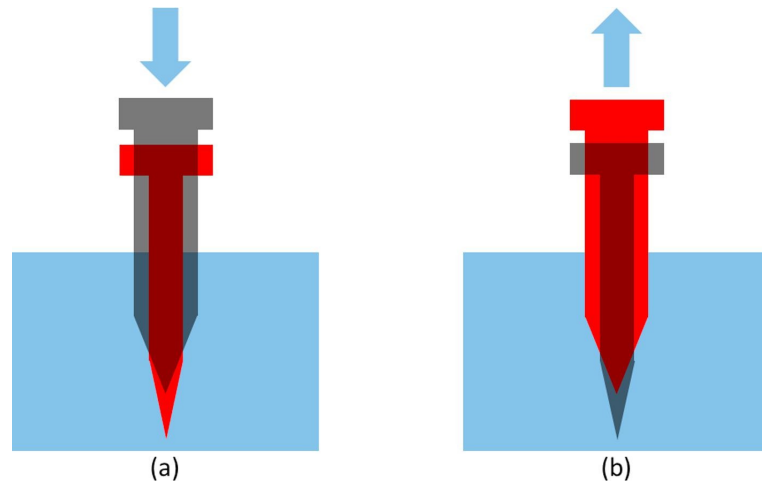


Figure 1.6: Illustration of auxeticity for auxetic nails: (a) during push-in; (b) during pull-out. (The nails in grey and red colour represent the configurations of the nails before and after deformation, respectively) from [7].

The primary purpose of auxetic nail work is to ensure that the nail is easily driven into the wood and difficult to remove. Since the nail exhibits expansion behavior during the removal process, it is expected to create more friction force than a non-auxetic nail. This behavior can be compared to auxetic materials absorbing more energy while being compressed in energy absorption applications. In energy absorption applications, the reaction forces on the structure serve to comment on the energy absorption efficiency.

Another study was conducted by Li and Wang [8], which looked at the behavior of the force on the structure with increasing auxetic properties. It investigates the bending behavior of sandwich composite structures with 3D-printed core materials featuring truss, conventional honeycomb, and re-entrant honeycomb designs. The study integrates experimental tests, numerical analysis, and 3D printing techniques to evaluate these cores in sandwich composites with carbon-fiber-reinforced polymer face sheets. The re-entrant honeycomb, characterized by a negative Poisson's ratio, displayed sequential snap-through instabilities enhancing energy absorption. In contrast, truss and conventional honeycomb cores offered higher flexural stiffness but experienced earlier failure due to localized stress. An experimental comparison of the applied loads towards three different core structures is given in Figure 1.7. The findings demonstrate the potential to tailor core topologies for specific mechanical

applications, balancing stiffness, strength, and energy absorption properties.

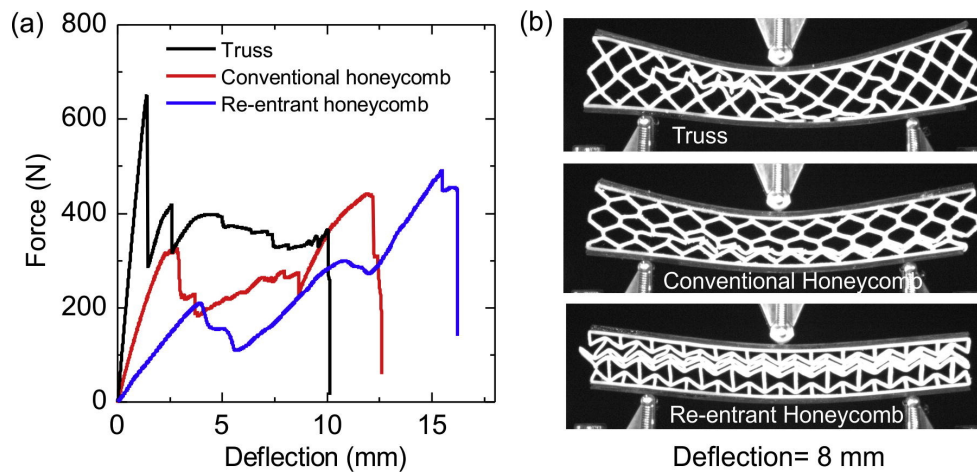


Figure 1.7: Bending characteristic of sandwich composite specimens. (a) Load-deflection curves; (b) the images of deformed configuration of each sandwich specimen at a deflection of 8 mm from [8].

Jiang et al. [9] show auxetic materials' efficiency in the medical field. The study proposes the development of a new type of artificial inter-vertebral disc (IVD) implant designed for treating lumbar disc herniation. In this condition, a spinal disc bulges out of place, pressing on nerves and causing pain or mobility issues. The implant uses an innovative 3D-printed structure called a "modified Bucklicrystal," made of thermoplastic polyurethane, a flexible and biocompatible material. The key feature of this implant is its negative Poisson's ratio (NPR), meaning it contracts inward when compressed instead of bulging outward, as traditional materials do. This behavior allows it to absorb and distribute stress more evenly, which can reduce pressure on surrounding nerves and tissues. Finite element analysis showed that the implant closely mimics the natural movement and load-bearing function of the spine. In *in vitro* (lab-based) studies, the implant-supported cell growth showed no toxic effects, indicating it is safe for use in the body. In *in vivo* (animal-based) tests demonstrated that the implant maintained spinal height, reduced tissue damage, and preserved spinal mobility over eight weeks, suggesting it could effectively replace damaged discs. This research offers a promising step toward better treatment options for spinal conditions with improved functionality and bio-compatibility. In Figure 1.8, the geometry in which non-auxetic and auxetic discs are produced, how they behave



when compressed, and the stress distributions of the compression analyses are given. Non-auxetic discs are named TPU-X, and auxetic discs are named TPU-A. The results of compression tests of TPU-X and TPU-A specimens are given in Figure 1.9. The test images and Poisson's ratio graph show that the TPU-X geometry is non-auxetic, while the TPU-A geometry is auxetic. The energy absorption graph indicates that the TPU-A geometry, which shows auxetic properties, has a higher energy absorption efficiency.

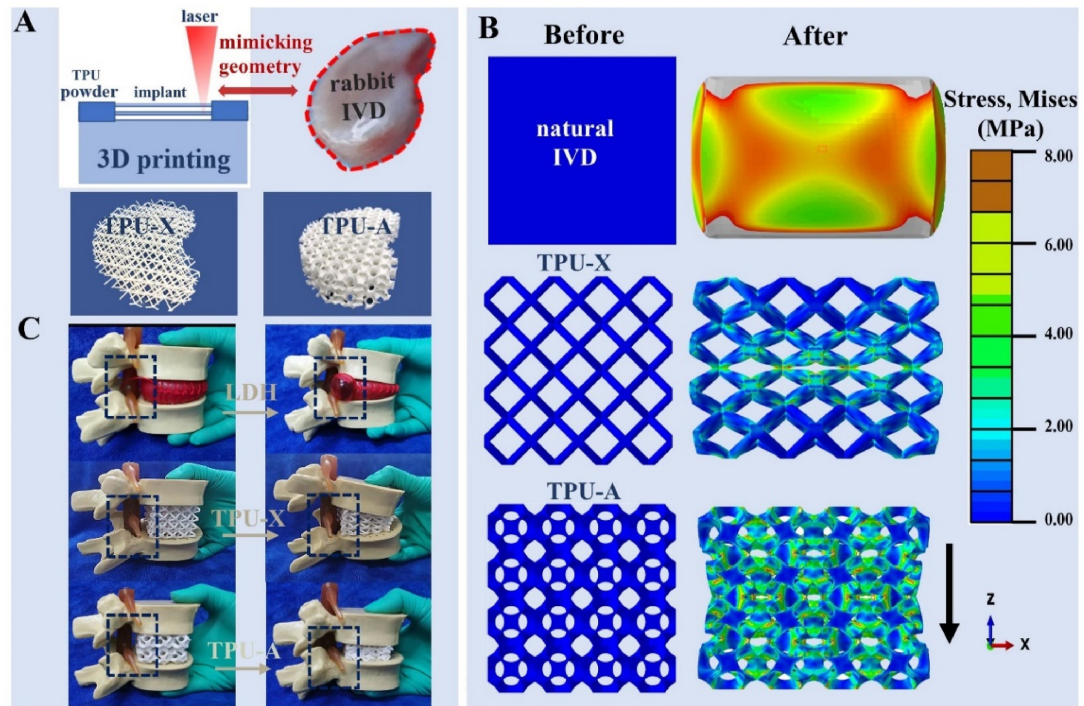


Figure 1.8: A) Schematic illustrating the SLS fabrication process and printed implants with geometry mimicking the rabbit IVD, B) The stress and deformation distribution within natural IVD, TPU-X and TPU-A under compression (the mid-sagittal plane of 3D analyses), C) The behavior of TPU-X and TPU-A under compression using a commercial lumbar disc herniation model from [9].

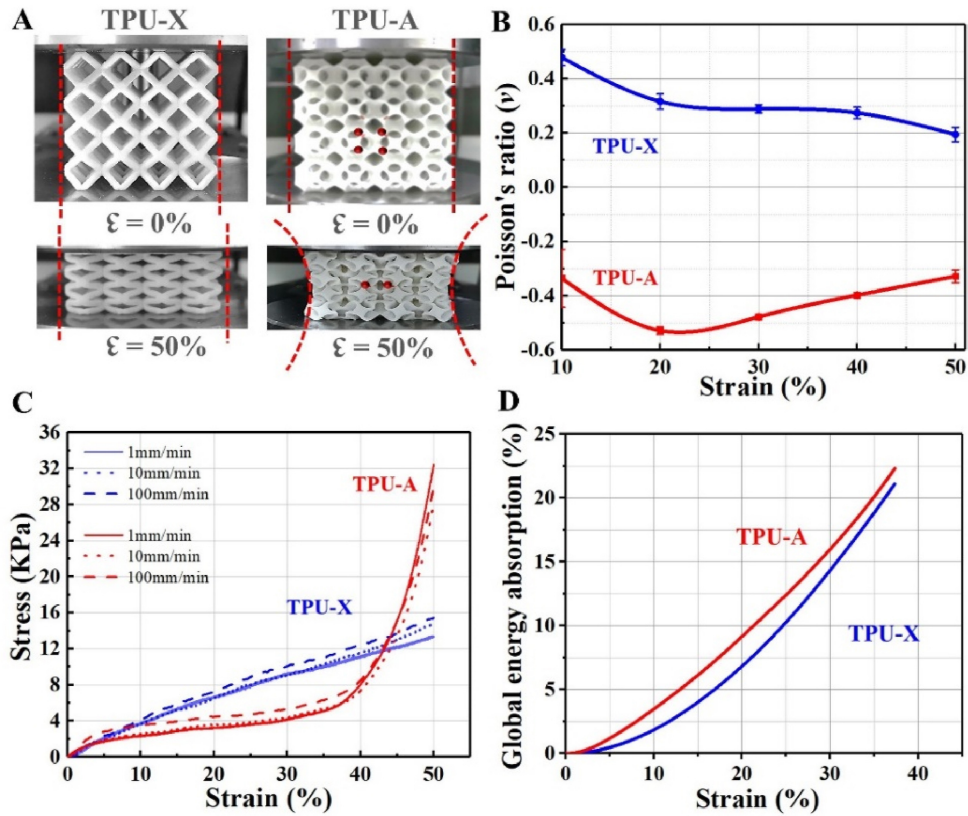


Figure 1.9: A) Optical images showing TPU-X and TPU-A in compression, B) The Poisson's ratio of TPU-X and TPU-A during compression testing, C) The compressive stress-strain curves, D) The global energy absorption curves of TPU-X and TPU-A from [9].

As an example of the use of auxetic lattice materials in the defense industry, Imbalzona et al. [10] investigate the comparative performance of Hybrid Auxetic Composite Panels (HACPs) and conventional honeycomb panels (EPPs) under blast loading, focusing on their structural and material responses. HACPs incorporate auxetic cores characterized by a negative Poisson's ratio, enabling them to contract laterally when compressed, which leads to unique deformation and energy absorption mechanisms. Auxetic and honeycomb unit cells are given in Figure 1.10. These properties allow HACPs to draw material into the loaded zones, effectively localizing and redistributing stresses while minimizing transmitted forces on underlying structures, such as concrete foundations. This contrasts with EPPs, which exhibit a bending-dominated response, leading to less effective load distribution and higher peak stresses. Using areas of purposed HACPs panels shown in Figure 1.11.

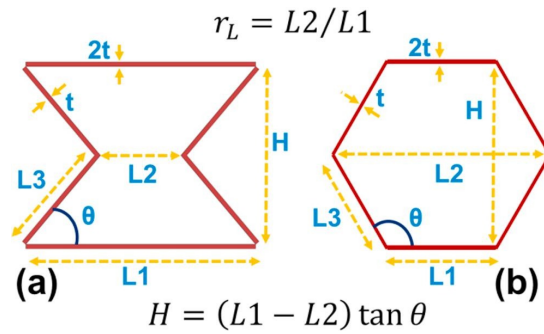


Figure 1.10: Schematic design of 2D auxetic unit cell (AU) (a) and honeycomb unitcell (HU) (b) from [10].

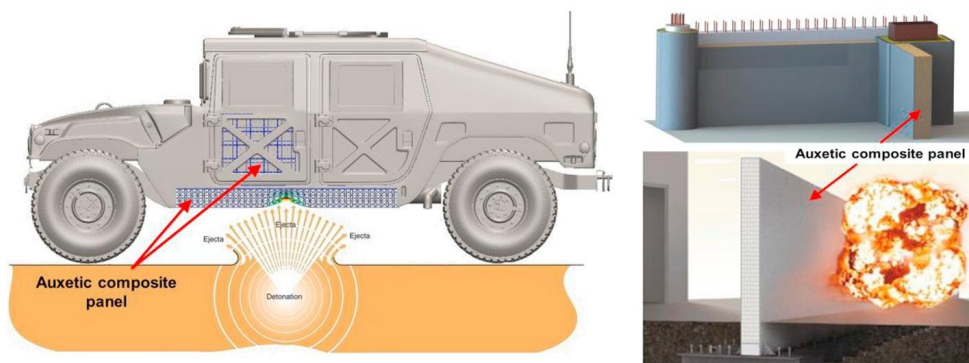


Figure 1.11: An application of lightweight hybrid auxetic composite panels to improve the blast resistance of armoured vehicles and protective structures from [10].

Numerical and analytical models, validated through finite element simulations and empirical data, reveal that HACPs consistently outperform EPPs in blast resistance, energy absorption, and stress redistribution. The auxetic behavior of HACPs ensures that the energy from impulsive loads is dissipated more uniformly, reducing the risk of localized failure and improving the overall structural integrity. Moreover, HACPs' ability to densify material in response to impact enhances their load-bearing capacity and resistance to dynamic forces. Parametric studies further demonstrate the influence of geometric factors, such as the angle ( $\theta$ ) and length ratio ( $r_L$ ), on the performance of both panel types. For HACPs, smaller angles and specific length ratios improve energy absorption and load resistance by increasing stiffness and deformation adaptability. Effective Poisson's Ratio (EPR) measurements indicate that HACPs maintain a consistent negative EPR throughout deformation, with

values ranging between -0.05 and -0.7, depending on the configuration. This property enhances their capacity to adapt to extreme loading scenarios, making them ideal for protective applications. Material selection also plays a critical role in the superior performance of HACPs. The aluminum 5083-H116 used for auxetic cores combines a high strength-to-weight ratio with excellent energy absorption and ductility. Its rate-dependent properties, modeled using the Johnson-Cook framework, allow HACPs to withstand high strain rates, further enhancing their blast resistance. In comparison, EPPs rely on traditional honeycomb designs that, while effective in some applications, lack the auxetic behavior critical for advanced energy absorption and stress management. In terms of practical applications, HACPs provide a lightweight yet highly efficient solution for protecting critical infrastructure and vehicles from explosive threats. By combining auxetic cores with metallic facets, these panels achieve superior structural performance while maintaining manufacturability and cost-efficiency. Overall, HACPs demonstrate significant advantages over EPPs, offering enhanced blast resistance, better energy dissipation, improved load distribution, and greater adaptability, making them a promising choice for modern protective systems.

Etemadi et al. [11] explore how auxetic meta-materials with a negative Poisson's ratio (NPR) relate to energy absorption, emphasizing mechanical performance and structural efficiency improvements. Figure 1.12 depicts the schematics of an auxetic structure and design parameters. Important parameters include strut thickness ( $t$ ), radius ( $r_1$  and  $r_5$ ), and overall unit cell connectivity, significantly influencing energy absorption and auxeticity.

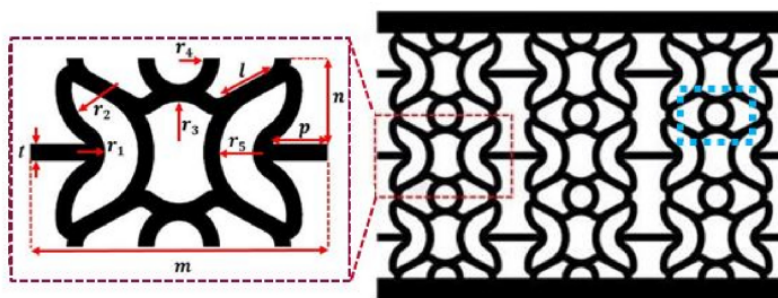


Figure 1.12: Designed structure in [11]

Figures 1.13 and 1.14 demonstrate how geometric parameters influence the specific

energy absorption (SEA) and negative Poisson's ratio (NPR) in the structure. SEA increases significantly with strut thickness ( $t$ ) due to greater resistance to collapse, and it improves with smaller  $r_1$ , which enhances energy dissipation through tighter curvature. NPR is most affected by  $r_1$ , with smaller values allowing more transverse contraction and auxeticity, while  $t$  and  $r_5$  have minor impacts. Notably, SEA shows non-monotonic behavior with  $r_5$ , initially increasing and then decreasing as  $r_5$  grows. These findings highlight the critical role of parameter optimization in balancing energy absorption and auxeticity.

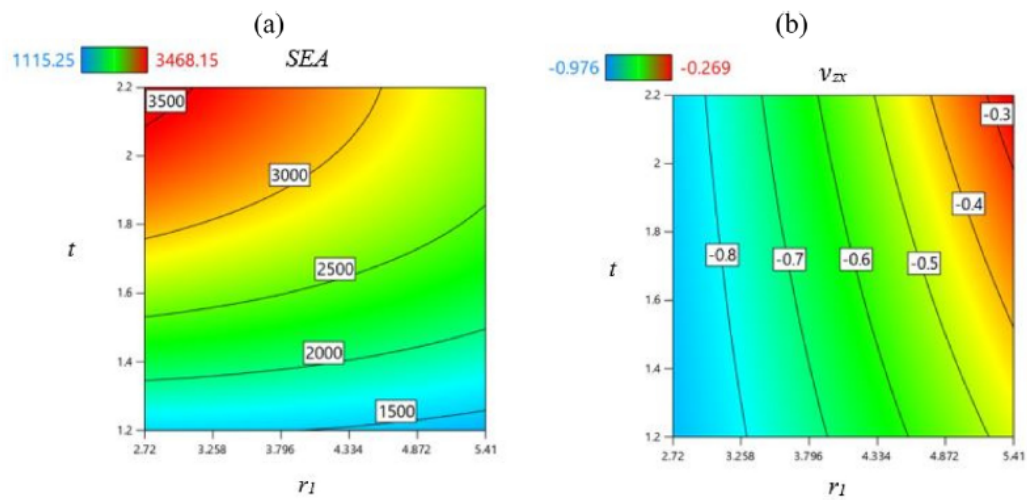


Figure 1.13: Effects of geometry parameters  $r_1$  and  $t$  on: (a) specific energy absorption and (b) Poisson's ratio from [11]

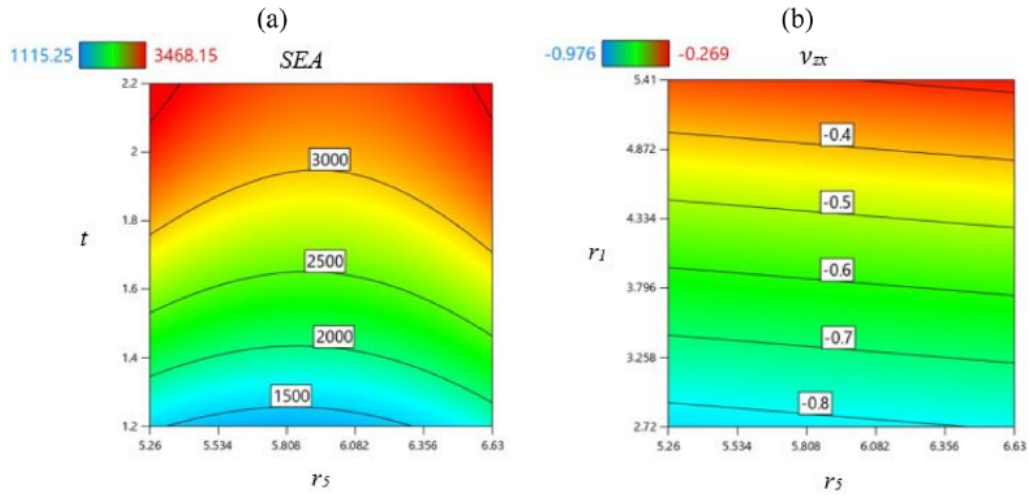


Figure 1.14: Effects of geometry parameters: (a)  $r_5$  and  $t$  on specific energy absorption and (b)  $r_5$  and  $r_1$  on Poisson's ratio from [11]

Tan et al. [12] study the in-plane crashworthiness of re-entrant hierarchical honeycombs with negative Poisson's ratio (NPR), focusing on two configurations: the Re-entrant Hierarchical Hexagonal (RHH) and Re-entrant Hierarchical Triangular (RHT) honeycombs. These designs integrate the hierarchical structure concept with auxetic characteristics by replacing the cell walls of traditional re-entrant honeycombs (RH) with substructures of hexagons (RHH) or equilateral triangles (RHT). Using finite element (FE) simulations validated against theoretical models, the study explores their energy absorption performance, deformation mechanisms, and stress-strain responses under quasi-static and dynamic compression. Geometries of the re-entrant and hierarchical lattices are given in Figure 1.15.

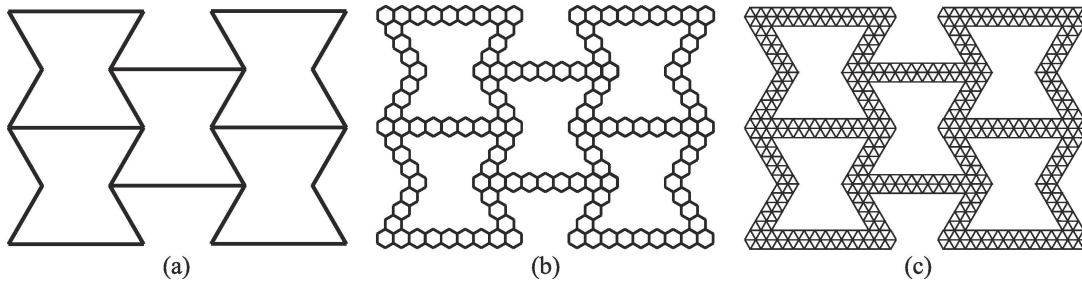


Figure 1.15: Schematic illustrations of re-entrant honeycomb and hierarchical honeycombs. (a) RH. (b) RHH. (c) RHT from [12]

Results demonstrate that RHT and RHH exhibit significant improvements in energy absorption and mechanical strength compared to RH. Specifically, under quasi-static compression, RHT achieves 292% higher specific energy absorption (SEA) and 353% higher stress at plateau regions, while RHH shows a 105% increase in SEA and 138% in stress compared to RH. Both hierarchical honeycombs maintain their NPR characteristics, enhancing their ability to dissipate energy. The SEA and Poisson's ratio results of compression analyzes of RH, RHH, and RHT geometries are given in Figure 1.16.

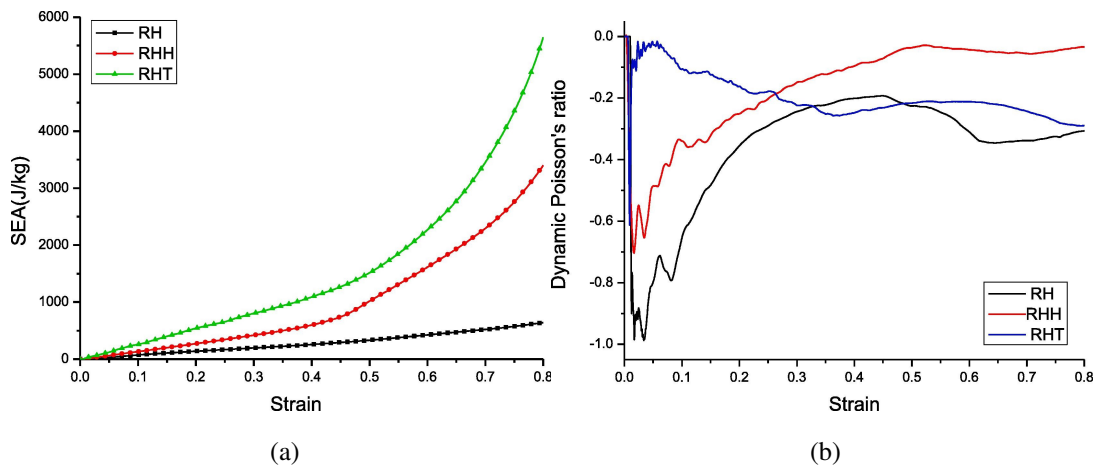


Figure 1.16: SEA and Poisson's ratio with respect to strain curves of RH, RHH and RHT from [12].

Logakannan et al. [13] investigate a novel auxetic structure, the re-entrant diamond design, developed to enhance energy absorption and mechanical performance under quasi-static and dynamic compression. The structure demonstrated auxetic behavior with a consistently negative Poisson's ratio by replacing vertical walls in conventional re-entrant cells with diamond-shaped elements. Cross-links introduced in the diamond cells further increased stiffness and strength while reducing the Poisson's ratio. Illustrations of a re-entrant unit cell and re-entrant diamond unit cell are given in Figure 1.17b. A re-entrant diamond unit cell with cross-link members is shown in Figure 1.17c.

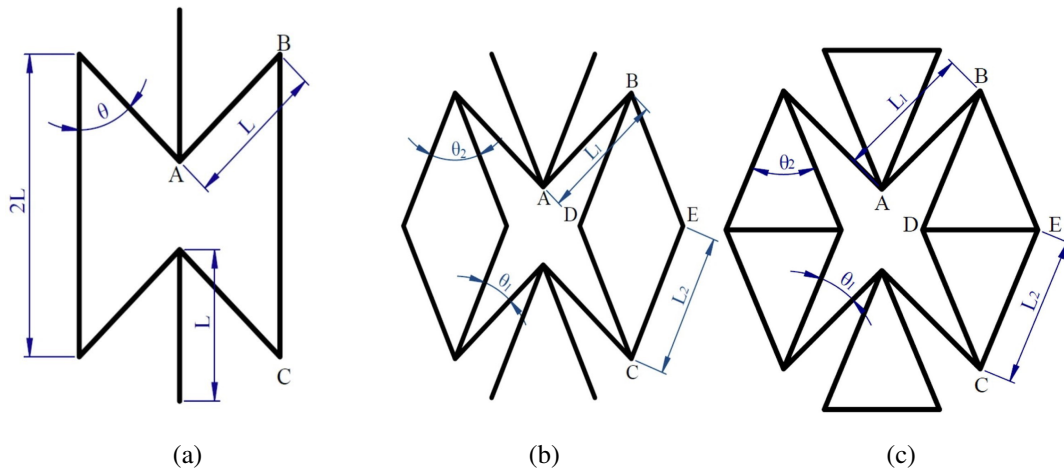


Figure 1.17: Unit cells of re-entrant (a), re-entrant diamond without cross-link (b), and re-entrant diamond with cross-link (c) geometries from [13].

In Figure 1.18, the stress and Poisson ratios of diamond re-entrant unit cells with and without cross-link are given according to their strain values. The cross-linked unit cell is more auxetic and can carry more load. The study conducted a parametric analysis to evaluate the effects of diamond angle ( $\theta_2$ ) and length ratio ( $L_2/L_1$ ) on the performance of the re-entrant diamond structures, both with and without cross-links.



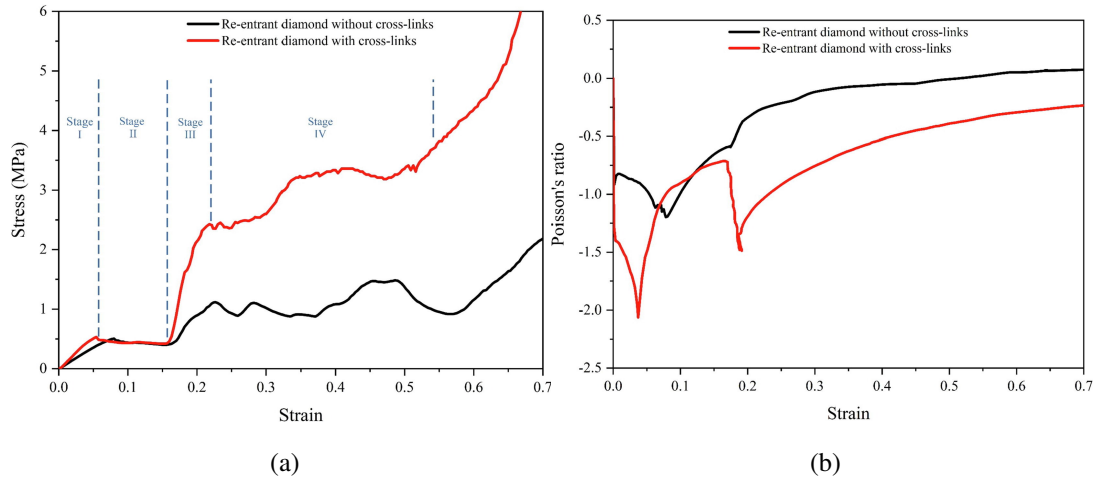


Figure 1.18: FE simulated stress–strain curves (a) and Poisson’s ratio (b) of re-entrant diamond structures with and without cross-link members from [13].

As a result of parametric studies, it was seen that a linear relationship could not be established between Poisson’s ratio and energy absorption. Stress and Poisson’s ratio results are given in Figures 1.19 and 1.20 of crosslinked re-entrant diamond structures according to angles and length ratios, respectively.

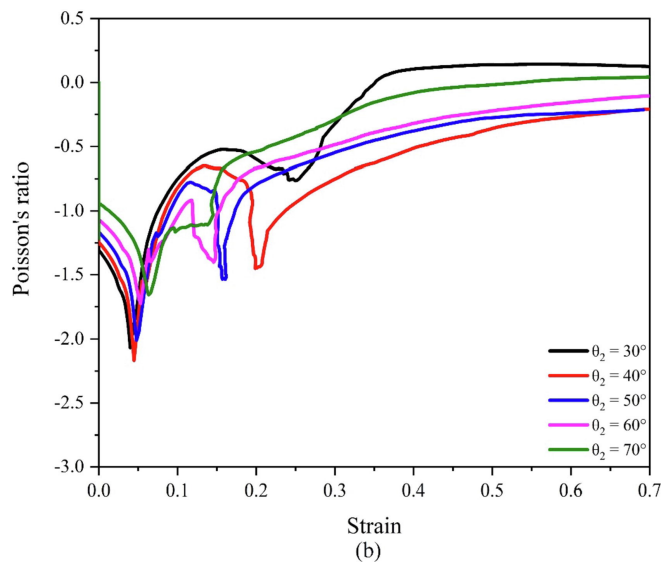
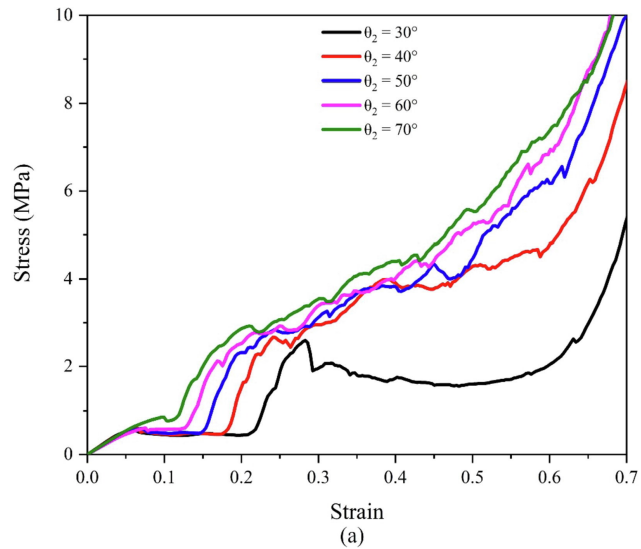


Figure 1.19: (a) Stress–strain curves; (b) Poisson’s ratio of re-entrant diamond structures with cross-links for different diamond angles ( $\theta_2$ ) from [13].

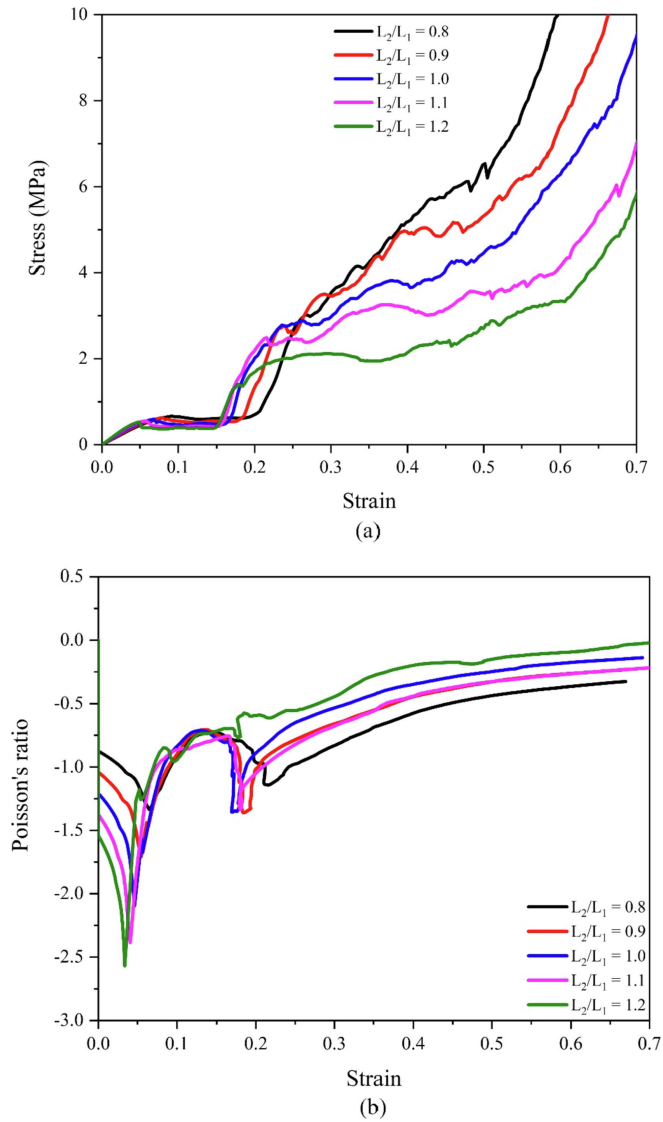


Figure 1.20: (a) Stress–strain curves; (b) Poisson’s ratio of re-entrant diamond structures with cross-links for different length ratios ( $L_2/L_1$ ) from [13].

In addition, Tancogne-Dejean et al. [14], investigate the mechanical performance of additively manufactured metallic micro-lattice materials, focusing on octet truss lattice structures (shown in Figure 1.21) made from stainless steel 316L using Selective Laser Melting (SLM). These materials are designed for high specific energy absorption (SEA) under static and dynamic loading conditions, achieving a relative density of around 30%. The study demonstrates that these lattices exhibit a stable stress plateau during compression, enabling efficient energy dissipation before densification. Simulations and experiments show that deformation

mechanisms transition from localized failures, such as twisting and buckling, at low densities to more uniform and stable deformation at higher densities. The SEA increases with relative density, making the lattices ideal for energy-absorbing applications. Compared to conventional honeycombs, these lattices provide higher SEA and isotropic energy absorption, overcoming the limitations of honeycombs under off-axis loading. Although the SLM process introduces slight geometric and microstructural variations, the fabricated lattices closely match simulation predictions. The study concludes that octet truss lattice, the plastic Poisson's ratio being close to zero is one of the factors that enables the material to exhibit a stable stress plateau and achieve high SEA, particularly under compression.

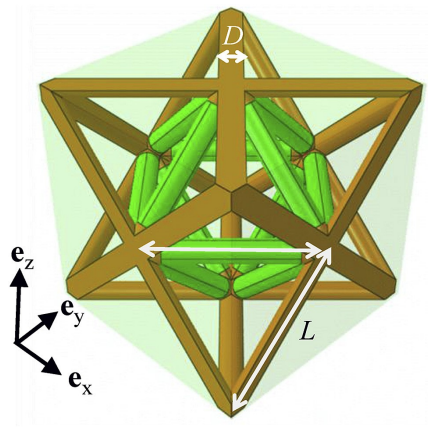


Figure 1.21: Unit cell of the octet truss lattice material from [14].

The studies of Xiao et al. [15] and Lin and Liu [16] collectively emphasize the development of advanced lattice and metamaterial structures, such as butterfly-shaped mechanical metamaterials, multi-concave honeycombs, and metallic micro-lattices, to achieve high energy absorption, mechanical stability, and adaptability. Zero or near-zero Poisson's ratio is central in these designs, enabling smooth deformation and preventing out-of-plane warping, along with geometric optimization to enhance stiffness, deformation range, and specific energy absorption (SEA). Variable stiffness properties are also integrated to balance load-bearing capability with adaptive deformation, addressing challenges in applications like deformable wing skins. These innovations demonstrate significant potential for lightweight, energy-efficient solutions in aerospace, automotive, and protective systems, offering tailored performance for dynamic and high-impact scenarios.

To understand more clearly the relationship between Poisson's ratio and energy absorption capability, this thesis focuses on how geometry affects lattices' ability to absorb and dissipate energy. Through analyzing various lattice designs, such as variations in cell shape, thickness, and cell angle, the study aims to comprehend their mechanical response under stress. Another purpose of the study is to create a relationship between Poisson's ratio and the energy absorption capacity of the lattice structures. While investigating energy absorption capacity and its relationship with the Poisson ratio, the definitions of some properties, such as plateau stress, critical strain, locking strain, and densification, are also examined.

### **1.3 The Outline of the Thesis**

This thesis includes five chapters, and the organization is as follows. Chapter 2 covers the comparison studies. In this chapter, several comparison studies with literature are presented to verify the models and the analysis framework. In Chapter 3, three different lattice models and their parameters are given. Analyses are detailed. Calculations of plateau stress, critical strain, locking strain, specific energy absorption, and Poisson's ratio value are explained. Chapter 4 includes results. The energy absorption capacities of the five different variations of three lattice geometries are presented and compared. The Poisson's ratios of the models are also calculated, and the relationship between energy absorption and Poisson's ratio is constituted. In Chapter 5, conclusions and future studies are presented.



## CHAPTER 2

### COMPARISON STUDIES

#### 2.1 Introduction

This chapter shows the results of two fundamental studies in the literature and compares the results of the present work with the referenced studies. Karabatak [17] has been a guide in examining the behavior of lattice materials and conducting comparative studies; the same reference studies were used. The first of the studies examines the results of the compression of hexagonal lattice geometries of different thicknesses under different velocities. The second study compares the energy absorption outputs of the lattice from cylindrical unit cells and the lattice from a new type of unit cell named quadri-arc. In addition to the two literature comparisons, the energy conservation of the explicit analyses is conducted, and the comparison of the explicit and implicit analyses is given in Appendix B and Appendix F, respectively.

#### 2.2 In-plane dynamic crushing of honeycombs—a finite element study

Ruan et al. [18] published a paper investigating the in-plane dynamic behavior of hexagonal aluminum honeycombs under impact loading using finite element simulations (via ABAQUS) in 2003. They focussed on the effects of cell wall thickness and impact velocity on deformation modes and plateau stress. In the study, a lattice geometry consisting of hexagonal unit cells was compressed in both  $x_1$  and  $x_2$  directions, and the behavior of the structure was investigated according to its thickness and compression rate. The lattice model used and the compression in the  $x_1$  direction are shown in Figure 2.1.

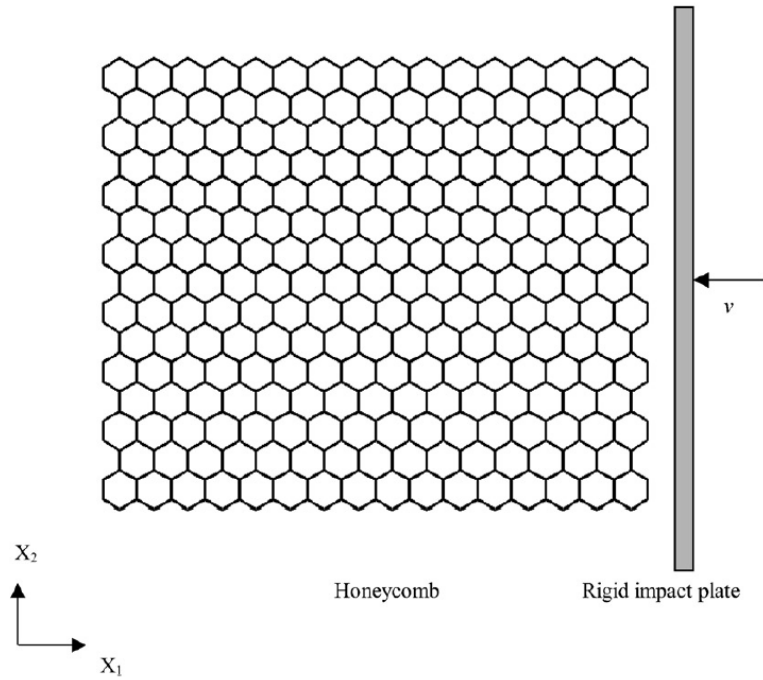
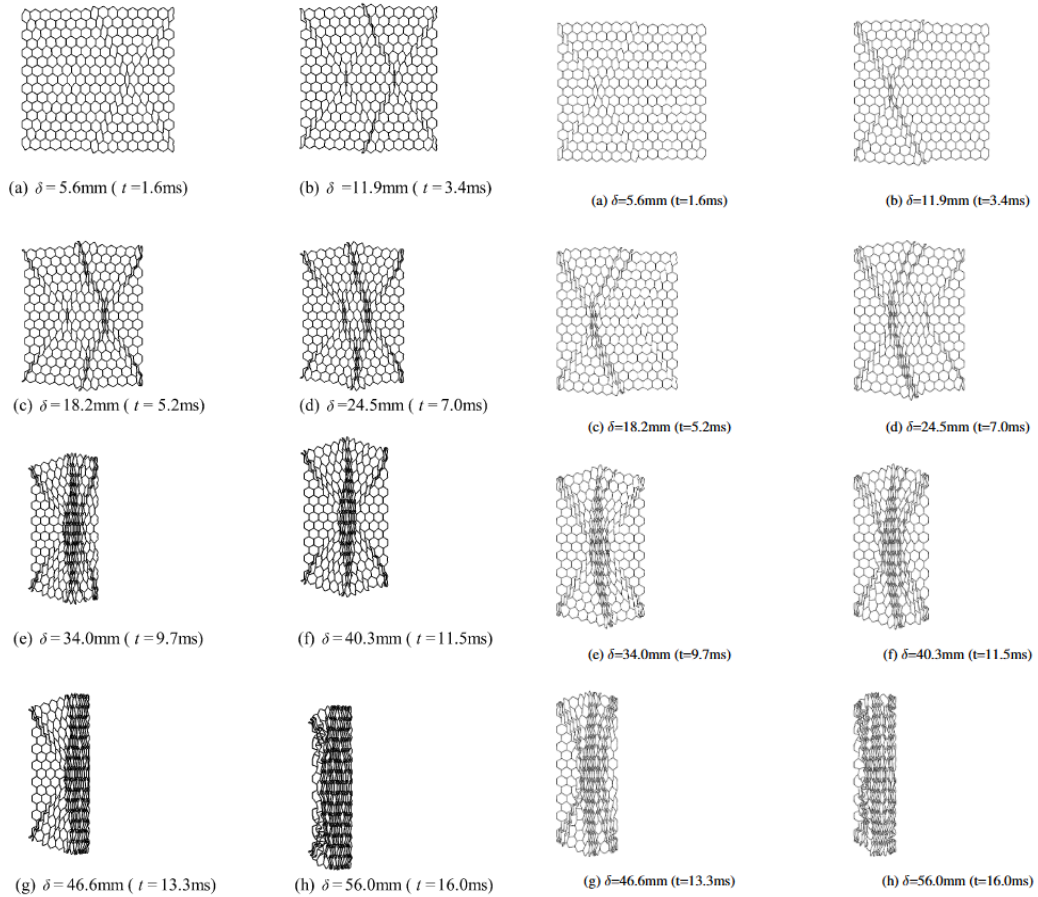


Figure 2.1: FE model and a rigid impact plate used in the simulation of hexagonal lattice from [18]

The edge thickness values of the hexagons were increased from 0.08 mm to 0.5 mm. Five different thickness values were used. The compression velocity was increased from 3.5 m/s to 280 m/s for the  $x_1$  direction, and analyses were performed for nine different speeds. In other words, a total of forty-five studies were performed for the  $x_1$  direction. The forty-five compression analyses in the referenced research were repeated to check that the other lattice compression studies in this thesis were performed with the proper modeling approach. In order to make a visual comparison and examine the geometries' deformation behavior, the situation where the thickness is 0.2 mm, and the velocity is 3.5 m/s is shared in Figure 2.2. The images on the left of the figure are from the reference study, and those on the right are from the analyses performed in the current study. The 'X' shape can be seen in both outputs at small strains from compression behavior at this thickness and velocity. As the strain level increases, these 'X' shapes merge, forming a rhombus geometry. As the compression increases, the rhombus narrows, and the geometry becomes tighter.





Referenced study [18]

Current study

Figure 2.2: Comparison between Ruan et al. [18] and current study of crushing of honeycomb with thickness = 0.2 mm, impact velocity = 3.5 m/s

The deformed views of the structure at 14 m/s velocity with the same thickness are given in Figure 2.3. This time, compression is similar to a 'V' shape instead of an 'X' shape. The 'V' shape thickens as the strain increases, and the entire geometry compresses.

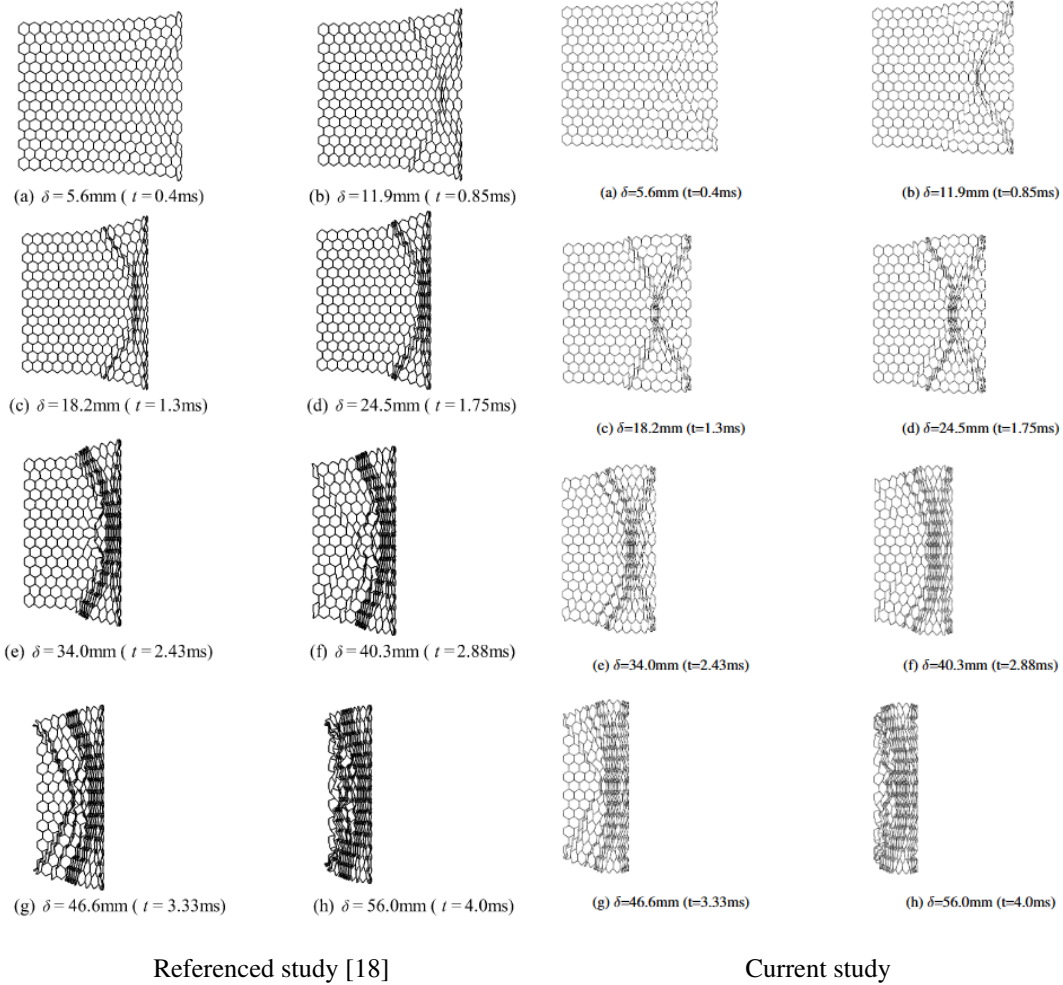


Figure 2.3: Comparison between Ruan et al. [18] and current study of crushing of honeycomb with thickness = 0.2 mm, impact velocity = 14 m/s

If the compression velocity is increased even more and analyzed with the same thickness, the comparative results are shown in Figure 2.4. Again, the images on the left are taken from the reference article, and those on the right are taken from the analyses made for this thesis. This time, the velocity is 70 m/s and compression behavior creates an 'I' shape, not an 'X' or 'V' shape. Concentration starts directly on the compression surface and grows in the concentrated area with increased strain.



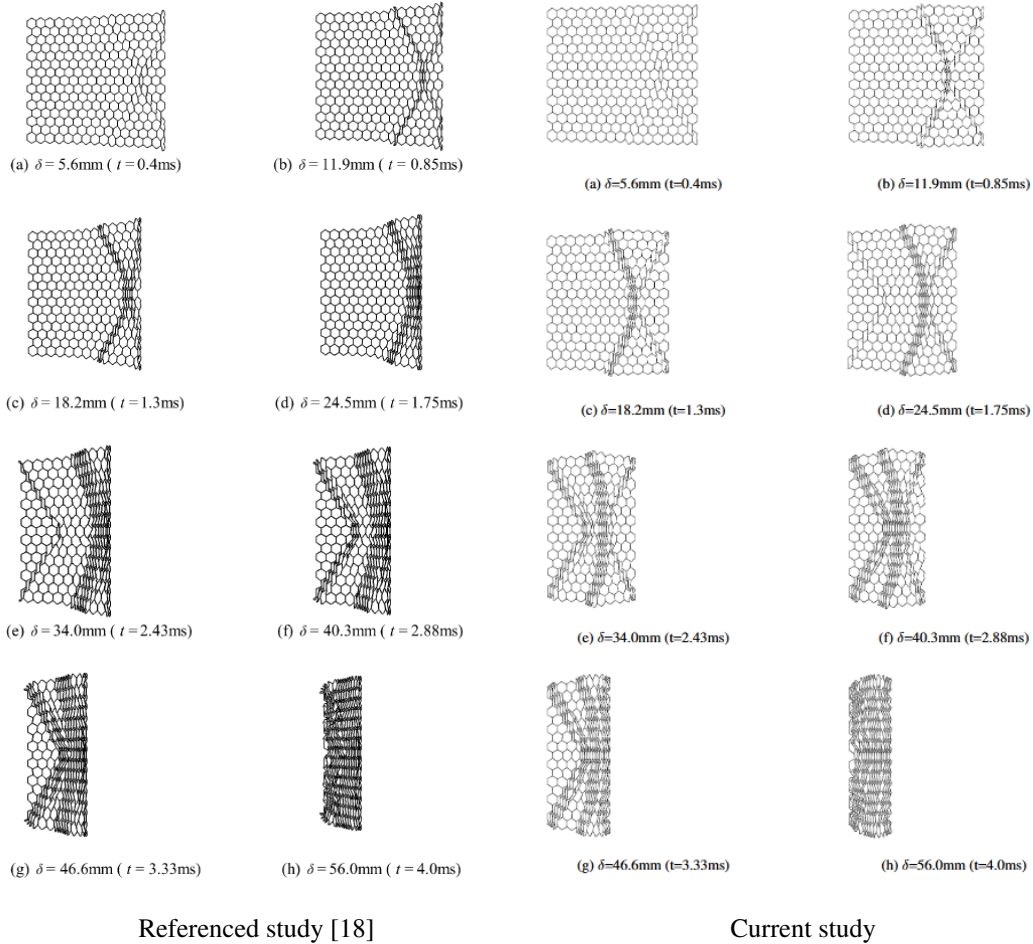
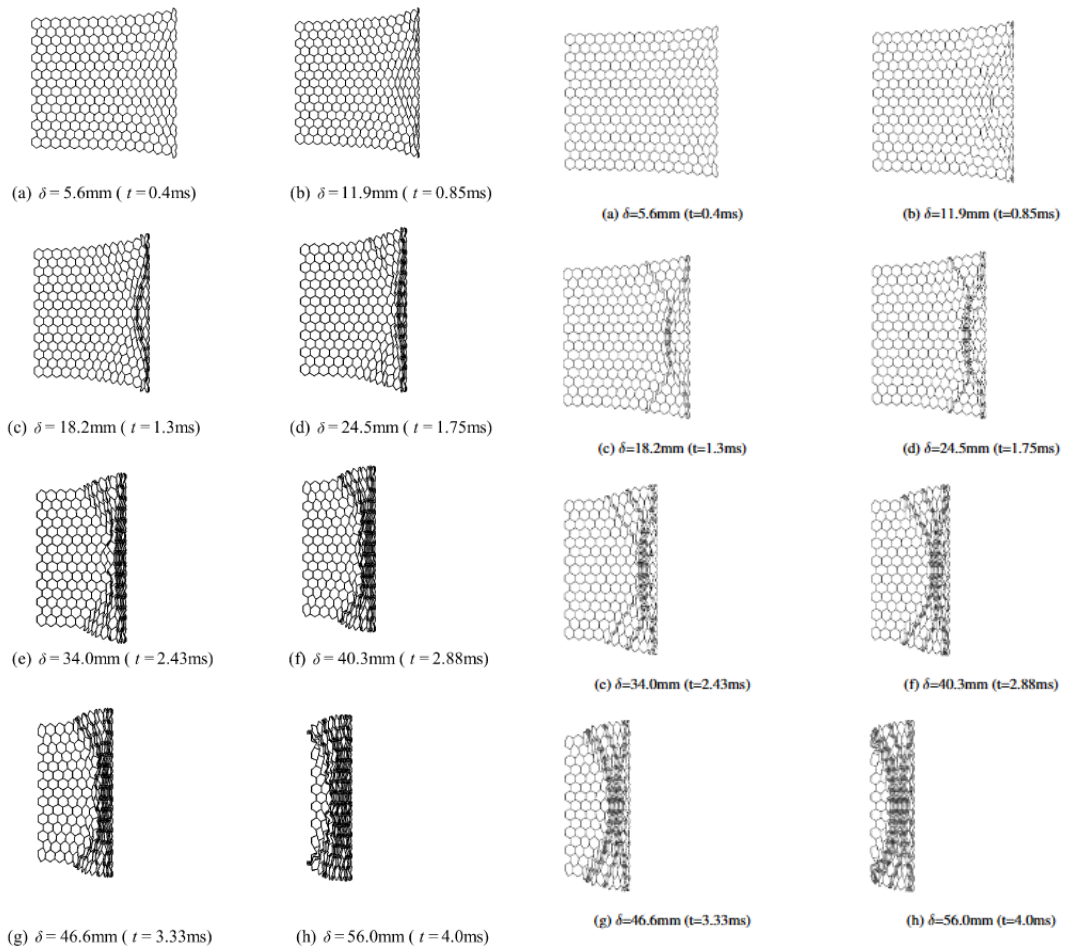


Figure 2.5: Comparison between Ruan et al. [18] and current study of crushing of honeycomb with thickness = 0.5 mm, impact velocity = 14 m/s



Referenced study [18]

Current study

Figure 2.6: Comparison between Ruan et al. [18] and current study of crushing of honeycomb with thickness = 0.08 mm, impact velocity = 14 m/s

These deformation modes determine how the material absorbs and dissipates energy during impact. The localized deformation patterns (e.g., X-shaped or I-shaped bands) reflect how stresses are distributed and concentrated within the hexagonal lattice. Understanding these patterns helps optimize the lattice designs for crash-worthiness and impact resistance in various applications, such as the aerospace and automotive industries. In this thesis, no optimization study is conducted according to deformation behavior, but optimization studies specific to collision situations can be undertaken in the future.

In addition to the deformed views of the structure, the force-displacement graph of the compression analysis of the 0.2 mm thick lattice at a compression velocity of 14 m/s is given in [18]. Figure 2.7 compares the analyses made in the current study and in [18]. The initial peak force is higher in [18] than the analysis made for the current study. Still, when the plateau region is examined, similar values are obtained. However, the peak stress/force does not influence the energy absorption calculations which will be discussed in Chapter 3.

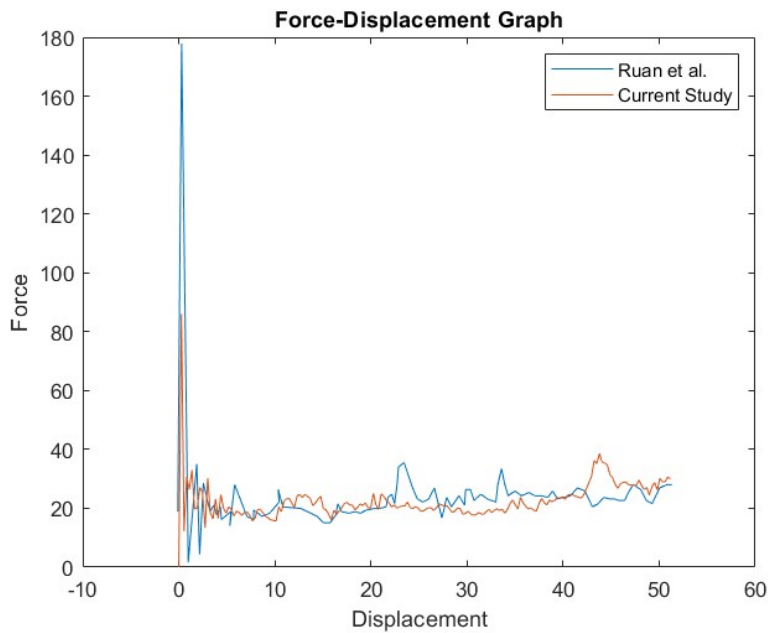


Figure 2.7: Comparison of force-displacement,  $h= 0.2$  mm,  $v= 14$  m/s between the referenced study [18] and the current study

This referenced study [18] aimed to establish a relationship between plateau stress,

compression rate, and structure thickness. The plateau stress is formulated as follows:

$$\sigma_p = \sigma_0 + Av^2, \quad (2.1)$$

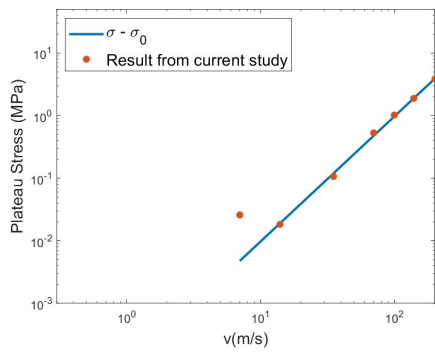
where  $\sigma_0$  is static plateau stress, and its value was taken from [19]. It is multiplied by 1.15 to account for the plane strain condition of the cell walls.  $v$  is compression velocity, and  $A$  is a coefficient that depends on the thickness and edge length. This coefficient was calculated as follows in a way that is compatible with the least squares method as a result of the finite element analyses of the referenced study.

$$A = 4742\left(\frac{h}{l}\right)^2 + 3115\left(\frac{h}{l}\right) + 0.75 \quad (2.2)$$

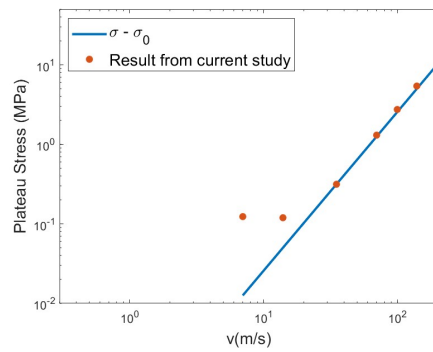
As a result, the plateau stress equation is:

$$\sigma_p = 0.8\sigma_{ys}\left(\frac{h}{l}\right)^2 + 4742\left(\frac{h}{l}\right)^2 + 3115\left(\frac{h}{l}\right) + 0.75 \quad (2.3)$$

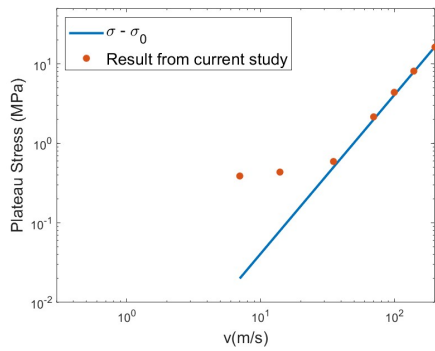
The results of the present work are with Equation (2.3) in Figure 2.8. Five graphs in the figure give the plateau stress of hexagonal lattices with different thickness values depending on the velocity. The graphs' lines simulate the equation where the static plateau term is removed from the Equation (2.3). The dots show the results of the analysis made for this thesis. The  $x$  and  $y$  axes of the graphs are given in the logarithmic range. When the empirical equation in the article is compared with the analyses made for this thesis, differences are seen at small velocities, but these differences are very small in value. Similar differences were also found in the reference study. The comparison of the empirical equation with the analyses made in the reference study is shown in Figure 2.9.



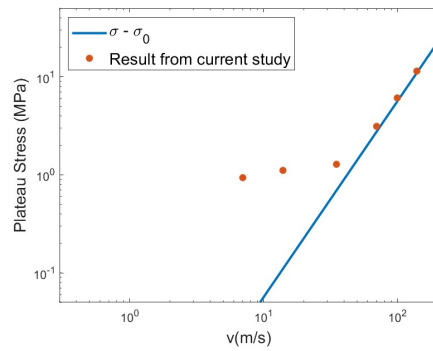
(a)  $h=0.08$  mm



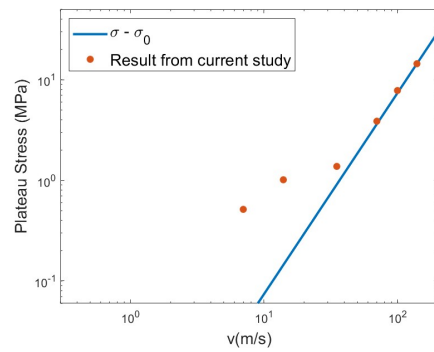
(b)  $h=0.2$  mm



(c)  $h=0.3$  mm



(d)  $h=0.4$  mm



(e)  $h=0.5$  mm

Figure 2.8: Plateau stress change in the  $x_1$  direction with the impact velocity with analyses of the current study



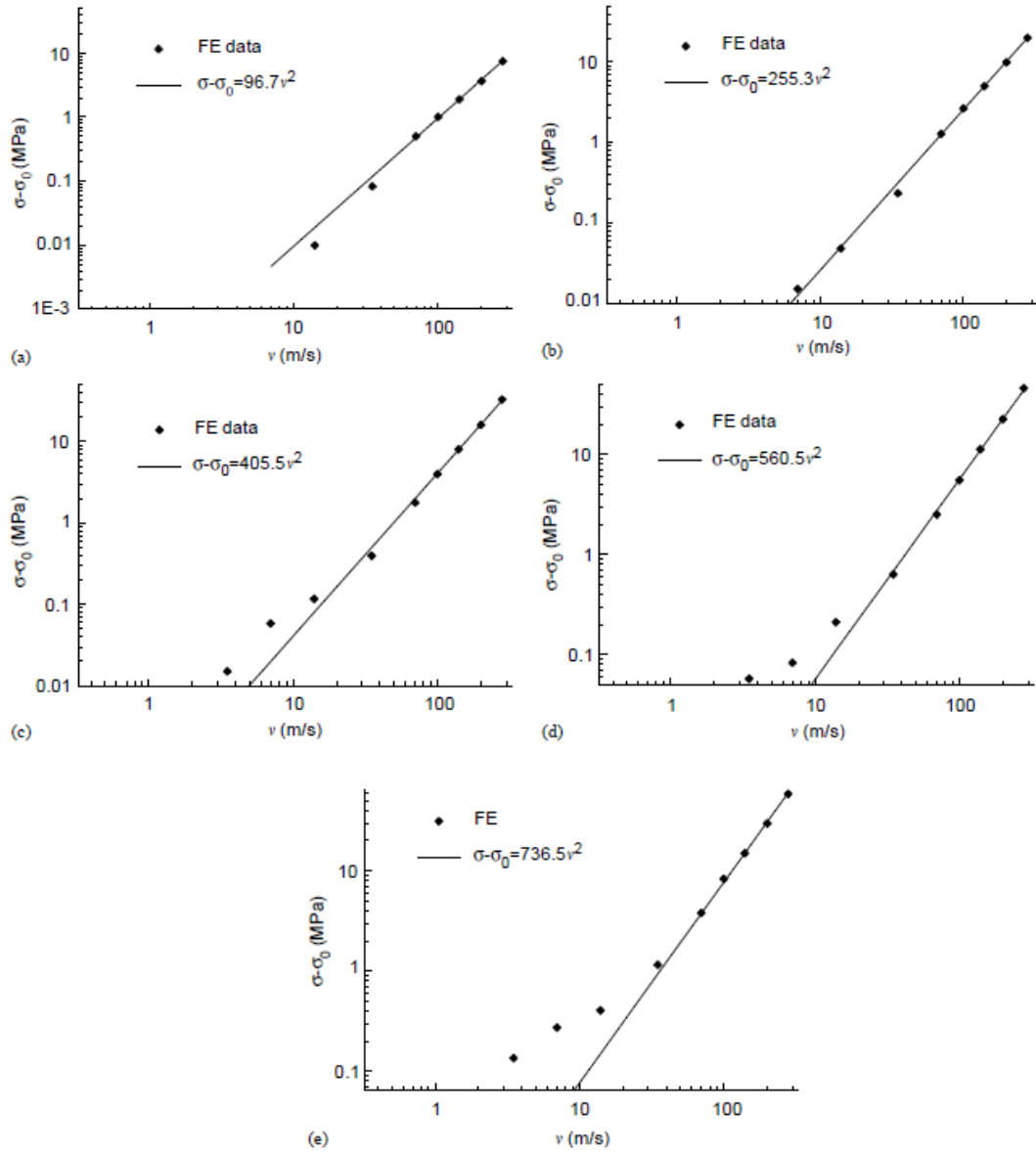


Figure 2.9: Plateau stress change in the  $x_1$  direction with the impact velocity with analyses of the referenced study [18]

It is understood from both the comparisons in Figures 2.2- 2.6 and the comparison in Figure 2.8 that the results of the current study are consistent with the analyses in the reference study. However, while calculating the plateau stress in the reference study [18], the locking strains for 0.08 mm, 0.2 mm, 0.3 mm, 0.4 mm, and 0.5 mm thickness values are 0.95, 0.9, 0.85, 0.82, and 0.78, respectively. It was not fully explained how these values were found. The locking strain calculation for this thesis is described in detail in Section 3.3.1.

### 2.3 In-plane dynamic crushing behavior and energy absorption of honeycombs with a novel type of multi-cells

Zhang et al. [20] presented a geometry consisting of quadri-arc unit cells to increase energy absorption in the lattice structure composed of cylindrical unit cells. The visual of the two lattice structures is given in Figure 2.10.

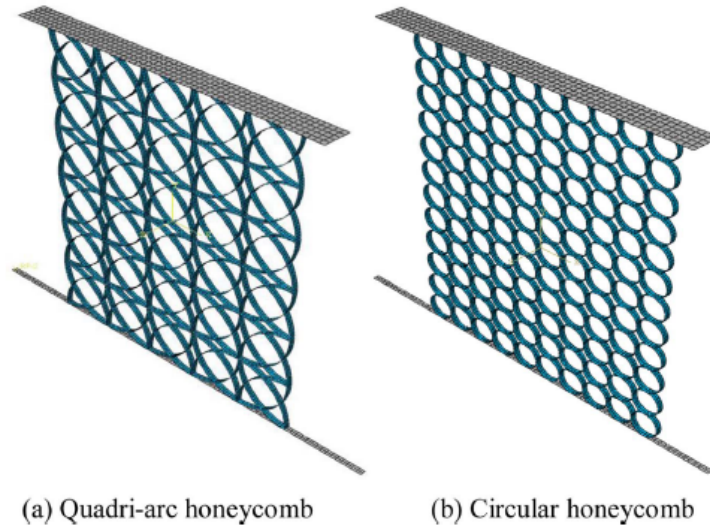


Figure 2.10: 3D view of the numerical models from [20]

The material property of these two structures is aluminum. Young Modulus is 69 GPa, yield stress is 76 MPa, Poisson's ratio is 0.33, and density is 2700 kg/m<sup>3</sup>. This material property is also used in the parametric studies conducted in this thesis. In the reference study [20], two lattices were compressed at three different velocities, and the SEA results for all three velocities were examined. The velocities were determined by the deformation modes mentioned in the previous study. The three different deformation modes are defined as quasi-static mode, transition mode, and dynamic mode. These modes are the X-shaped, V-shaped, and I-shaped deformation modes mentioned in Section 2.2. A relative velocity is selected for each of these three modes. This relative velocity is a parameter that depends on the compression speed of the lattice and the yield speed:

$$\bar{V} = V_0/V_y \quad (2.4)$$

In the equation,  $V_0$  represents the compression speed, and  $V_y$  represents the yield

velocity.  $V_y$  depends on the material properties:

$$V_y = c_0 \epsilon_y, \quad (2.5)$$

where  $c_0$  is the longitudinal elastic stress wave speed,  $\epsilon_y$  is the yield strain, and their equations are:

$$c_0 = \sqrt{E_s / \rho_s} \quad (2.6)$$

$$\epsilon_y = \sigma_{ys} / E_s \quad (2.7)$$

In the equations,  $E_s$  is Young's modulus,  $\rho_s$  is the density of the material, and  $\sigma_{ys}$  is the yield stress. Yield velocity for aluminum is approximately 5.57 m/s. In the reference study, the relative velocity for the quasi-static mode is selected as 0.4, for the transition mode 4.0, and the dynamic mode 12.0. In the parametric studies conducted in this thesis, the relative velocity is 0.4, and since aluminum is selected as the material property, the applied compression velocity is applied as 2.23 m/s.

The compression analyses of the cylindrical lattice in the reference article are repeated in this thesis to make a comparison. First of all, the reference article also compared its work with the study conducted by Wang et al. [21]. Therefore, the results of Wang et al. [21] are also included in the comparison. The force-displacement graphs of the cylindrical lattice under compression at a velocity  $V=2.23$  m/s are given in Figure 2.11. The agreement among the three results is very satisfactory.

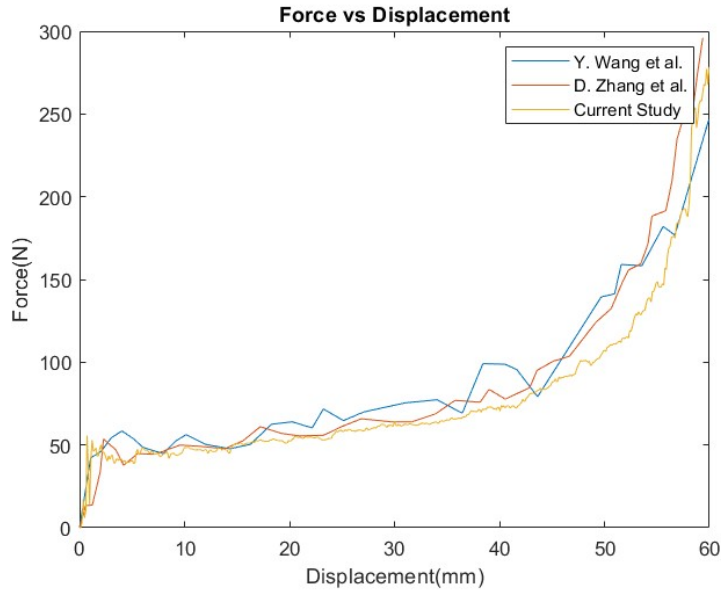
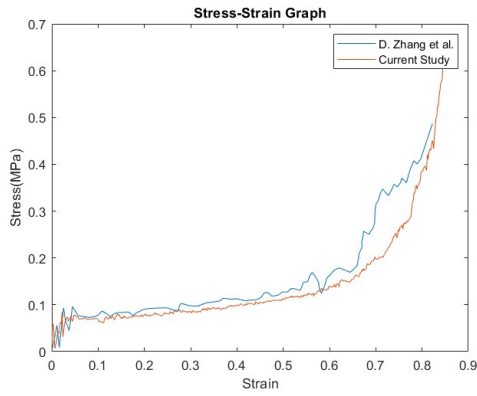
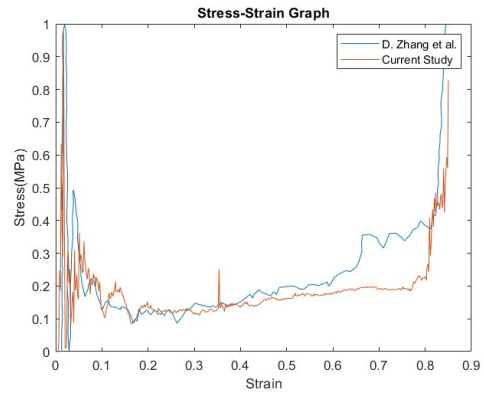


Figure 2.11: Comparison of force results of circular lattice in compression with the studies of Wang et al. [21], and Zhang et al. [20]

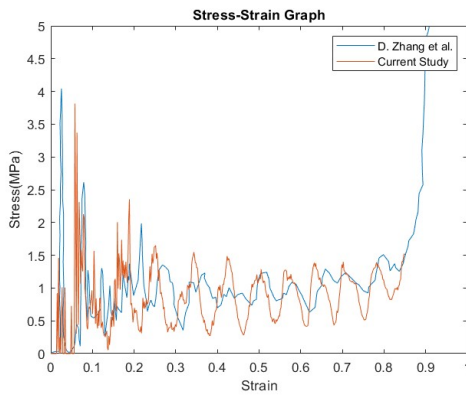
In addition, the compression analyses of the lattice structure in [20] for the quasi-static, transition, and dynamic modes are repeated. The stress-strain diagrams are shown in Figure 2.12. In the quasi-static mode, good agreement with a slight difference in the densification region. In the transition mode, the lattice in [20] starts to densify earlier but slowly, see Figure 2.12b. However, the general agreement is satisfactory. Although the stress outputs at the same strain values in the dynamic mode comparison do not match, the plateau stress values in both studies seem to be close. As a result of comparison studies, it is concluded that the finite element models and analyses of the present work can regenerate the results from the literature with an acceptable agreement.



(a) Quasi-static



(b) Transition



(c) Dynamic

Figure 2.12: Comparison of stress-strain diagrams with the reference study [20]



## CHAPTER 3

### FINITE ELEMENT MODELS AND METHODS OF COMPUTATION

#### 3.1 Introduction

This section explains all computational analysis models and calculation methodologies for Poisson's Ratio, plateau stress, critical and locking strains, and specific energy absorption values.

There are three different lattice units, each with five parametric studies. Thus, there are fifteen models in total to compare energy capacity and investigate Poisson's ratios of the structures. These fifteen models are detailed in the section. Boundary conditions and mesh properties are also explained.

Because the stress-strain curves of the compression analyses of the lattice geometries are complex, specifying critical strain and locking strain values has limitations. So, the geometries' plateau stresses and specific energy absorption values can not be calculated straightly. The Calculation Methodologies Section defines and instantiates the situations and the keys. The calculation of the Poisson's ratios of the models is also explained in this section.

#### 3.2 Models

Geometrical, mass properties and details of the finite element models are given in the following sections for the fifteen different lattice models. These fifteen different models are created from three geometry and five variational studies. Three geometries are hexagonal, re-entrant, and chiral lattices. These are visualized in Figure 3.1 with

variable and fixed parameters. While the edge lengths ( $l_e$ ) are fixed, angle ( $\theta$ ), and thicknesses ( $t_v$  and  $t_h$ ) are variable. The reason why the thicknesses are divided into two groups is that the thickness of the vertical ( $t_v$ ) and horizontal edges ( $t_h$ ) can vary depending on each other.

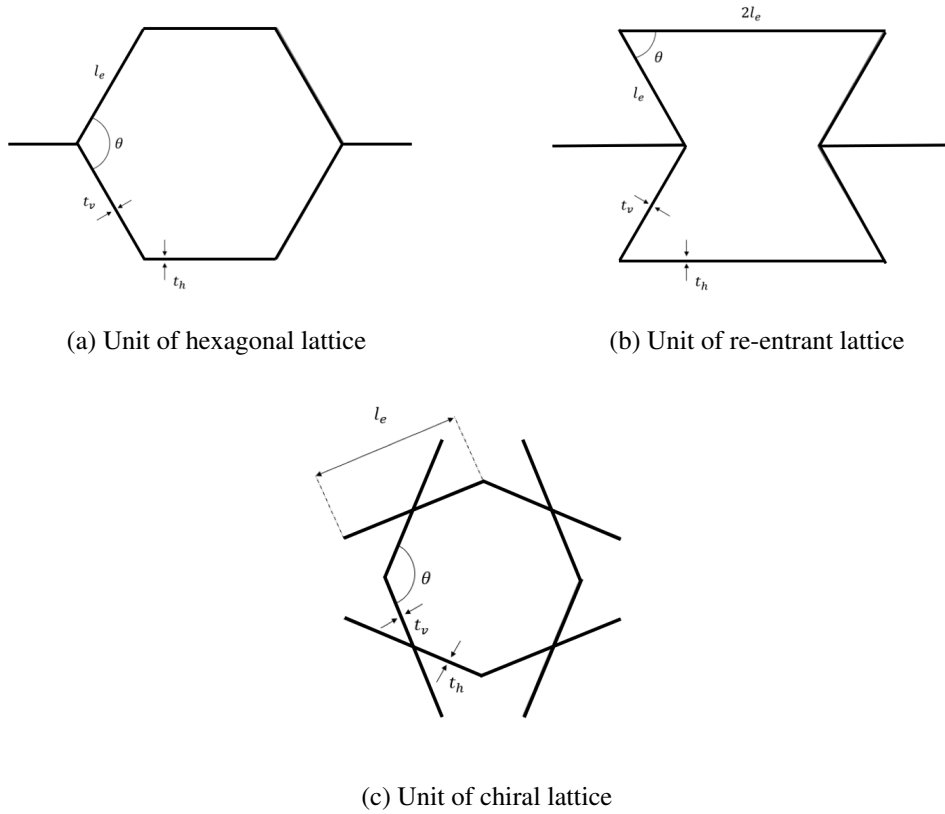


Figure 3.1: Illustration of units of lattice structures

Some geometrical properties are similar or the same: edge length, material properties, and depth. For all models, the depth is 2 mm. Material is modeled as elastic perfectly plastic. For the elastic region, Young's Modulus is 69 GPa, Poisson's Ratio is 0.33, and for the elastic to plastic passing, yield stress is 76 MPa. Density is 2700 kg/m<sup>3</sup>. Material properties are taken from the study of Ruan et al. [18] and are similar to aluminum. All edges of the hexagonal and chiral shapes are equal to each other, and the values of them are 5 mm. In the re-entrant shape, the top and bottom edges are twice as long as the other edges. So, the top and bottom edges are 10 mm, and the other edges are 5 mm. On the other hand, some properties vary from model to model. These are the thickness and angle of the unit cells. Concerning thickness and angle,



some properties can be influenced. These are listed as follows.

- Length and Width Of Structure
- Mass
- Base Area
- Relative Density
- Theoretical Locking Strain

The length and width of the structures depend on the number, angle, height, and width of the unit cells. Mass and base area are connected to thickness and angle, respectively. The base area is critical to calculating stress values. Its value is the multiplication of the width and depth of the body. Relative density is the ratio of the mass of the cellular structure to the bulk structure, and in [5], it is defined as:

$$\Delta\rho = \frac{\rho^*}{\rho_s} \quad (3.1)$$

$\rho^*$  is the volume of the cellular unit cell and  $\rho_s$  is the volume of the bulk unit cell. Since the depths of the models are the same, we can also calculate from areas instead of volume. For example, in the unmodified hexagonal shape, the area of the cellular unit cell should be taken as three times the thickness. Since the model is created from repeated unit cells, half the thickness on each edge must be considered in a unit cell. The bulk area is the area of the equilateral hexagon. By using relative density, locking strain defined in [19], and it is:

$$\epsilon_d = 1 - \lambda\Delta\rho \quad (3.2)$$

$\lambda$  can be defined as the coefficient of the locking strain and is given as 1.4 for hexagonal honeycombs in [19]. In this study,  $\lambda$  is assumed to be 1.4 for all geometries. In Equation (3.2), the locking strain value is theoretical, but in all compression analyses, the locking strain value should be unique to the analyses. A detailed explanation of the calculation of the locking strain is given in the relevant section. As mentioned, depending on thickness and angle change, five variational studies were created:

- Thickness variation between vertical ( $t_v$ ) and horizontal ( $t_h$ ) edges while keeping weight constant
- Adding horizontal edges and changing the thickness of added and former edges while keeping weight constant
- Adding vertical edges and changing the thickness of added and former edges while keeping weight constant
- Changing unit angle ( $\theta$ ) while the weight is kept constant, but the specific density changes
- Changing unit angle ( $\theta$ ) while the specific density is kept constant but weight changes

### 3.2.1 Boundary Conditions for All Models

Two rigid plates were created to simulate compression during the analysis. Their depth and width were adjusted to be greater than the lattice structures, and their weight was given according to the density of  $2700 \text{ kg/m}^3$ . The fixed plate is positioned under the lattice structure, the movable one is positioned on top of the structure, and it moves downwards. The compression amount must be greater than the locking strain value of the structure so that the locking can be seen in the stress-strain curves. As mentioned in Chapter 2, the compression speed was adjusted as if in quasi-static mode. Therefore, the speed was chosen to be approximately  $2.23 \text{ m/s}$ . That is, the upper solid plate was set to be compressed at a speed of  $2.23 \text{ m/s}$  throughout the analysis. However, the velocity boundary condition was not applied to the plate. Displacement boundary condition was applied, and analysis time was adjusted. For example, for the main hexagonal model, the relative density is approximately  $0.0693$ , so the theoretical locking strain is  $0.903$ . The total model length is  $104 \text{ mm}$ . Accordingly, the structure should be compressed more than  $94 \text{ mm}$ , so the compression amount was chosen as  $96 \text{ mm}$ . The selected compression rate must occur within  $0.043$  seconds to adjust the quasi-static mode speed. Thus, a compression speed of  $2.23 \text{ m/s}$  is reached. The compression speed is kept constant for all models. Therefore, the strain rate may change according to the model length. In parametric

studies, where the angles of the unit cells change, the model dimensions change. The strain rate for the hexagonal and re-entrant models with initial angles is  $21.4 \text{ s}^{-1}$ , and for the chiral model, it is  $23.4 \text{ s}^{-1}$ . These models are the shortest models for angle change studies. The strain rate of the longest models is  $18.6 \text{ s}^{-1}$  for all three unit cells. In Figure 3.2, the boundary conditions of the main hexagonal shape are given.

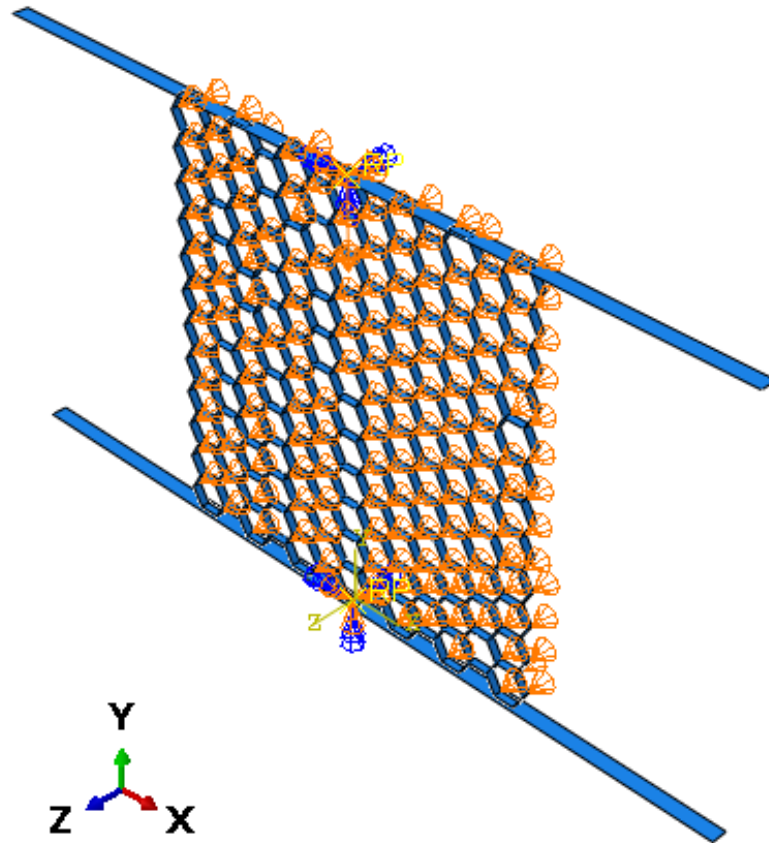


Figure 3.2: Boundary condition of hexagonal lattice structure

The boundary conditions of all models are similar to the boundary conditions in Figure 3.2. If we examine the applied boundary conditions in more detail, the boundary condition applied to the center of gravity of the lower plate fixes the six degrees of freedom of the plate. It is shown in Figure 3.3.

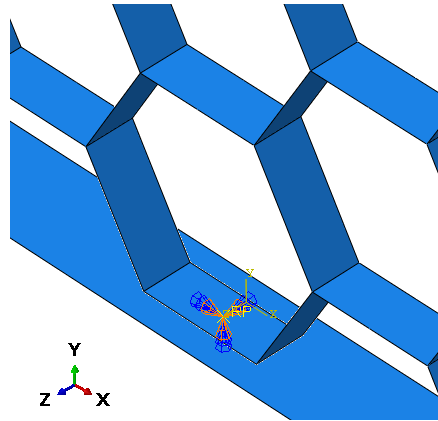


Figure 3.3: Boundary condition of fixed plate

The boundary condition applied to the center of gravity of the upper plate moves the plate along the y-axis while fixing the other degrees of freedom. It is given in Figure 3.4. The value of the y-axis displacement of the upper plate can differ from model to model. As explained, the value of it depends on the relative density and total length of the body.

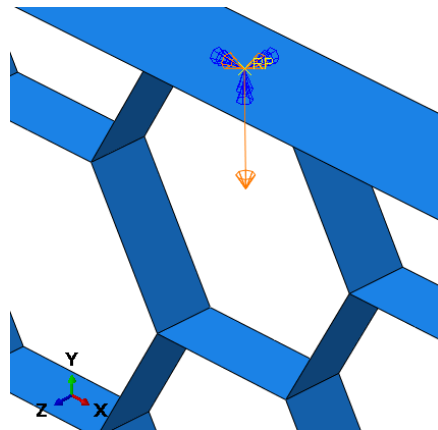


Figure 3.4: Boundary condition of moving plate

The only boundary condition applied to the lattice structure is the displacement boundary condition to constraint z-displacement on one face to prevent global buckling, as visualized in the figure below.

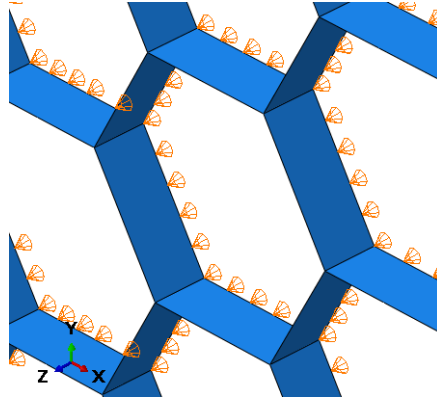


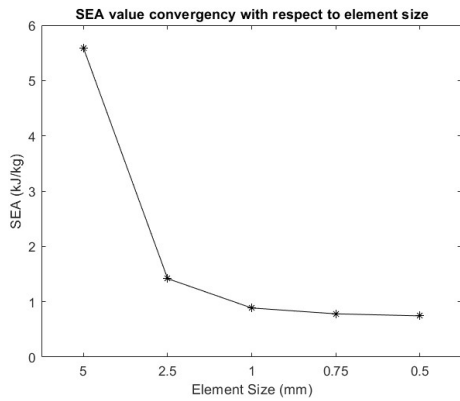
Figure 3.5: Boundary condition of lattice structure

With the boundary conditions applied to the upper and lower plates, an interaction must be established between the plates and the lattice structure for the lattice structure to compress. The same relationship was established between the surfaces of the lattice structure. In this way, the behavior of the surfaces after contact with each other while the structure is compressed can be calculated. The normal behavior of this interaction was chosen as hard contact. In this way, the surfaces do not penetrate each other in the normal direction. Friction was created in tangential behavior. In the study of Zhang et al. [20], a friction coefficient value of 0.3 was taken. This value was used in the parametric studies, but the effect of the friction coefficient change on SEA and plateau stress was examined. Since the friction energy will increase with the increase of the friction coefficient, it is expected that the SEA and plateau stress will increase, and this effect was observed. Details are given in Appendix D.

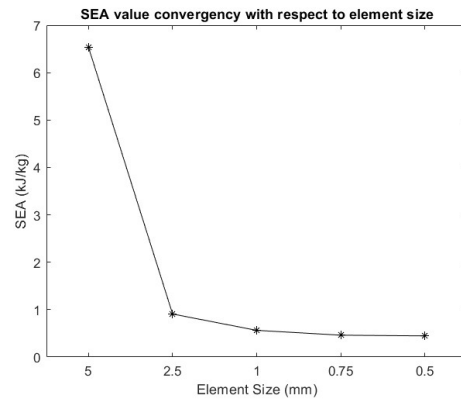
### 3.2.2 Mesh Properties and Convergence Study

The study of Ruan et al. [18] was taken as a reference for meshing. Abaqus/EXPLICIT is used as the analysis program in the related study. S4R, a four-node reduced integration element, was selected as the element type. This element type is used for surfaces defined as shells. That study also selected 1 mm as the element size, but a convergence study was performed for each lattice geometry for the element size. Five different element sizes were selected for hexagonal and re-entrant lattice models. The coarsest mesh was selected as 5 mm, and the finest

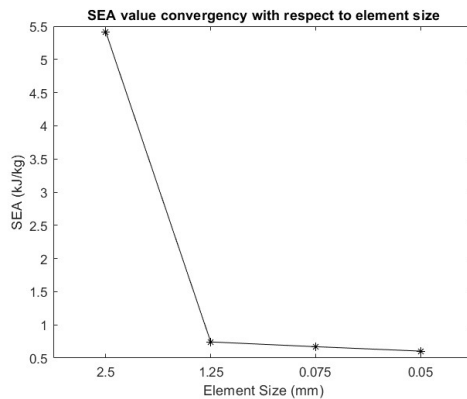
mesh as 0.5 mm. For the chiral shape, four different element sizes were selected between 2.5 mm and 0.5 mm. The element size is important for the lattice structure but not the upper and lower rigid plates. Therefore, the element sizes of the rigid plates were not changed in the convergence study. Figure 3.6 shows how much the SEA value changes for each shape according to the element size. SEA was explained in Chapter 1, and how it is calculated is explained in detail in Section 3.3.1.



(a) Hexagonal lattice



(b) Re-entrant lattice



(c) Chiral lattice

Figure 3.6: SEA outputs of the three lattices according to element sizes

When looking at the outputs of the mesh convergence study, it will be sufficient to use 1 mm elements for the hexagonal and re-entrant models and 1.25 mm elements for the chiral model. Considering the explicit analysis time, there is no need to choose the finest element size to not increase the analysis time too much. In this case, there are elements in the hexagonal model, 6620 elements in the re-entrant model, and 8256

elements in the chiral model. The selected element density is shown on the models in Figure 3.7.

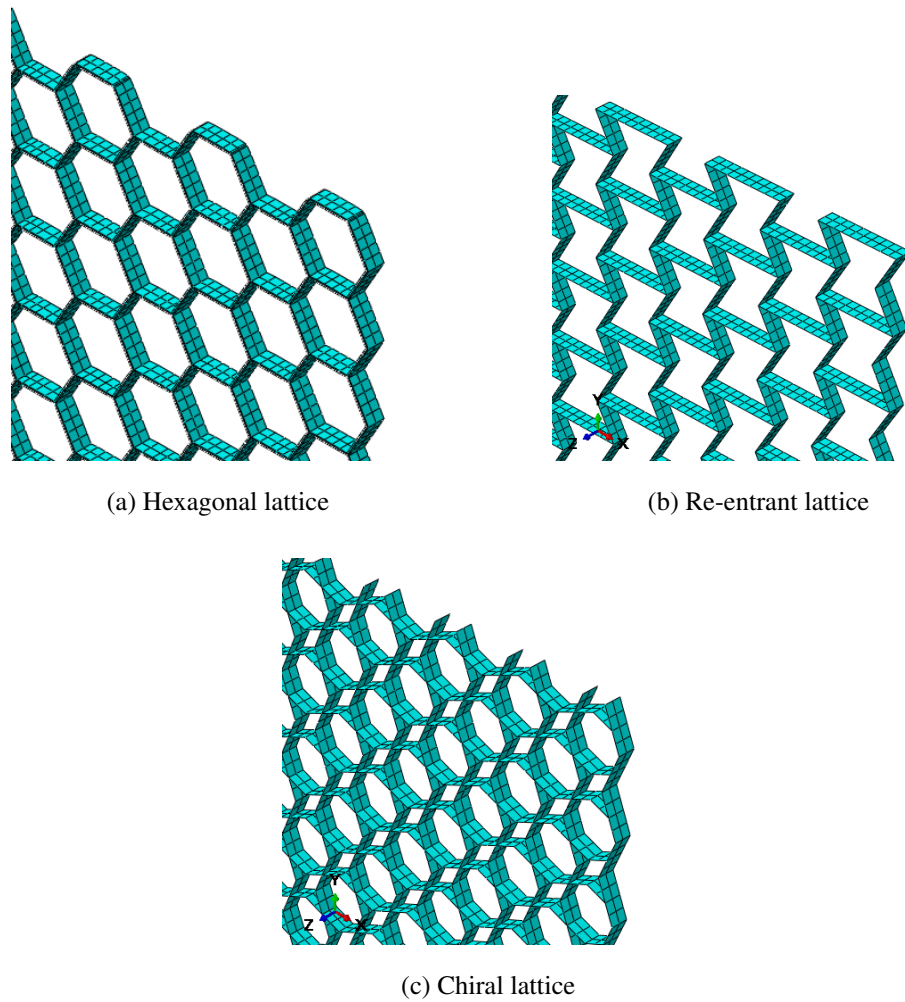


Figure 3.7: Mesh densities of the lattices

In addition to the mesh convergence study, the explicit analysis method with the selected mesh density was compared with the implicit analysis method for low-strain values. However, in the comparison study, the difference between the explicit solution and the implicit solution can be ignored. The study details can be examined in Appendix F.

### 3.2.3 Hexagonal Lattice Structures

A hexagonal lattice is created by repeating the unit seen in Figure 3.1a twelve times in the x-direction and seven times in the y-direction of Figure 3.8. Representation of the structure can be seen in Figure 3.8. In the study of Ruan et al. [18], eight unit cells are used in the x-direction and sixteen in the y-direction. To properly display the compression behavior of the lattice, the number of unit cells in the vertical direction must be above a certain number. Twelve unit cells in this study are sufficient. While determining the number of repetitions of horizontal and vertical unit cells, an attempt was made to approximate the structure to a square. The width of the main hexagonal structure was chosen as 100 mm and the height was approximately 104 mm.

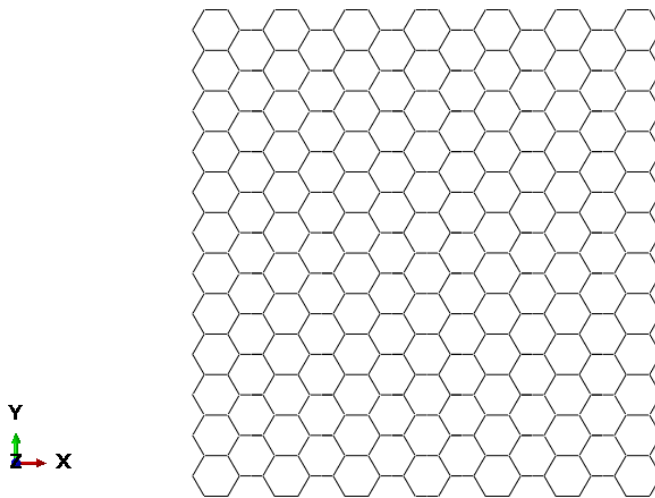


Figure 3.8: Hexagonal lattice structure

It is the base structure for the five different studies listed above. The geometrical and mass properties of the base model are given in Table 3.1.



Edge Thickness	0.3 mm
Angle of Unit	120°
Unit height	8.66 mm
Unit Width	15 mm
Relative Density	0.0693
Theoretical Locking Strain	0.903
Mass	$4.042 \times 10^{-3}$ kg

Table 3.1: Properties of base hexagonal lattice

The first parametric study was the variation of the thickness of the horizontal and vertical edges relative to each other. The thicknesses of the horizontal and vertical edges are specified as  $t_h$  and  $t_v$ , respectively, in Figure 3.1. While making this thickness change, the weight of the lattice was preserved. Since the angle does not change and the weight is kept constant, relative density does not change. So, the locking strain and the total length do not change either according to Equation 3.2. For this reason, the displacement values applied to the upper plate were kept constant in all parametric studies.

In the FE models, three sections are created in the structure to make a thickness difference between vertical and horizontal edges: base section, horizontal section, and inclined section. The thickness of the base section is constant, while the thickness of the horizontal and inclined sections is changed. The sections can be seen in Figure 3.9. The base, horizontal, and inclined sections are green, cream, and red, respectively. The thickness of the base section is kept constant to keep the distance between the top and bottom plate constant in all models.

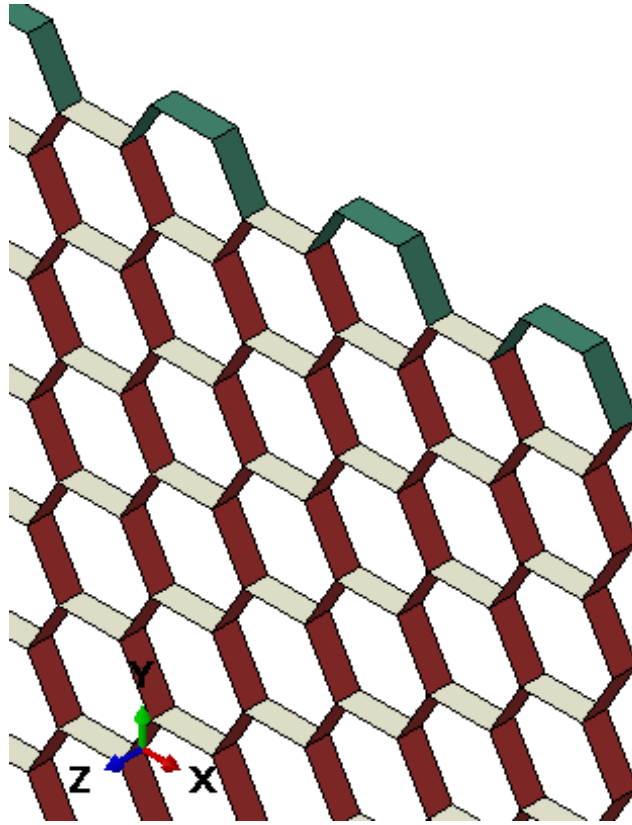


Figure 3.9: Sections of hexagonal lattice structure for vertical and horizontal thickness variation

Fourteen models were created to compare energy absorption capacity and Poisson's ratios. The thickness of the horizontal edges of these models varies from 0.35 mm to 0.001 mm. To maintain weight, the thickness of the inclined elements must increase while the thickness of the horizontal elements must decrease. The most extreme models have the following thicknesses; the inclined edge thickness of the model, which has a horizontal edge thickness of 0.35 mm, is approximately 0.28 mm; the model has the horizontal edge thickness of 0.001 mm, has the inclined edge thickness of approximately 0.45 mm. The thickness of the base part does not change in any model, and it is 0.3 mm.

The second parametric study was to add horizontal edges to the unit cells and change their thickness. The thickness of the original lattice geometry was reduced to keep the weight constant when adding elements and changing their thickness. Again, three sections were created, and the thickness of additional and original sections was

changed, but the thickness of the base section was kept constant. In Figure 3.10, the green, red, and cream sections can be seen. These are the base section, the additional section, and the original lattice section, respectively.

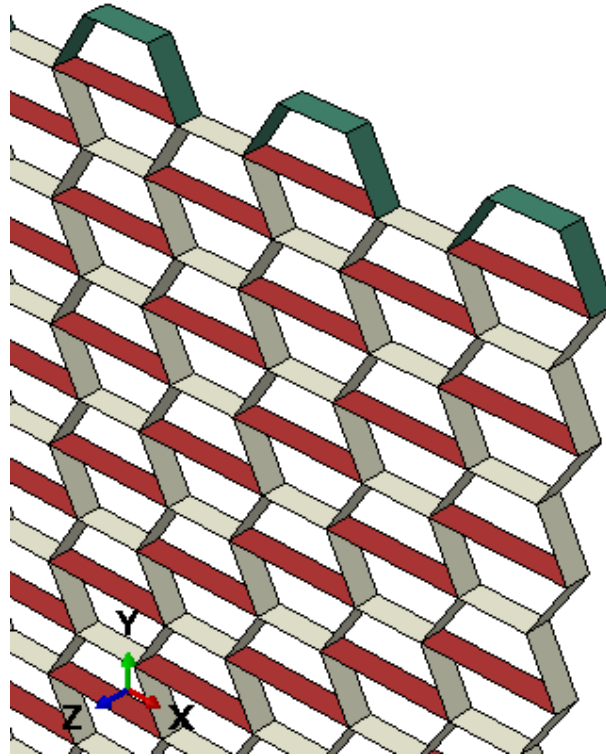


Figure 3.10: Sections of hexagonal lattice structure of the model with horizontal edges added

In this study, the thickness of the added horizontal edges is increased from 0 mm to 0.4 mm. While increasing the thickness of the additional edges, the thickness of the original lattice geometry should be reduced from 0.3 mm to 0.037 mm so that the weight can be preserved. Sixteen models were created to observe the SEA change.

The third study was adding vertical elements to the unit cells. Similar to adding horizontal elements, as the thickness of the added edges increased, the thickness of the original geometry was reduced, but the thickness of the base section was not changed. For this work, the visual of the vertically added section, the original section, and the base section is shown in Figure 3.11. In the figure, the color of the base, the additional, and the original sections are green, red, and cream, respectively.

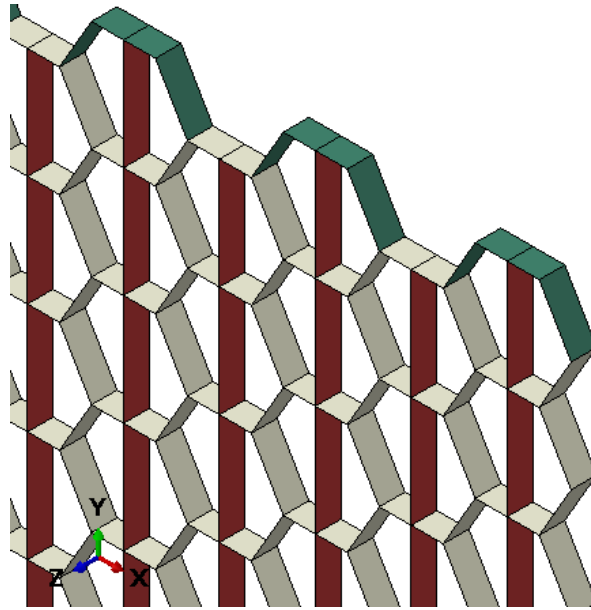
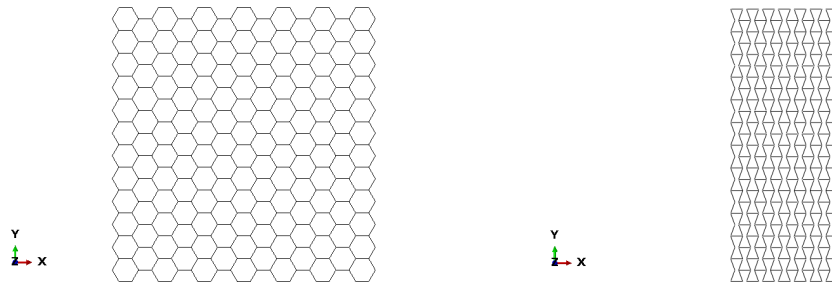


Figure 3.11: Sections of hexagonal lattice structure for additional vertical edge thickness variation

In the additional vertical edge thickness variation study of the hexagonal shape, eleven models are created. The thickness of the horizontal edges is decreased from 0.3 mm to 0.073 mm, while the thickness of the vertical edges is increased from 0 mm to 0.4 mm.

In the fourth and fifth studies, the angle of the unit cell was changed. The changing angle was shown as  $\theta$  in Figure 3.1. In the fourth study, the thicknesses were kept constant while the angle was changed. In this case, the weight was preserved, but the relative density increased with the decrease in the angle. Figure 3.12 below shows the difference between hexagonal lattice structures consisting of  $120^\circ$  and  $70^\circ$  unit cells. The lattice structure consisting of the  $70^\circ$  unit cell is denser. In these studies, models were not analyzed at angles lower than  $70^\circ$  since at  $60^\circ$ , the two corners of the unit cell touch each other anyway. Seventeen models were created from  $120^\circ$  to  $70^\circ$  for the fourth and fifth parametric studies.



(a) Structure for hexagonal geometry with unit angle  $120^\circ$  (b) Structure for hexagonal geometry with unit angle  $70^\circ$

Figure 3.12: Difference of hexagonal lattice geometries with two different angles

Since the length of the structure changes with the angle change, the amount of compression applied to the upper plate should also be changed. When applying displacements, it is necessary to ensure that the compression amount is greater than the locking strain. Since the relative density changes with the angle change in the fourth study, the locking strain value of each model will be different. The relative density of the  $120^\circ$  model is 0.0693, the theoretical locking strain is 0.903, while the relative density of the  $70^\circ$  model is 0.146, the theoretical locking strain is 0.796. When we look at their lengths, the length of the  $120^\circ$  model is approximately 104 mm, the length of the  $90^\circ$  model is 120 mm, and the length of the  $70^\circ$  model is approximately 113 mm. When we consider all these, a displacement of 96 mm was applied to the  $120^\circ$  model, a displacement of 111 mm to the  $90^\circ$  model, and a displacement of 104 mm to the  $70^\circ$  model.

In the fifth study, while changing the angle the thickness was changed to maintain the relative density. As the angle decreased from  $120^\circ$  to  $70^\circ$ , the thickness decreased from 0.3 mm to 0.143 mm. In this case, while the theoretical locking strain remained constant since the length changed, the given displacement values increased from  $120^\circ$  to  $90^\circ$  and decreased from  $90^\circ$  to  $70^\circ$ . The displacement values of the  $100^\circ$  model and the  $80^\circ$  models, which have the same total length, were given equally.

### 3.2.4 Re-entrant Lattice Structures

The re-entrant lattice structure was created by shifting seven and twelve unit cells in x-direction and y-direction, respectively, like the hexagonal lattice. The unit cell of the re-entrant structure is given in Figure 3.1b, and its body is given in Figure 3.13.

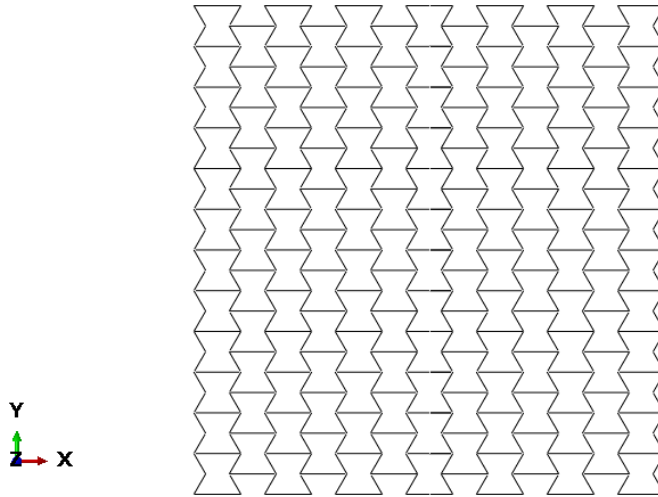


Figure 3.13: Re-entrant lattice structure

It is the base structure for the five studies. For creating a same-weight model with the hexagonal model, the thickness is set to 0.225 mm. The geometrical and mass properties of the base model are given in Table 3.2

Edge Thickness	0.225 mm
Angle of Unit	60°
Unit height	8.66 mm
Unit Width	15 mm
Relative Density	0.0693
Theoretical Locking Strain	0.903
Mass	$4.042 \times 10^{-3}$ kg

Table 3.2: Properties of base re-entrant lattice

Again, three regions were created while changing the thickness of the inclined and horizontal edges relative to each other. The thickness of the base region was kept constant. The maximum value for the horizontal edge was 0.4 mm, and the minimum

value was 0.001 mm. When the horizontal edge was 0.4 mm, the inclined edges were set to 0.056 mm, and when the horizontal edge was 0.001 mm, the inclined edges were set to 0.442 mm. In Figure 3.14, the horizontal edges are cream-colored, the inclined edges are red, and the base edges are green.

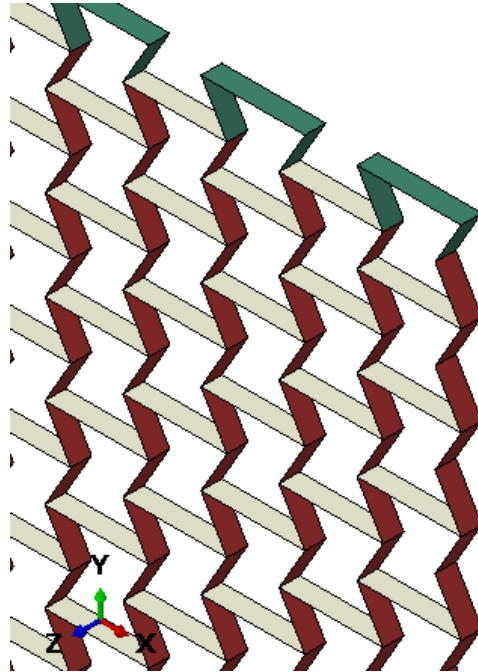


Figure 3.14: Sections of re-entrant lattice structure for vertical and horizontal thickness variation

If horizontal edges are added to the original re-entrant lattice model and the thickness of the added horizontal edges is increased from 0 mm to 0.8 mm, the thickness of the original geometry should also be reduced from 0.225 mm to 0.027 mm. While doing this, the thickness of the edges at the border of the top and bottom plates was not changed. Visually, when looking at the re-entrant shape with the horizontal edge added, the red-colored parts show the added parts, the cream-colored parts show the original geometry, and the green parts show the parts at the border of the top plate, see Figure 3.15. There are sixteen models for this study.

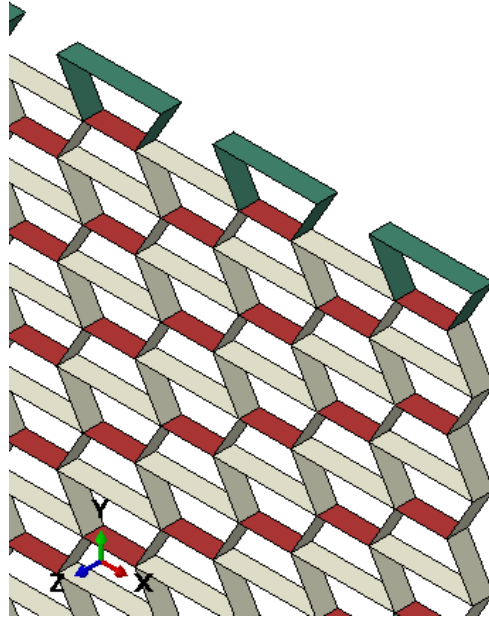


Figure 3.15: Sections of re-entrant lattice structure for additional horizontal edge thickness variation

When we add vertical edges to the re-entrant model, sections are formed as in Figure 3.16. The cream-colored area represents the original shape of the re-entrant model, the red area represents the added vertical edges, and the green area represents the base areas.



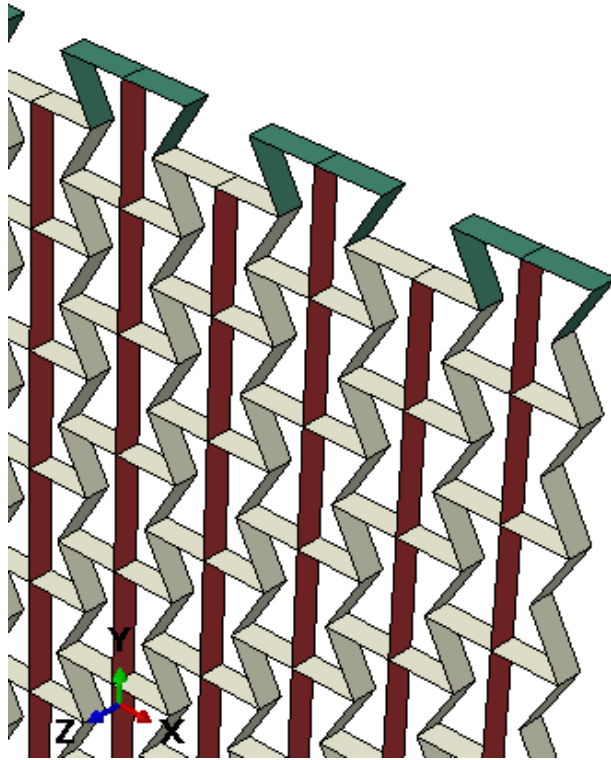
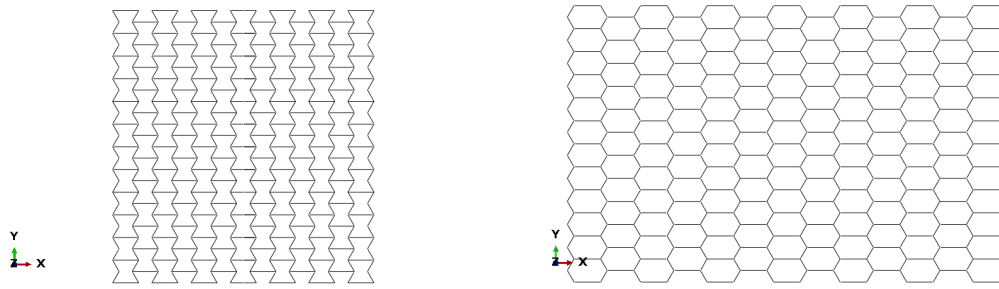


Figure 3.16: Sections of re-entrant lattice structure for additional vertical edge thickness variation

The thickness of the added edges was increased from 0 mm to 0.4 mm, while the thickness of the original geometry was reduced from 0.225 mm to 0.054 mm. Eleven models were created in this range.

Unlike the hexagonal lattice structure, the variable angle of the re-entrant model was taken from a different corner. This angle is shown as  $\theta$  in Figure 3.1b. In this case, the angle of the model was increased from  $60^\circ$  to  $120^\circ$ , and the relative density decreased as the angle increased. In Figure 3.17,  $60^\circ$  and  $120^\circ$  models can be seen.



(a) Structure for re-entrant geometry with unit angle  $60^\circ$  (b) Structure for re-entrant geometry with unit angle  $120^\circ$

Figure 3.17: Difference of hexagonal geometries with two different angles

In the fourth parametric study, since only the angle changed and the thickness remained constant, the relative density decreased, and the theoretical locking strain increased from  $60^\circ$  to  $120^\circ$ . Again, since the length changed with the angle change, the applied displacement value of each model should be different. The longest geometry, the  $90^\circ$  model, was compressed by 115 mm, while the  $60^\circ$  model was compressed by 96 mm, and the  $120^\circ$  model was compressed by 101 mm. The length of the  $60^\circ$  and  $120^\circ$  models is approximately 104 mm.

In the fifth parametric study, to maintain the relative density, the thickness was increased from 0.225 mm at  $60^\circ$  to 0.375 mm at  $120^\circ$ . In this case, since the theoretical locking strain in all models was 0.903, all models were compressed to 0.924 strain. The applied displacement values were found by multiplying the length of the models by 0.924. Nineteen models were created for the re-entrant model's fourth and fifth parametric studies.

### 3.2.5 Chiral Lattice Structures

The unit cell widths of the hexagonal and re-entrant models were greater than their lengths. The unit cell width in both base models was 15 mm, while its length was approximately 8.66 mm. However, the length and width of the chiral unit cell were equal. The length and width of the  $135^\circ$  main model were approximately 9.24 mm. Therefore, eleven repetitions in the x-direction of the chiral cell were chosen to make

the width of the structure close to 100 mm. The number of repetitions in the y-direction was the same as in the other models. In this case, the width of the main model was approximately 99 mm, and its length was approximately 111 mm. The main model made of 135° unit cells is given in Figure 3.18.

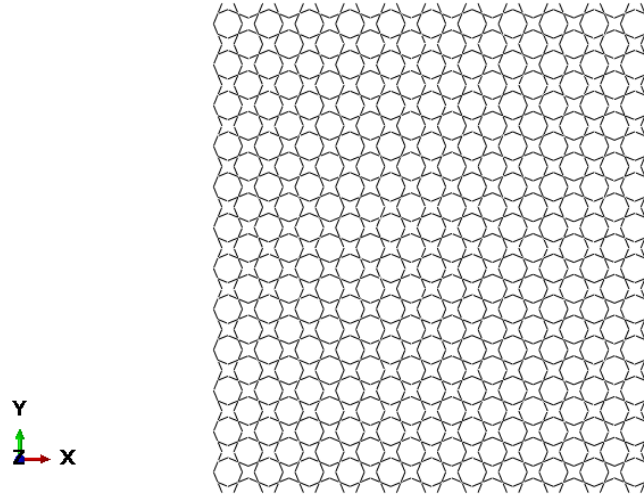


Figure 3.18: Chiral lattice structure

The thickness of the chiral main model was chosen as 0.15 mm to have a similar weight to the other two models. Since there was a small difference in relative density, there were also small differences in theoretical locking strain and weight compared to the other two models. The numerical values of the properties for the main model of chiral lattice are given in Table 3.3:

Edge Thickness	0.15 mm
Angle of Unit	135°
Unit height	9.24 mm
Unit Width	9.24 mm
Relative Density	0.0703
Theoretical Locking Strain	0.902
Mass	$4.18 \times 10^{-3}$ kg

Table 3.3: Properties of base chiral lattice

As in the other two models, the thickness of the close-to-vertical and close-to-horizontal edges in the chiral lattice was changed in the first study. While the

thickness of close-to-horizontal edges were decreased from 0.275 mm to 0.025 mm, the close-to-vertical edges were increased from 0.025 mm to 0.275 mm, and eleven models were created. Figure 3.19 shows close-to-horizontal, close-to-vertical, and base sections.

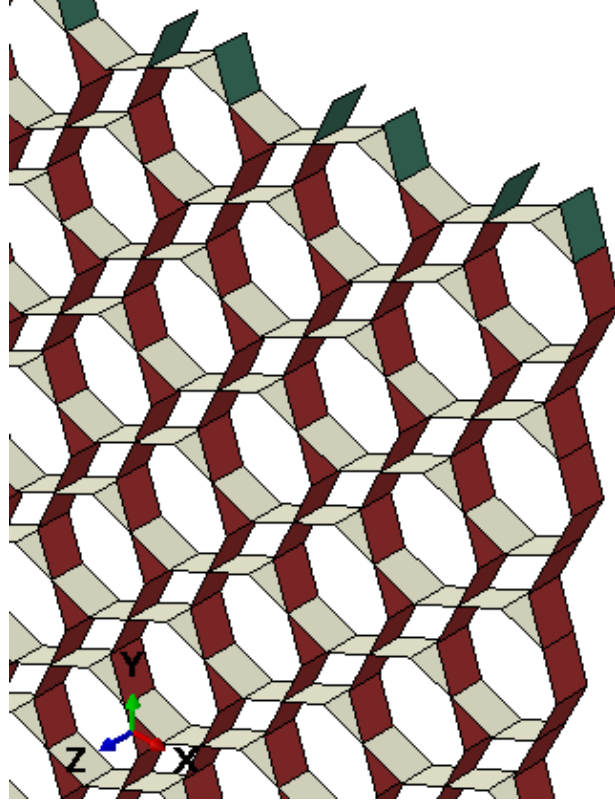


Figure 3.19: Sections of chiral lattice structure for vertical and horizontal thickness variation

For the study where a horizontal edge was added to unit cells, fourteen models were created. While the thickness of the horizontal element in the first model was taken as 0 mm, the thickness of the horizontal element in the last model became 0.25 mm. However, while the thickness of the original geometry of the first model was 0.15 mm, the thickness of the original geometry of the last model was decreased to 0.072 mm. The sections for this study are visualized in Figure 3.20.

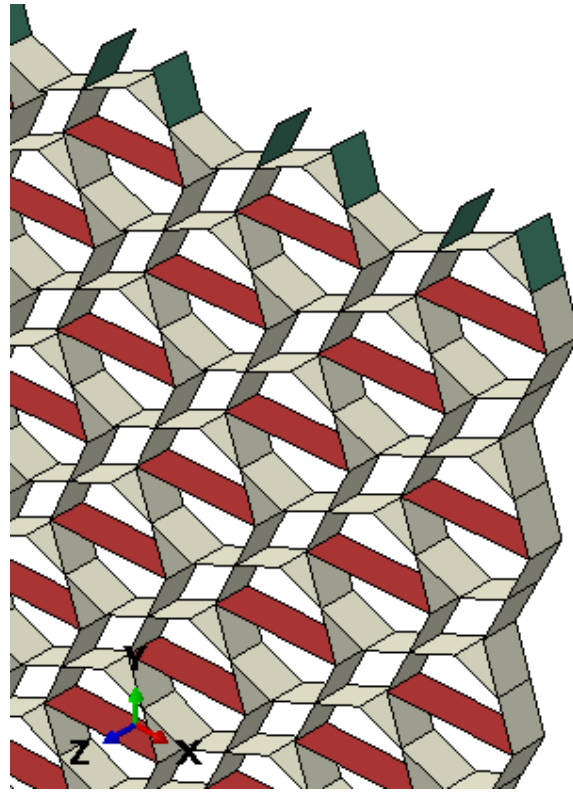


Figure 3.20: Sections of chiral lattice structure for additional horizontal edge thickness variation

Fourteen models were created for the study, where vertical elements were added. Since the lengths and widths of the unit cells are the same, the thickness changes are the same as when we added horizontal edges. The sections of these models are shown in Figure 3.21.

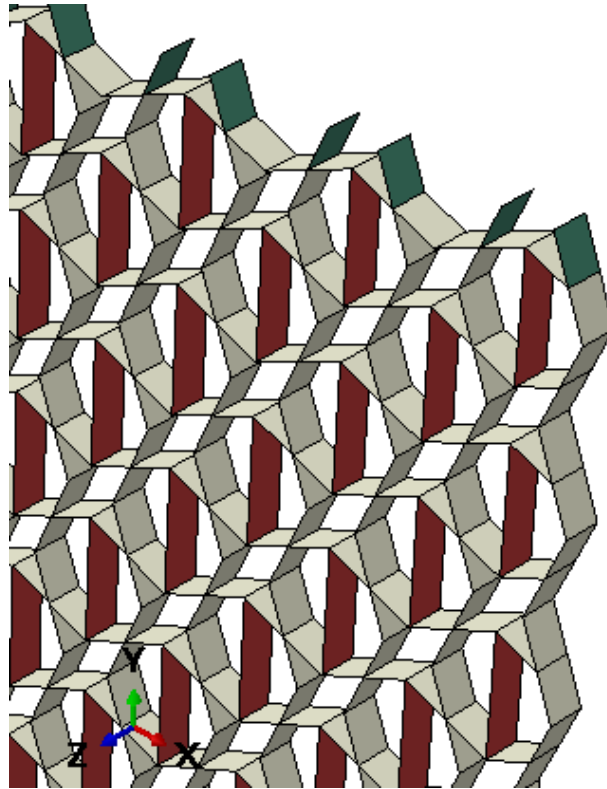
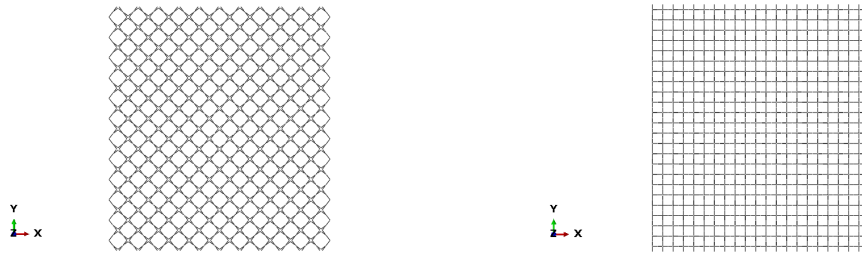


Figure 3.21: Sections of chiral lattice structure for additional vertical edge thickness variation

For angle change studies, twenty-one models were created for chiral lattice. Angle values were studied from  $105^\circ$  to  $235^\circ$ . Figure 3.22 below shows the  $105^\circ$  structure and the  $180^\circ$  structure. Due to the geometric shape of the chiral unit cell, structures created with degrees above and below  $180^\circ$  are identical. In other words, there is a great visual similarity between the structure created with a  $135^\circ$  unit cell and the structures created with  $225^\circ$  unit cells. The only difference between the two is that the  $225^\circ$  structure looks like a half-unit shift of the  $135^\circ$  structure.



(a) Structure for chiral geometry with unit angle  $105^\circ$  (b) Structure for chiral geometry with unit angle  $180^\circ$

Figure 3.22: Difference of chiral geometries with two different angles

In the first study, where the angle was changed, the thickness did not change, so the relative density changed. In the second study, the thickness was 0.111 mm for  $105^\circ$ , 0.176 mm for  $180^\circ$ , and 0.138 mm for  $235^\circ$ . For each model, the relative density, theoretical locking strain, and lengths were calculated, and appropriate displacement values were applied.

### 3.3 Methods of Computation

#### 3.3.1 Computation of Plateau Stress, EA, and SEA

The definitions of plateau stress, EA, and SEA are briefly given in Chapter 1. In short, the plateau stress is the mean stress value between the critical strain and the locking strain of the compressed structure, EA is the area of the stress-strain diagram between these two strains, and the SEA value is EA divided by the weight. These three parameters are essential when examining the energy absorption capabilities of structures. This section presents how these values are calculated for the lattice geometries. The equations are respectively:

$$\sigma_p = \frac{\int_{\epsilon_{cr}}^{\epsilon_d} \sigma(\epsilon) d\epsilon}{\epsilon_d - \epsilon_{cr}} \quad (3.3)$$

$$EA = \int_{\epsilon_{cr}}^{\epsilon_d} \sigma(\epsilon) d\epsilon \quad (3.4)$$

$$SEA = \frac{\int_{\epsilon_{cr}}^{\epsilon_d} \sigma(\epsilon) d\epsilon}{\rho_s \bar{\rho}}, \quad (3.5)$$

where  $\bar{\rho}$  is relative density and  $\rho_s$  is material density of the structure.  $\epsilon_d$  and  $\epsilon_{cr}$  are the locking strain and critical strain values. Critical strain is a strain of the first peak stress. Locking strain corresponds to the densification point of the cellular bodies. These two strain points should be obtained from stress-strain curves. Although defining locking strain is complicated, the critical strain point is generally clear. Thus, computation of locking strain should be described.

For locking strain, a theoretical equation is given in Equation (3.2), but it is valid for simple hexagonal geometries. So, for all analyses, a locking strain has to be defined. Thus, all models are compressed beyond the theoretical locking strain value, and a slope is defined between 0.25 and 0.75 strains (it is assumed that the range between 0.25 and 0.75 strains is in the plateau region for all models), which can be called the *middle* slope. Then using four consecutive data points all slope values in the strain range from 0.25 to 0.75 are computed. Then the biggest value of these slope values corresponds to the middle slope. For example, assume there exist one hundred stress and strain data between 0.25 and 0.75 strains. Ninety-seven slope values are



calculated using each of the four stress-strain data sets. These slopes are the average values of each quart. The value of a quart is the average value of the slope of the first and second stress-strain values, the slope of the second and third stress-strain values, and the slope of the third and fourth stress-strain values. The middle slope is the biggest value of these Ninety-seven slopes. It is later used to compare the slopes of the locking regions. Slopes of the densification regions are calculated from ten stress-strain data points. They are taken as the last ten strain values that are lower than the theoretical locking strain. The average of these ten data points is called as the *densification* slope.

In stress-strain diagrams, the middle and densification slopes are compared to find locking strains. If the densification slope is smaller than the middle slope, the locking strain is the theoretical locking strain, which is given in Equation 3.2. If the densification slope is bigger than the middle slope, a line with the slope of the densification slope is drawn from the theoretical locking strain, and the strain value where it cuts the strain axis is found. It is the new locking strain value, and a new densification slope can be found following the same procedure and compared with the middle slope. However, there is a limitation to prevent the locking strain from becoming too small and unfeasible. If the locking strain correction exceeds ten percent of the strain space which is the total compressive strain, it is set as ten percent of the strain range. In the second and third corrections, the limitation is twenty and forty percent of the strain range. In Figure 3.23, the stress-strain diagram of the chiral angular model ( $145^\circ$ ) with the thickness of 0.15 mm can be seen. In this diagram, there are three corrections, and the limitation is applied in each correction. The theoretical locking strain of this model is 0.91. After the corrections, the locking strain of 0.74 was calculated. In Figure 3.24, same stress-strain diagram is given but without limitation. In this model, the locking strain of 0.67 is found.

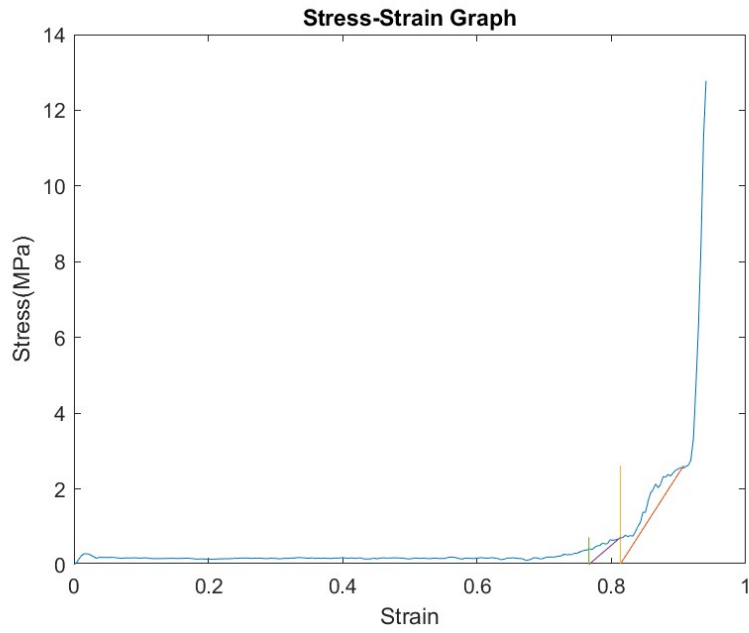


Figure 3.23: Stress strain diagram of the chiral angular model ( $145^\circ$ ) with thickness of 0.15 mm and its densification slopes, with limitation three locking strain correction is applied

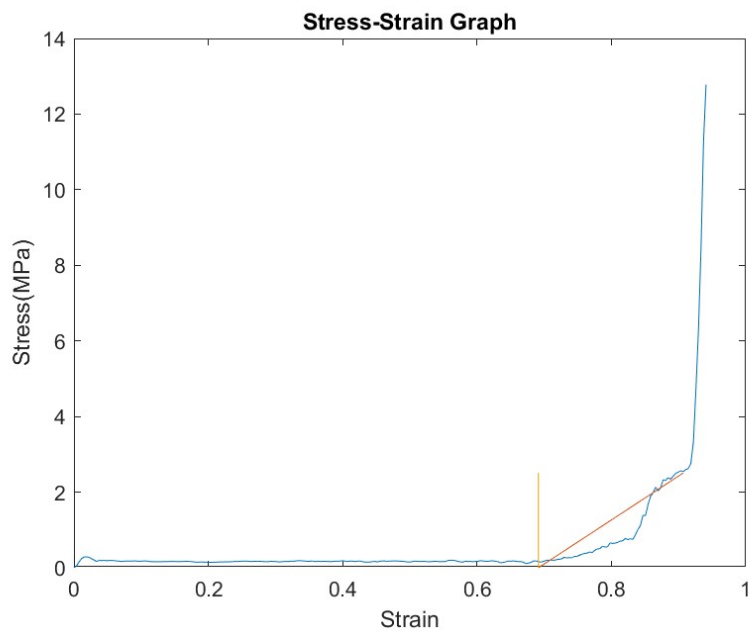


Figure 3.24: Stress strain diagram of the chiral angular model ( $145^\circ$ ) with thickness of 0.15 mm and its densification slopes, without limitation one locking strain correction is applied

The stress is calculated by dividing the force on the upper plate by the cross-sectional area of the lattice structure. The width of the hexagonal lattice is given as 100 mm. The depth of all lattices is 2 mm. In this case, the stress is calculated by dividing the force by  $200 \text{ mm}^2$  in the models of the hexagonal lattice with no angle change. Note that the area changes in each model. After finding the locking strain on the stress-strain graph, the plateau region is found after the critical strain is defined as the strain where the first stress peak occurs. The plateau stress is computed as the average of the stresses in this region. In Figure 3.25, the plateau range and plateau stresses are shown on the stress-strain graphs for model mentioned in the previous paragraph.

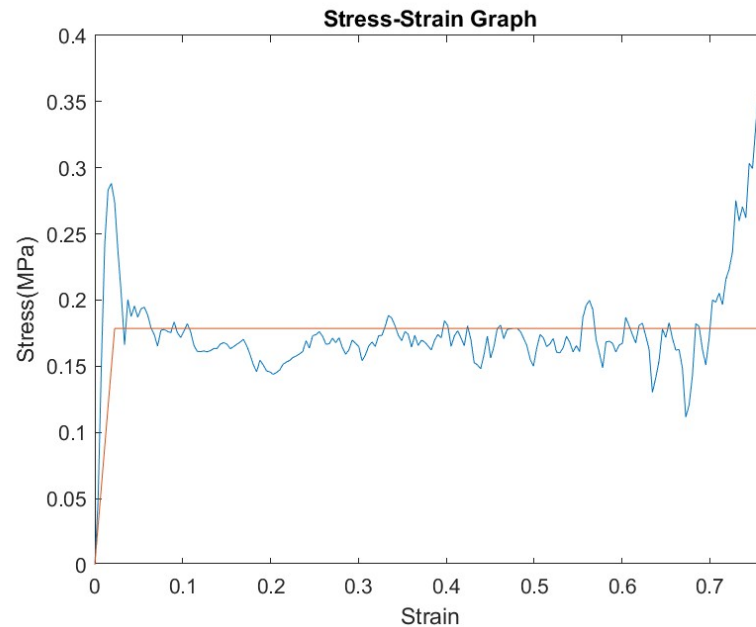


Figure 3.25: Plateau stress of the chiral angular model ( $145^\circ$ ) with thickness of 0.15 mm

Once the plateau stress, locking strain, and the critical strain are computed, the EA and SEA values are computed Equations (3.4) and (3.5). However, SEA can also be calculated from the energy outputs on the structure. A comparison of these two approaches for the computation of SEA values is given in Appendix B for three base models.

### 3.3.2 Computation of Poisson's Ratio

The Poisson's ratio is a material property that quantifies the relationship between axial and transverse strain when a material is stretched or compressed, and it can be defined as:

$$\nu = -\frac{\text{Transverse Strain}}{\text{Axial Strain}} \quad (3.6)$$

As in the study of Luo et al. [22], in analyses performed on Lattice geometries, the Poisson's ratio can be found by the horizontal and vertical displacements of four points in the middle of the structure in the longitudinal direction and the outermost points in the horizontal direction. For long lattice structures, calculating from four points taken from the middle region in the longitudinal direction may prevent making a correct inference because, in some models, the middle region of the structure in the longitudinal direction may be deformed a lot. In contrast, the upper and lower parts may be deformed less. Therefore, Poisson's ratio calculation will yield more accurate results by taking more points from the structure, like the study of Zhang et al. [23]. In this thesis, while calculating the Poisson's ratio, it is aimed to consider points from each unit cell in the longitudinal direction. In addition, not only the outermost points in the horizontal direction are considered. In the computation of Poisson's ratio, points from the central region of the lattice structures are also considered. For example, the points taken from the hexagonal lattice structure are seen in Figure 3.26. Poisson's ratio calculation includes the displacement of a total of 47 points on the hexagonal structure. The longitudinal displacement in Equation (3.6) is calculated from the displacement of the upper plate. The lateral displacement is calculated from the horizontal displacements of 46 points taken from the structure which are shown in red. In Figure 3.26, there are twelve red dots on the structure's far right and twelve on the far left. The average of twelve pairs is calculated after calculating the x-direction displacement of each right-left point pair relative to each other. Similarly, for the 11 points on the right and left of the middle region, the x-axis displacement of each pair relative to each other is calculated and averaged. Then, the x-displacements from the outer region are divided by the distance of outer nodes, and the x-displacements from the inner region are divided by the distance of inner nodes to find strains. The average

of the x-direction strains calculated in the outer and inner regions is calculated and divided by the y-direction strain to calculate the Poisson's ratio. Similar sets of points are generated for the computation of Poisson's ratio for re-entrant and chiral models.

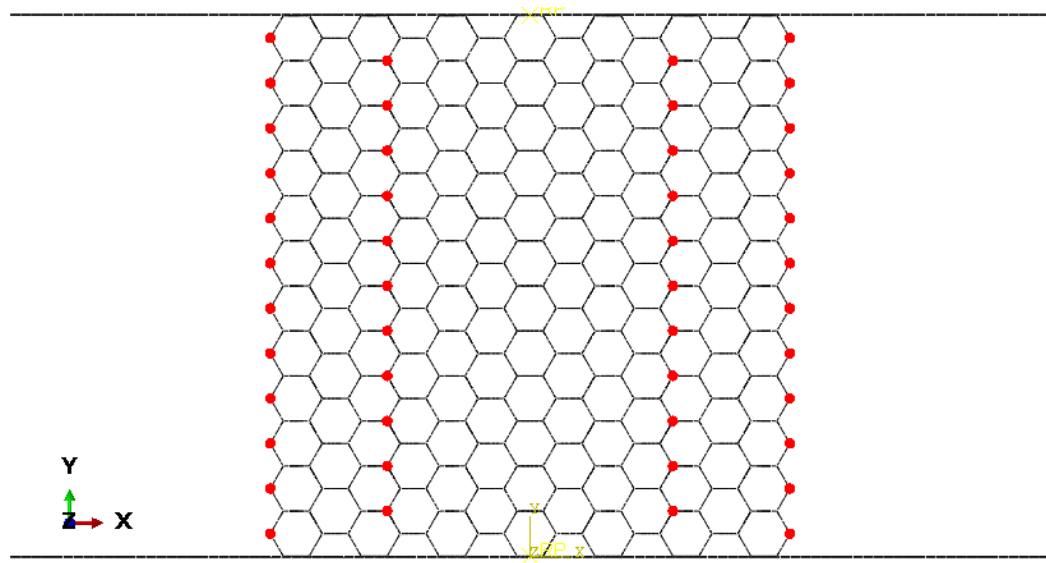


Figure 3.26: Nodes for Poisson's ratio calculation of hexagonal lattice

The computation of Poisson's ratio can be more precise by increasing the points taken. Although Poisson's ratio in this thesis is calculated using the method explained above, an alternative approach is also considered. In the alternative approach, all the left and right outermost points of the structure are included in the computation. The results of two approaches are compared in Appendix C.



## CHAPTER 4

### RESULTS

#### 4.1 Introduction

As presented in Chapter 1, this study claims that when the energy absorption capabilities of lattice structures are compared with Poisson's ratio, the structures with the highest energy absorption are generally those with a Poisson's ratio around zero. As mentioned in Section 3.2, fifteen different parametric models were created to defend this argument. The outputs of the models are presented in this chapter. However, Poisson's ratio of all the models created did not show a change from negative to positive or positive to negative with the parameter change. Therefore, this chapter does not show the outputs of all parametric models.

The Poisson's ratio of the base hexagonal lattice structure is positive. However, the Poisson's ratio becomes negative in all five parametric studies of the hexagonal lattice. Therefore, all the outputs of the hexagonal lattice structure are presented in this chapter. The base model of the re-entrant structure has a negative Poisson's ratio. Of the five parametric studies conducted for this model, only the second (study with added horizontal edges), the fourth, and fifth (studies with angle change) show a positive Poisson's ratio or approach to zero. Therefore, only the results of these three parametric studies are shared in this chapter. While the base geometry of the chiral model has a positive Poisson's ratio, except for the first parametric study (the study in which the thicknesses of the horizontal and inclined elements were changed relative to each other), it was observed that Poisson's ratio becomes negative in all four parametric studies and they are shared in this chapter. The results of the three parametric studies not shared in this chapter are given in Appendix A.

When structures are compressed, Poisson’s ratios are computed with the method presented in Section 3.3 may vary depending on the amount of compression. The base hexagonal lattice model can be given as an example. In Figure 4.1, the graph of the Poisson’s ratio of the hexagonal model is given according to the strain value. In addition, six different predetermined strain levels are drawn as lines. When Poisson’s ratio in these strain values is examined, it is calculated as 1.304 when 0.004, 1.023 when the strain is approximately 0.015, 0.744 when the strain is 0.05, 0.479 when the strain is 0.1, 0.324 when the strain is 0.2, and 0.276 when the strain is 0.5.

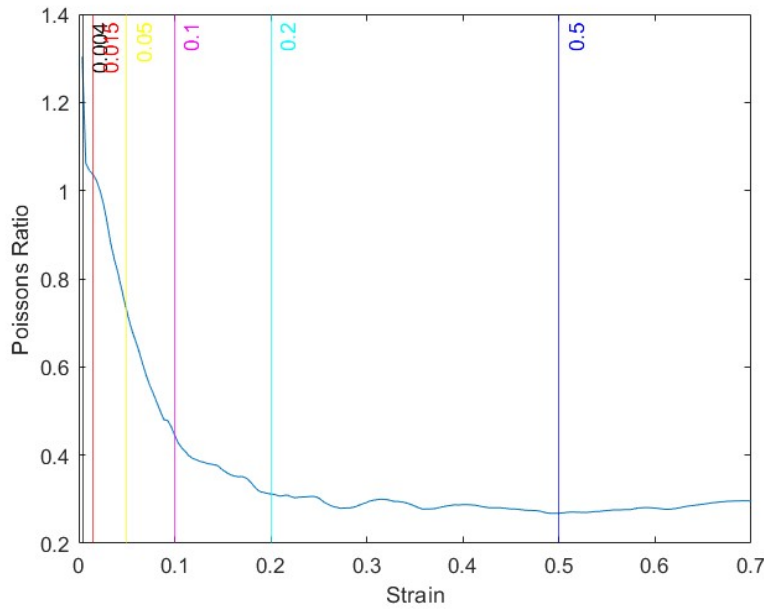


Figure 4.1: Variation of Poisson’s ratio of the hexagonal base model with strain

Since Poisson’s ratio changes with the strain, only Poisson’s ratios computed at 0.015 strain are presented in this section. The value of 0.015 was chosen because it was observed that the lattice structures remained almost completely in the elastic range at this strain. The strain range in which each parametric model remains completely elastic differs. Still, since this value is suitable for most models, the results of the same strain value are compared in all parametric studies. The general stress distribution on the structure can be examined to check whether it is in the elastic region. When the stress distributions of all parametric studies are discussed, although, in some models, the Von Misses stress values in small local areas at 0.015 strain value can reach 76 MPa, which is the yield stress, these regions are very local. Furthermore,



when the Poisson's ratios at different strain levels are compared with the analytical values (whenever available) or unit cell calculations, the 0.015 strain value was found to be the most appropriate. The analytical calculation method and comparisons are given in detail in Appendix E. For these reasons, in this section, Poisson's ratios of all parametric models are presented at 0.015 strain value. However, Poisson's ratios at other strain values (0.004, 0.05, 0.1, 0.2) are also given in Appendix A together with the strain value of 0.015 for completeness. In this chapter, numerical outputs of compression analyses are given, but to better understand the compression behavior, deformed geometries of some hexagonal lattices at 0.2 and 0.5 strain levels are shown in Appendix G.

In this chapter, SEA values and Poisson's ratios are shown in tabular form and on the graph according to the changing parameter. In the given tables, the first three columns show the parametric changes in the models. The SEA value is given in the fourth column, and the Poisson's ratios are presented in the fifth column. In the SEA column, three cells are colored blue because these cells have higher SEA than others. If there are models with the same SEA value, the number of blue-colored unit cells can exceed three. In the Poisson's ratio column, some cells are colored mustard. The mustard-colored cells mean that Poisson's ratio changes its sign. The x-axes in the graphs show the thickness or angle in increasing order: the left y-axes show Poisson's ratio, and the right y-axes show the SEA value. For clarity, the plots showing the results of Poisson's ratio and SEA values are shown in the same color as the corresponding axes. Mustard is used for Poisson's ratio, and blue is used for the SEA value. In addition, a dashed line, which is zero Poisson's ratio line, is added to the graphs.

## **4.2 Results of Hexagonal Lattices**

As mentioned in the previous section, Poisson's ratio changes from positive to negative in the five parametric studies with the hexagonal unit cell. The outputs of the first parametric study, the change of horizontal and inclined edge thicknesses relative to each other, are given in Table 4.1 and Figure 4.2. The first three columns in the table show the thicknesses of the sections in Figure 3.9. The thickness of the regions

close to the upper and lower plates where the original thickness is preserved and given in the first column. The calculated SEA values are given in the fourth column, and Poisson's ratios at 0.015 strain are given in the fifth column. The variation of Poisson's ratio and the SEA value with the thickness of the horizontal edge can be seen in Figure 4.2. The thickness of the horizontal edges is 0.3 mm in the unchanged hexagonal model. As the thickness of the horizontal edges decreases, Poisson's ratio decreases, and after a specific thickness value, it becomes negative. It can be observed that the SEA first increases and then decreases with the decrease in thickness. In the region where the SEA is the largest, Poisson's ratio starts to decline rapidly, but it cannot be said that the SEA has the highest value for the region where the Poisson's ratio changes its sign. However, in the following parametric studies, the models where the SEA is the largest are very close to the transition point of Poisson's ratio.

Thickness of Sections (mm)			SEA (kj/kg)	Poisson's ratio
Base	Horizontal	Inclined		
0.3	0.350	0.276	0.740	1.030
0.3	0.300	0.300	0.887	1.023
0.3	0.250	0.324	1.114	1.017
0.3	0.200	0.348	1.199	1.009
0.3	0.150	0.373	1.282	0.983
0.3	0.125	0.459	1.327	0.955
0.3	0.100	0.397	1.185	0.774
0.3	0.075	0.483	1.060	0.310
0.3	0.050	0.495	0.833	0.138
0.3	0.025	0.507	0.839	-0.183
0.3	0.010	0.440	0.722	-0.379
0.3	0.008	0.516	0.666	-0.352
0.3	0.005	0.443	0.473	-0.238
0.3	0.001	0.446	0.392	-0.147

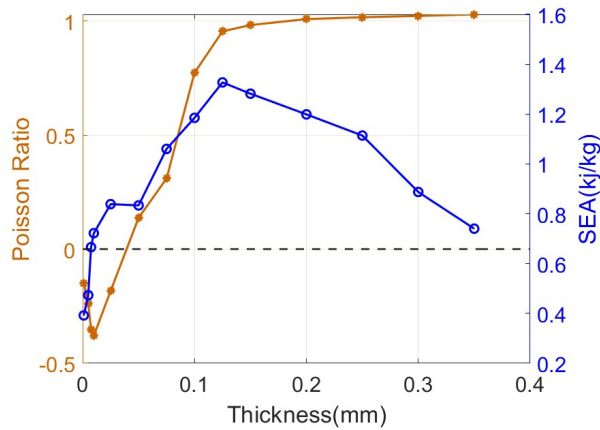


Table 4.1: Model parameters and outputs of the first parametric study of the hexagonal lattice

Figure 4.2: Variation of Poisson's ratio and SEA values with the thickness change for the first parametric study of the hexagonal lattice

In the second parametric study, where horizontal edges are added, and their thicknesses are changed, the SEA and Poisson's ratio values are given in Table 4.2. The first column of the table shows the thickness of the regions close to the plates where the original thickness is constant. The second column gives the thickness of the original hexagonal shape. The thickness of the added horizontal edges is shown in the third column. Note that while the thickness of the added horizontal

edge increases, the thickness of the original hexagonal shape decreases to keep the weight constant. As the thickness of the added horizontal edges increases, the SEA value first increases and then decreases. It can be seen that Poisson's ratio sign change occurs in the region where SEA is the maximum. In this parametric study, it is seen that the SEA value decreases continuously after a specific thickness value. The reason for this is that the horizontally added edges are thick, and the remaining geometry is too thin. When the thickness of the hexagonal lattice elements becomes too thin, the structure becomes unable to carry loads.

Thickness of Sections (mm)			SEA (kj/kg)	Poisson's ratio
Base	Hexagon	Additional		
0.3	0.300	0.000	0.887	1.023
0.3	0.299	0.001	0.956	1.021
0.3	0.297	0.005	0.959	1.018
0.3	0.293	0.010	1.117	1.011
0.3	0.267	0.050	2.065	0.863
0.3	0.251	0.075	2.070	0.303
0.3	0.234	0.100	1.880	-0.165
0.3	0.226	0.113	1.848	-0.183
0.3	0.218	0.125	1.623	-0.125
0.3	0.210	0.138	1.618	-0.113
0.3	0.202	0.150	1.506	-0.008
0.3	0.185	0.175	1.380	-0.176
0.3	0.169	0.200	1.304	-0.259
0.3	0.136	0.250	1.021	-0.123
0.3	0.103	0.300	0.730	-0.132
0.3	0.037	0.400	0.128	-0.153

Table 4.2: Model parameters and outputs of the second parametric study of the hexagonal lattice

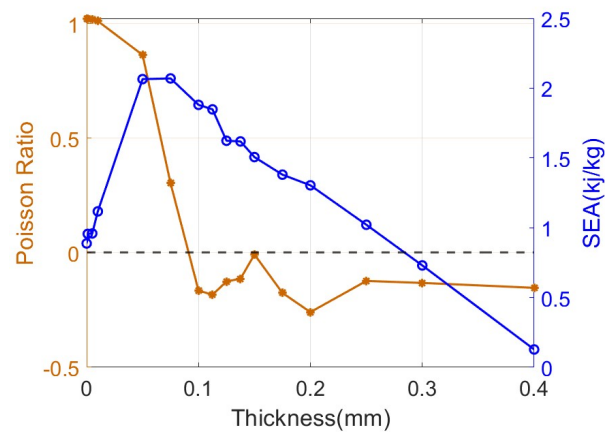


Figure 4.3: Variation of Poisson's ratio and SEA values with the thickness change for the second parametric study of the hexagonal lattice

In the third parametric study, vertical edges are added to the hexagonal unit cells. The thicknesses of the added vertical edges are shown in the third column of Table 4.3. The thickness is increased from 0 mm to 0.526 mm. Accordingly, the thickness of the original hexagonal geometry is reduced, as seen in the second column. Figure 4.4 shows how the SEA and Poisson's ratios change with the thickness of the added edges. As the thickness increases, SEA first increases and then decreases, and Poisson's ratio decreases until the last two models and increases in the last two models. The region where SEA is the maximum is very close to the region where the Poisson's ratio changes sign. Again, the SEA value decreases after a specific

thickness. This is because the original hexagon elements become too thin, and the structure becomes almost unstable.

Thickness of Sections (mm)			SEA	Poisson's
Base	Hexagon	Additional	(kj/kg)	ratio
0.3	0.300	0.000	0.887	1.023
0.3	0.299	0.001	0.900	1.022
0.3	0.297	0.005	0.871	1.023
0.3	0.294	0.010	0.846	1.024
0.3	0.272	0.050	0.837	1.031
0.3	0.243	0.100	0.952	0.969
0.3	0.215	0.150	1.257	0.649
0.3	0.186	0.200	1.450	0.481
0.3	0.158	0.250	1.644	0.356
0.3	0.129	0.300	1.664	0.364
0.3	0.073	0.400	1.135	-0.134
0.3	0.044	0.450	0.907	-1.326
0.3	0.030	0.475	0.753	-1.347
0.3	0.016	0.500	0.563	-1.412
0.3	0.002	0.525	0.303	-0.586
0.3	0.001	0.526	0.298	-0.627

Table 4.3: Model parameters and outputs of the third parametric study of the hexagonal lattice

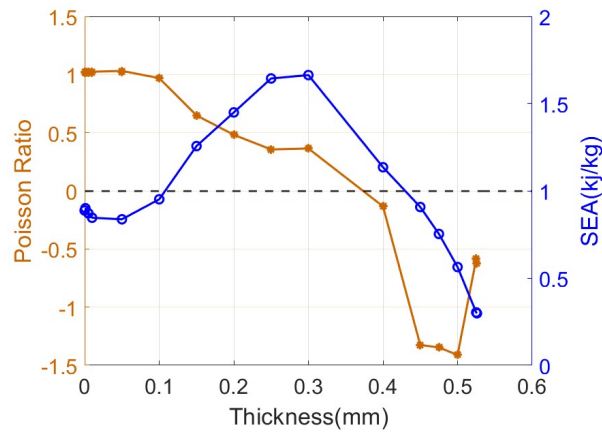


Figure 4.4: Variation of Poisson's ratio and SEA values with the thickness change for the third parametric study of the hexagonal lattice

The variations of SEA and Poisson's ratios while changing the angle, are given in Table 4.4. The relative density increases with the angle since the thickness is kept constant. The angle, thickness, and relative density values are given in the first three columns of the table. The fourth and fifth columns provide the SEA and Poisson's ratios. The base model of the hexagonal lattice is the 120° model. While it has a positive Poisson's ratio at 120°, Poisson's ratio becomes negative for angles smaller than 90°, and the transition in Poisson's ratio occurs in the region where the SEA is the highest. It can be observed more clearly in Figure 4.5.

Angle (Degree)	Thickness (mm)	Relative Density	SEA (kj/kg)	Poisson's ratio
120	0.300	0.069	0.887	1.023
115	0.300	0.070	1.038	1.353
110	0.300	0.071	1.167	1.808
105	0.300	0.074	1.173	2.444
100	0.300	0.078	1.427	3.234
97.5	0.300	0.080	1.365	3.740
95	0.300	0.083	1.415	4.353
93	0.300	0.086	1.395	4.561
91	0.300	0.088	1.497	0.999
90	0.300	0.090	1.431	0.254
89	0.300	0.092	1.474	-1.347
87	0.300	0.095	1.400	-4.664
85	0.300	0.099	1.468	-5.077
82.5	0.300	0.104	1.254	-4.638
80	0.300	0.111	0.873	-4.548
75	0.300	0.126	1.181	-4.233
70	0.300	0.146	0.990	-3.951

Table 4.4: Model parameters and outputs of the fourth parametric study of the hexagonal lattice

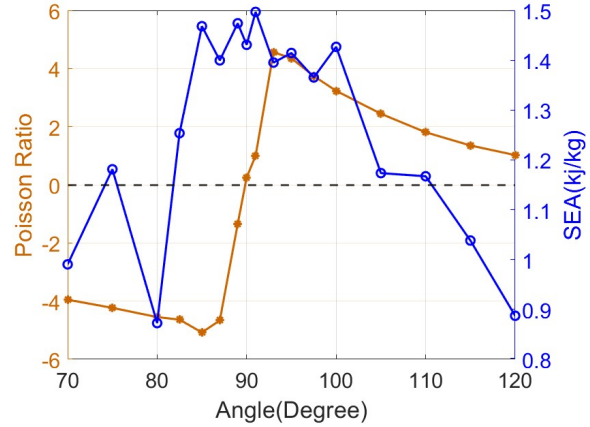


Figure 4.5: Variation of Poisson's ratio and SEA values with the angle change for the fourth parametric study of the hexagonal lattice

In the fifth parametric study, the angle is changed together with the thickness to keep the relative density constant. Again, the angle, thickness, SEA, and Poisson's ratio values are shown in Table 4.5. The outputs are similar to the previous angle change study. Since the thickness decreases with the angle change, there is a general decrease in SEA values. However, it can be said that the region where Poisson's ratio changes sign is the region where the SEA is the highest, like the previous parametric study. In models where the angle is changed, it is seen that SEA reaches high values around 90°. Again, this is an output related to the load-carrying capacity of the inclined edges. The more parallel the edges are to the compression direction, the more energy absorption occurs because it can carry loads.

Angle (Degree)	Thickness (mm)	Relative Density	SEA (kj/kg)	Poisson's ratio
120	0.300	0.069	0.887	1.023
115	0.298	0.069	1.046	1.353
110	0.291	0.069	1.155	1.806
105	0.281	0.069	1.112	2.422
100	0.267	0.069	1.242	3.192
97.5	0.259	0.069	1.242	3.746
95	0.250	0.069	1.281	4.496
93	0.243	0.069	1.173	4.860
91	0.235	0.069	1.208	1.407
90	0.231	0.069	1.317	0.377
89	0.227	0.069	1.215	-0.765
87	0.219	0.069	1.078	-5.196
85	0.210	0.069	1.127	-5.506
82.5	0.199	0.069	0.896	-4.890
80	0.188	0.069	0.812	-4.686
75	0.165	0.069	0.700	-4.291
70	0.143	0.069	0.410	-3.960

Table 4.5: Model parameters and outputs of the fifth parametric study of the hexagonal lattice

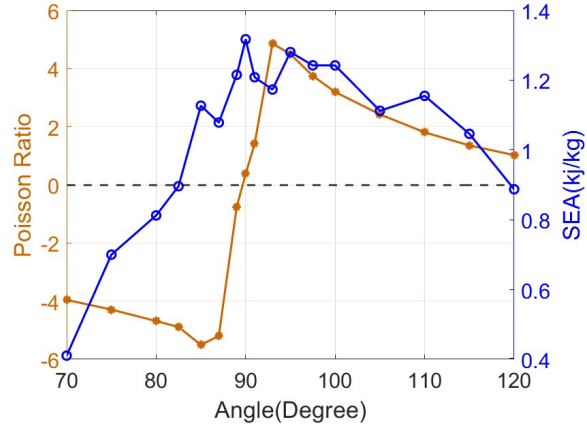


Figure 4.6: Variation of Poisson's ratio and SEA values with the angle change for the fifth parametric study of the hexagonal lattice

### 4.3 Results of Re-entrant Lattices

In the base cell of the re-entrant lattice, Poisson's ratio is negative, and for the three parametric studies, Poisson's ratio approaches zero from the negative side or switches the sign and becomes positive. The results are not shared in the first parametric study because the Poisson's ratio remained negative. The outputs of the second parametric study, in which the horizontal edge is added and its thickness is increased, are given in Table 4.6 and Figure 4.7. For the case where no horizontal edge is added, the edge thickness of the re-entrant lattice is selected as 0.225 mm. To protect the weight, as the thickness of the added horizontal element increases, the thickness of the original geometry decreases. When Poisson's ratios of the models are examined, there is no transition from negative to positive, but as the thickness increases, Poisson's ratio approaches zero. The SEA value first increases and then decreases with the thickness of the added edges. As a result of this parametric study, it cannot be said that the highest value of SEA is seen in the region where Poisson's ratio negative to positive transition is seen, but it can be said that SEA is maximum in the first region where the

Poisson's ratio approaches zero. The structure cannot carry loads with the increased thickness of the added horizontal element and the excessive decrease in the thickness of the other edges. In cases where the thickness of the added horizontal elements exceeds 0.6 mm, the energy absorption ability of the structure has reached a point where it becomes meaningless.

Thickness of Sections in mm			SEA (kj/kg)	Poisson's ratio
Base	Re-entrant	Additional		
0.225	0.225	0.000	0.563	-1.020
0.225	0.225	0.001	0.547	-1.018
0.225	0.224	0.005	0.571	-1.022
0.225	0.223	0.010	0.613	-1.018
0.225	0.200	0.100	1.027	-0.758
0.225	0.194	0.125	1.311	-0.432
0.225	0.188	0.150	1.320	-0.244
0.225	0.182	0.175	1.383	-0.146
0.225	0.175	0.200	1.276	-0.181
0.225	0.163	0.250	1.133	-0.201
0.225	0.151	0.300	1.272	-0.181
0.225	0.126	0.400	0.863	-0.070
0.225	0.101	0.500	0.616	-0.042
0.225	0.076	0.600	0.365	-0.059
0.225	0.052	0.700	0.115	-0.012
0.225	0.027	0.800	0.028	-0.018

Table 4.6: Model parameters and outputs of the second parametric study of the re-entrant model

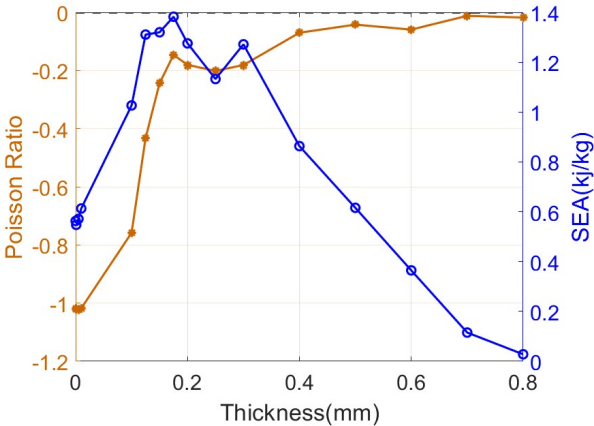


Figure 4.7: Variation of Poisson's ratio and SEA values with the thickness change for the second parametric study of the re-entrant model

In the study where the vertical elements are added and the thicknesses are changed, Poisson's ratios remained negative in all models, so it was not shared here. In the fourth study, where the angle is changed, the transition of Poisson's ratio can be seen in Table 4.7 and Figure 4.8. As the angle approaches from 60° to 85°, Poisson's ratio decreases. From 85° to 95°, it reaches a positive value with a significant increase and decreases again until 120° after 95° but maintains its positive value. The region where SEA is maximum is also around 90°. In this model, the region where SEA is maximum coincides with the region where Poisson's ratio is around zero.

Angle (Degree)	Thickness (mm)	Relative Density	SEA (kj/kg)	Poisson's ratio
60	0.225	0.069	0.563	-1.020
65	0.225	0.063	0.632	-1.222
70	0.225	0.058	0.841	-1.469
75	0.225	0.054	0.771	-1.730
80	0.225	0.050	0.803	-2.062
82.5	0.225	0.049	0.780	-2.331
85	0.225	0.047	0.847	-2.687
87	0.225	0.046	0.805	-1.800
89	0.225	0.045	0.829	0.015
90	0.225	0.045	0.905	-0.027
91	0.225	0.045	0.919	0.473
93	0.225	0.044	0.877	1.726
95	0.225	0.043	0.843	2.301
97.5	0.225	0.043	0.843	2.060
100	0.225	0.042	0.833	1.692
105	0.225	0.041	0.763	1.290
110	0.225	0.041	0.692	0.995
115	0.225	0.041	0.647	0.764
120	0.225	0.042	0.623	0.582

Table 4.7: Model parameters and outputs of the fourth parametric study of the re-entrant model

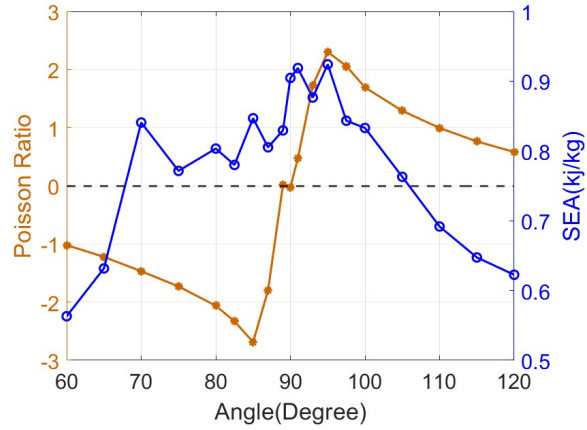


Figure 4.8: Variation of Poisson's ratio and SEA values with the angle change for the fourth parametric study of the re-entrant model

The second angle change study yields very similar results. Since the thickness is increased in this parametric study to maintain the relative density, the SEA values increase slightly compared to the previous parametric angle change study. When looking at Poisson's ratio and SEA values, it is seen that the models with the largest SEA are the models where Poisson's ratio changes from negative to positive. The results of the last parametric study of the re-entrant lattice are shown in Table 4.8 and Figure 4.9.



Angle (Degree)	Thickness (mm)	Relative Density	SEA (kj/kg)	Poisson's ratio
60	0.225	0.069	0.563	-1.020
65	0.248	0.069	0.684	-1.227
70	0.270	0.069	0.930	-1.469
75	0.291	0.069	0.925	-1.722
80	0.312	0.069	1.058	-2.021
82.5	0.321	0.069	1.066	-2.235
85	0.330	0.069	1.206	-2.553
87	0.337	0.069	1.133	-2.501
89	0.343	0.069	1.083	-0.569
90	0.346	0.069	1.328	0.283
91	0.349	0.069	1.351	0.566
93	0.355	0.069	1.314	2.358
95	0.360	0.069	1.394	2.249
97.5	0.366	0.069	1.302	1.900
100	0.371	0.069	1.245	1.666
105	0.378	0.069	1.167	1.300
110	0.381	0.069	1.100	1.000
115	0.380	0.069	1.018	0.772
120	0.375	0.069	0.909	0.596

Table 4.8: Model parameters and outputs of the fifth parametric study of the re-entrant model

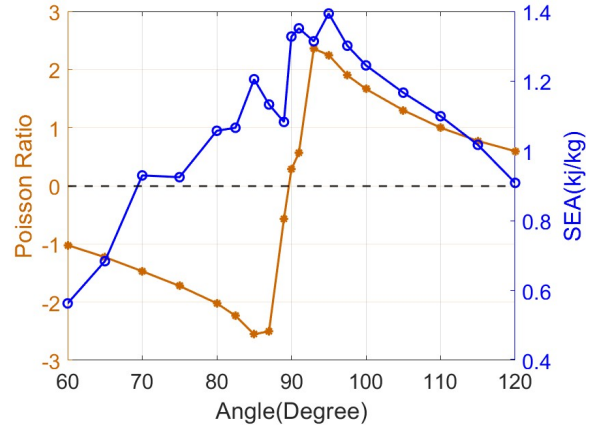


Figure 4.9: Variation of Poisson's ratio and SEA values with the angle change for the fifth parametric study of the re-entrant model

#### 4.4 Results of Chiral Lattices

The first of the parametric studies of chiral lattice, the model in which the thicknesses of the close-to-horizontal and close-to-vertical edges change relative to each other, is not shared here because there is no Poisson's ratio sign change. The results of the study in which the horizontal edge is added are shown in Table 4.9 and Figure 4.10. Since the behavior of SEA changes very rapidly with the addition of a very thin horizontal edge, many models with very thin horizontal edges are created, i.e., the first five data points in Figure 4.10. The largest two values of SEA are found in the models in which the added horizontal edge thickness is 0.01 mm and 0.02 mm. Poisson's ratios of these models are also close to zero. While a serious decrease is seen in SEA as the added edge thickness increases, Poisson's ratio does not change much in a few models. With the further increase of the thickness of the added edge, the thickness of the original structure becomes too thin to carry, and SEA decreases. In this study, the maximum value of SEA is in the region where Poisson's ratio first

approaches zero.

Thickness of Sections in mm			SEA	Poisson's
Base	Hexagon	Additional	(kj/kg)	ratio
0.15	0.150	0.000	0.743	0.660
0.15	0.150	0.001	0.675	0.640
0.15	0.148	0.005	0.810	0.414
0.15	0.148	0.008	0.864	0.190
0.15	0.147	0.010	0.978	0.090
0.15	0.144	0.020	0.972	-0.004
0.15	0.141	0.030	0.913	0.028
0.15	0.137	0.040	0.891	0.025
0.15	0.134	0.050	0.777	0.021
0.15	0.127	0.075	0.706	-0.035
0.15	0.119	0.100	0.796	-0.163
0.15	0.103	0.150	0.855	-0.319
0.15	0.087	0.200	0.771	-0.115
0.15	0.072	0.250	0.664	-0.473

Table 4.9: Model parameters and outputs of the second parametric study of the chiral model

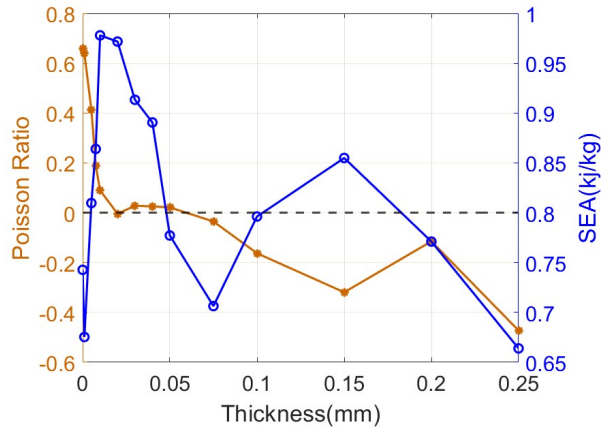


Figure 4.10: Variation of Poisson's ratio and SEA values with the thickness change for the second parametric study of the chiral model

The results of the third parametric study where a vertical edge is added to the chiral lattice are shown in Table 4.10 and Figure 4.11. In this particular study, the Poisson's ratio almost monotonously decreases and shows a clear sign change, while SEA increases almost monotonously with the added vertical edge thickness. However, the region where the Poisson's ratio changes sign is not close to the region where the maximum SEA is found. In the case where we add vertical elements to the chiral lattice and increase its thickness, the added vertical edges affect the load-carrying capacity of the structure. SEA increases up to the additional edge thickness of 0.2 mm and decreases at 0.25 mm. At the value of 0.25 mm, the load-carrying capacity decreases because the thickness of the structures that establish the connection between the vertical elements becomes too low.

Thickness of Sections in mm			SEA (kj/kg)	Poisson's ratio
Base	Hexagon	Additional		
0.15	0.150	0.000	0.743	0.660
0.15	0.150	0.001	0.753	0.663
0.15	0.148	0.005	0.652	0.684
0.15	0.147	0.010	0.655	0.686
0.15	0.142	0.025	0.645	0.669
0.15	0.134	0.050	0.686	0.032
0.15	0.130	0.063	0.743	-0.056
0.15	0.127	0.075	0.813	-0.093
0.15	0.123	0.088	0.962	-0.095
0.15	0.119	0.100	1.123	-0.092
0.15	0.111	0.125	1.361	-0.088
0.15	0.103	0.150	1.439	-0.152
0.15	0.087	0.200	1.687	-0.200
0.15	0.072	0.250	1.454	-0.229

Table 4.10: Model parameters and outputs of the third parametric study of the chiral model

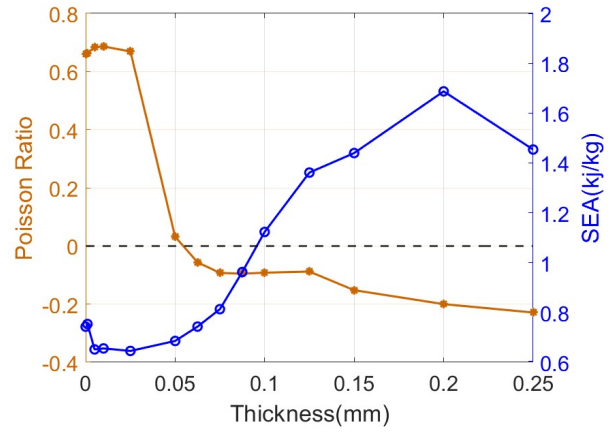


Figure 4.11: Variation of Poisson's ratio and SEA values with the thickness change for the third parametric study of the chiral model

In the study where the angle of the chiral lattice changes, while keeping the edge thicknesses constant, Poisson's ratio shows two sign changes. There is first a change from positive to negative around  $180^\circ$  and then from negative to positive around  $200^\circ$ . The outputs are shown in Table 4.11 and Figure 4.12. The highest value of SEA is obtained in the second sign change region.

Angle (Degree)	Thickness (mm)	Relative Density	SEA (kj/kg)	Poisson's ratio
105	0.150	0.095	0.465	0.594
115	0.150	0.084	0.523	0.611
125	0.150	0.076	0.594	0.674
135	0.150	0.070	0.648	0.660
145	0.150	0.066	0.744	0.694
155	0.150	0.063	0.749	0.716
165	0.150	0.061	0.820	0.467
170	0.150	0.060	0.784	0.210
175	0.150	0.060	0.749	0.045
177	0.150	0.060	0.779	-0.058
179	0.150	0.060	0.782	-0.058
180	0.150	0.060	0.706	-0.006
181	0.150	0.060	0.782	-0.058
183	0.150	0.060	0.779	-0.058
185	0.150	0.060	0.742	-0.352
190	0.150	0.060	0.718	-0.239
195	0.150	0.061	0.894	-0.120
205	0.150	0.063	0.780	0.207
215	0.150	0.066	0.735	0.308
225	0.150	0.070	0.644	0.346
235	0.150	0.076	0.602	0.414

Table 4.11: Model parameters and outputs of the fourth parametric study of the chiral model

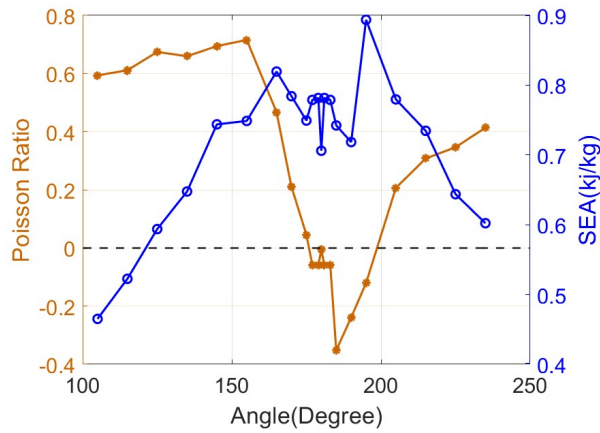


Figure 4.12: Variation of Poisson's ratio and SEA values with the angle change for the fourth parametric study of the chiral model

In the second angular study of the chiral model, the results are similar to those of the first angular study as in the hexagon and re-entrant models. The results are given in Table 4.12 and Figure 4.13. The angle of the base chiral model is  $135^\circ$ . While the thickness of the  $135^\circ$  model is 0.15 mm, the edges become thinner at lower angles. Similarly, the edge thicknesses increase from  $135^\circ$  to  $180^\circ$ . After  $180^\circ$ , the edge thicknesses drop again. This model also shows two distinct regions where the Poisson's ratio changes sign. These are at  $180^\circ$  and  $200^\circ$ . Indeed, the Poisson's ratio finely oscillates around zero for the range  $177^\circ$ - $183^\circ$ . However, as in the case of the previous model, the maximum value of SEA is found in the region where the Poisson's ratio changes its sign from negative to positive, i.e., around  $200^\circ$ .

Angle (Degree)	Thickness (mm)	Relative Density	SEA (kj/kg)	Poisson's ratio
105	0.111	0.070	0.348	0.712
115	0.125	0.070	0.439	0.574
125	0.138	0.070	0.556	0.670
135	0.150	0.070	0.648	0.660
145	0.160	0.070	0.789	0.685
155	0.168	0.070	0.875	0.706
165	0.173	0.070	0.936	0.420
170	0.174	0.070	0.893	0.230
175	0.175	0.070	0.908	0.013
177	0.176	0.070	0.908	-0.009
179	0.176	0.070	0.888	-0.012
180	0.176	0.070	0.760	0.075
181	0.176	0.070	0.889	-0.012
183	0.176	0.070	0.911	-0.009
185	0.175	0.070	0.910	-0.296
190	0.174	0.070	0.902	-0.233
195	0.173	0.070	0.963	-0.136
205	0.168	0.070	0.881	0.202
215	0.160	0.070	0.783	0.299
225	0.150	0.070	0.668	0.346
235	0.138	0.070	0.566	0.410

Table 4.12: Model parameters and outputs of the fifth parametric study of the chiral model

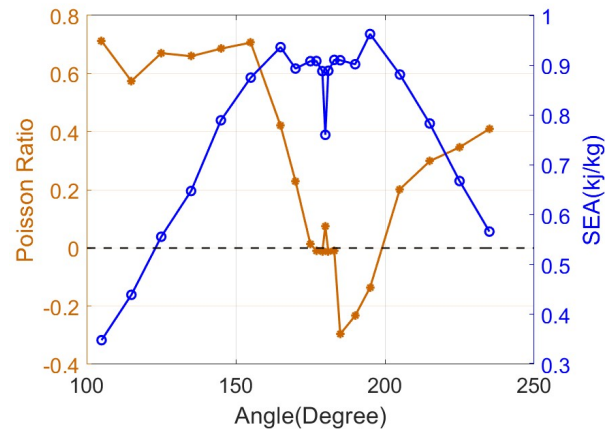


Figure 4.13: Variation of Poisson's ratio and SEA values with the angle change for the fifth parametric study of the chiral model

When all the results are considered, it seems that there is a relationship between the SEA value and the angle between the inclined edges and the compression direction. In the six angular change studies conducted in three different lattice geometries, it is observed that the energy absorption capacity increases as inclined edges are aligned with the compression direction. Another result that can be concluded from the angle change studies is that, although SEA is obtained by normalizing the energy absorption by the weight, the change in thickness, that is, the weight of the model, has an effect on the SEA. When the thickness is increased together with the angle to maintain the relative density, the SEA value also increases, and when the thickness is decreased together with the angle, the SEA value also decreases. If the SEA values are examined by increasing the thickness in the models, meaningful values may not be obtained after a certain thickness. Because with the excessive increase in thickness, the locking strain decreases, and the Plateau region and SEA decrease too much. For example, if the thickness is 3.0 mm instead of 0.3 mm in the hexagonal lattice model, the

theoretical locking strain becomes 0.03 according to Equation (3.2). In this case, there may be no gap between the locking and critical strains from which plateau stress and SEA were calculated.

Another significant output is the thickness of the edges perpendicular and parallel to the compression direction. Especially in models where vertical and horizontal edges are added, and the thickness of these edges is increased, the increase in SEA is visible. However, the increase only continues up to a certain thickness. Suppose the thickness of the vertical or close-to-vertical elements is too high. In that case, the horizontal or close-to-horizontal elements that provide the connection between the vertical and close-to-vertical elements become too thin, and the load cannot be carried properly. Suppose the thickness of the horizontal or close-to-horizontal elements is too much. In that case, the SEA value decreases due to very low thicknesses of the vertical or close-to-vertical elements already carrying the load. Here, an optimization study can be conducted between the thicknesses of the edges.

As mentioned in the introduction, some studies in the literature claim that the auxetic properties of structures and energy absorption are proportional. Since auxetic materials contract in the direction perpendicular to the main compression direction, it is expected that they can better resist external loads, and since the edges start to touch each other at small strain values, the friction energy, and therefore the SEA value, is expected to increase. In addition, since the relative density of the deformed structure increases as it is compressed, it is logical that it can carry more load because of its relative density. When looking at the studies where horizontal elements are added to the chiral model, a linear relationship can be established between the auxetic properties of the model and the SEA. Again, when looking at the angular studies of the chiral model, the largest values of SEA occur when the structure is auxetic. However, when all studies are considered, the load-carrying capabilities of the edges of the lattice seriously affect the SEA value. Increasing the thickness of the vertical edges or aligning inclined elements towards the compression direction directly increases the SEA value. When examining the energy absorption capabilities of lattice structures, this feature should be considered at least as much as the auxetic property. According to the results of most studies, SEA is not high in models that show very auxetic properties because the structure's stiffness is sacrificed to make it

auxetic. It is observed in most models that Poisson's ratios being zero or close to zero rather than being negative (auxetic) causes SEA to increase more.





## CHAPTER 5

### CONCLUSION

This thesis provides a comprehensive computational exploration of the energy absorption capacities of hexagonal, re-entrant, and chiral lattice structures. By systematically varying geometric parameters such as thickness, angle, and additional elements, this study has uncovered critical insights into the interplay between lattice geometry and mechanical performance, particularly emphasizing the role of Poisson's ratio.

Through five detailed parametric studies, the analyses revealed the relationships between geometric configurations and energy absorption properties. Specifically, it was observed that lattice structures with transitions in Poisson's ratio sign consistently demonstrated superior energy absorption capacities in most cases.

The computational approach employed in this research, utilizing finite element analysis in ABAQUS/Explicit, has proven to be a robust method for evaluating the mechanical performance of complex lattice geometries. The ability to simulate and analyze stress-strain responses, reaction forces, and deformation patterns provides a solid foundation for understanding and optimizing lattice structures without the immediate need for costly experimental setups.

The study also highlighted the sensitivity of specific energy absorption (SEA) and plateau stress to geometric modifications. For instance, increasing the thickness of specific struts or altering the angle of unit cells significantly influenced the stress-strain behavior, densification, and overall energy dissipation. The thickness of the edges parallel or close to parallel to the compression direction and vertical or close to vertical, as well as the angles of these edges to the compression vector, affect

the plateau stress, locking strain, Poisson's ratio, and SEA parameters. Although a significant relationship has been established between Poisson's ratio and SEA, there may be parameters other than Poisson's ratio that affect the SEA value. More comprehensive studies should be conducted to examine what affects the SEA value.

In the studies conducted in this thesis, the unit cell numbers forming the lattice structure were kept constant in parametric studies. Therefore, the aspect ratios of the structures changed in studies where the angle was changed. Since the models created have finite sizes, the side boundaries will affect the results at different rates in each angular model. To keep the results' effect rate constant, parametric studies can be conducted with a fixed aspect ratio. For this, the unit cell numbers should vary from model to model. Changing the aspect ratio also changes the strain rate. Analyses with constant strain rate values can also be compared.

While this thesis focuses on a particular low-velocity compression, the findings open avenues for further research into dynamic and multi-axial loading conditions. Future studies could explore multi-material lattice configurations, the impact of different speeds, and the integration of machine learning techniques for predictive modeling and optimization. Additionally, real-world validation of these computational results through experimental testing would strengthen the applicability of the insights gained.

In conclusion, this thesis bridges fundamental research and practical application by elucidating the mechanisms governing energy absorption in lattice structures. The findings advance the understanding of the relationship between geometry and mechanical behavior and provide a road map for designing advanced materials tailored for high-performance engineering applications. The work presented here contributes to the growing knowledge of lattice structure optimization. It underscores the transformative potential of these structures in fields ranging from aerospace to biomedical engineering.

## REFERENCES

- [1] S. Schröder, C. D. Grimm, L. Witte, A. Dimassi, and P. Buchholz, “Design, development and testing of 3d-printed conformal energy absorbing structures”, *Materials Today Communications*, vol. 35, p. 106 204, 2023.
- [2] H. Mohammadi, Z. Ahmad, M. Petru, *et al.*, “An insight from nature: honeycomb pattern in advanced structural design for impact energy absorption”, *Journal of Materials Research and Technology*, vol. 22, pp. 2862–2887, 2023.
- [3] N. Willems, G. Langenbach, V. Everts, and A. Zentner, “The microstructural and biomechanical development of the condylar bone: a review”, *The European Journal of Orthodontics*, vol. 36, pp. 479–485, 2013.
- [4] N. Khan and A. Riccio, “A systematic review of design for additive manufacturing of aerospace lattice structures: current trends and future directions”, *Progress in Aerospace Sciences*, vol. 149, p. 101 021, 2024.
- [5] X. Zhang, L. An, and H. Ding, “Dynamic crushing behavior and energy absorption of honeycombs with density gradient”, *Journal of Sandwich Structures and Materials*, vol. 16, no. 2, pp. 125–147, 2013.
- [6] J. Zhang, G. Lu, and Z. You, “Large deformation and energy absorption of additively manufactured auxetic materials and structures: a review”, *Composites Part B*, vol. 201, p. 108 340, 2020.
- [7] X. Ren, J. Shen, P. Tran, T. D. Ngo, and Y. M. Xie, “Auxetic nail: design and experimental study”, *Composite Structures*, vol. 184, pp. 288–298, 2018.
- [8] T. Li and L. Wang, “Bending behavior of sandwich composite structures with tunable 3d-printed core materials”, *Composite Structures*, vol. 175, pp. 46–57, 2017.

- [9] Y. Jiang, K. Shi, L. Zhou, *et al.*, “3d-printed auxetic-structured intervertebral disc implant for potential treatment of lumbar herniated disc”, *Bioactive Materials*, vol. 20, pp. 528–538, 2023.
- [10] G. Imbalzano, S. Linforth, T. D. Ngo, P. V. S. Lee, and P. Tran, “Blast resistance of auxetic and honeycomb sandwich panels: comparisons and parametric designs”, *Composite Structures*, vol. 183, pp. 242–261, 2018.
- [11] E. Etemadi, A. M. Zamani, F. Scarpa, M. Zeeshan, M. Hosseinabadi, and H. Hu, “Modified re-entrant auxetic metamaterials with energy absorption enhancement”, *Materials Today Communications*, vol. 38, p. 108 079, 2024.
- [12] H. Tan, Z. He, K. Li, E. Li, A. Cheng, and B. Xu, “In-plane crashworthiness of re-entrant hierarchical honeycombs with negative poisson’s ratio”, *Composite Structures*, vol. 229, p. 111 415, 2019.
- [13] K. P. Logakannan, V. Ramachandran, J. Rengaswamy, Z. Gao, and D. Ruan, “Quasi-static and dynamic compression behaviors of a novel auxetic structure”, *Composite Structures*, vol. 254, p. 112 853, 2020.
- [14] T. Tancogne-Dejean, A. B. Spierings, and D. Mohr, “Additively-manufactured metallic micro-lattice materials for high specific energy absorption under static and dynamic loading”, *Acta Materialia*, vol. 116, pp. 14–28, 2016.
- [15] C. Xiao, R. Tian, X. Zhang, and S. Li, “Variable stiffness and zero poisson’s ratio of the butterfly-shaped mechanical metamaterial”, *Composites Communications*, vol. 49, p. 101 958, 2024.
- [16] C. Xiao, R. Tian, X. Zhang, and S. Li, “Mechanical properties and band gap characteristics of flexible skin based on multi-concave angle honeycomb”, *Materials Today Communications*, vol. 35, p. 106 113, 2023.
- [17] A. Karabatak, “Latis malzemelerin enerji emme ve ezilme davranışlarının statik ve dinamik yüklemeler altında incelenmesi”, M.S. thesis, TOBB Ekonomi ve Teknoloji Üniveritesi, 2023.
- [18] D. Ruan, G. Lu, B. Wang, and T. Yu, “In-plane dynamic crushing of honeycombs—a finite element study”, *International Journal of Impact Engineering*, vol. 28, no. 2, pp. 161–182, 2003.

- [19] L. J. Gibson and M. F. Ashby., *Cellular solids: structure and properties*, 2nd ed. Cambridge ; New York: Cambridge University Press, 1999.
- [20] D. Zhang, Q. Fei, and P. Zhang, “In-plane dynamic crushing behavior and energy absorption of honeycombs with a novel type of multi-cells”, *Thin-Walled Structures*, vol. 117, pp. 199–210, 2017.
- [21] Y. Wang, P. Xue, and J. Wang, “Comparing study of energy-absorbing behavior for honeycomb structures”, *Key Engineering Materials*, vol. 462, pp. 13–17, 2011.
- [22] Y. Luo, F. Dai, J. Shen, A. Wang, X. Jiang, and Y. Li, “Negative poisson’s ratio lattice structure with chiral and re-entrant properties”, *Applied Sciences*, vol. 13, no. 24, p. 13 097, 2023.
- [23] X. Zhang, H. Hao, R. Tian, Q. Xue, H. Guan, and X. Yang, “Quasi-static compression and dynamic crushing behaviors of novel hybrid re-entrant auxetic metamaterials with enhanced energy-absorption”, *Composite Structures*, vol. 288, p. 115 399, 2022.
- [24] *Abaqus/standard user’s manual, version 6.14, dassault systèmes simulia corp, united states, 2014.*
- [25] Z. Chen, J. Li, B. Wu, X. Chen, and Y. M. Xie, “Enhanced mechanical properties of re-entrant auxetic honeycomb with self-similar inclusion”, *Composite Structures*, vol. 331, p. 117 921, 2024.



## Appendix A

### RESULTS OF ALL PARAMETRIC MODELS

As mentioned in Chapter 4, the results of all models created parametrically are not shared because, in some models, the Poisson ratio does not change the sign or does not approach zero. In addition, the Poisson ratios of the structures are shared only at 0.015 strain. This section shares the SEA results of all parametric studies and the Poisson's ratios at strain values of 0.004, 0.015, 0.05, 0.1. A table was given for each parametric study. The geometric parameters are shown in the first three columns of the tables, the SEA results are shown in the fourth column, and the Poisson ratios at strain values of 0.004, 0.015, and 0.1 are shown in the fifth, sixth, seventh, and eighth columns, respectively. Four graphs show how the Poisson ratio and SEA values change for each parametric model according to the thickness or angle change in the models. Each graph shows a different strain value. The Poisson ratio axis and line in the graphs are the same color as the corresponding column in the table, and the SEA axis and line are shown in blue. The results for all models are shown below, respectively.

## A.1 Hexagonal Lattice

Thickness of Sections (mm)			SEA (kj/kg)	Poisson's ratio	Poisson's ratio	Poisson's ratio	Poisson's ratio
Base	Horizontal	Inclined		at strain 0.004	at strain 0.015	at strain 0.05	at strain 0.1
0.3	0.35	0.2758	0.74	1.36	1.03	0.77	0.49
0.3	0.3	0.3	0.89	1.30	1.02	0.74	0.48
0.3	0.25	0.3242	1.11	1.24	1.02	0.75	0.48
0.3	0.2	0.3484	1.20	1.16	1.01	0.69	0.39
0.3	0.15	0.3726	1.28	1.10	0.98	0.58	0.31
0.3	0.125	0.4588	1.33	1.07	0.96	0.52	0.28
0.3	0.1	0.3968	1.18	1.03	0.77	0.08	0.06
0.3	0.075	0.4830	1.06	0.97	0.31	-0.07	-0.03
0.3	0.05	0.4951	0.83	0.90	0.14	0.03	-0.08
0.3	0.025	0.5072	0.84	0.59	-0.18	-0.55	-1.43
0.3	0.01	0.4403	0.72	0.27	-0.38	-1.05	-1.97
0.3	0.0075	0.5157	0.67	0.21	-0.35	-1.07	-2.04
0.3	0.005	0.4427	0.47	0.17	-0.24	-0.92	-1.70
0.3	0.001	0.4464	0.39	0.08	-0.15	-0.47	-0.80

Table A.1: Model parameters, SEA, and Poisson's ratio for 0.004, 0.015, 0.05, and 0.1 strains of the first parametric study of the hexagonal lattice

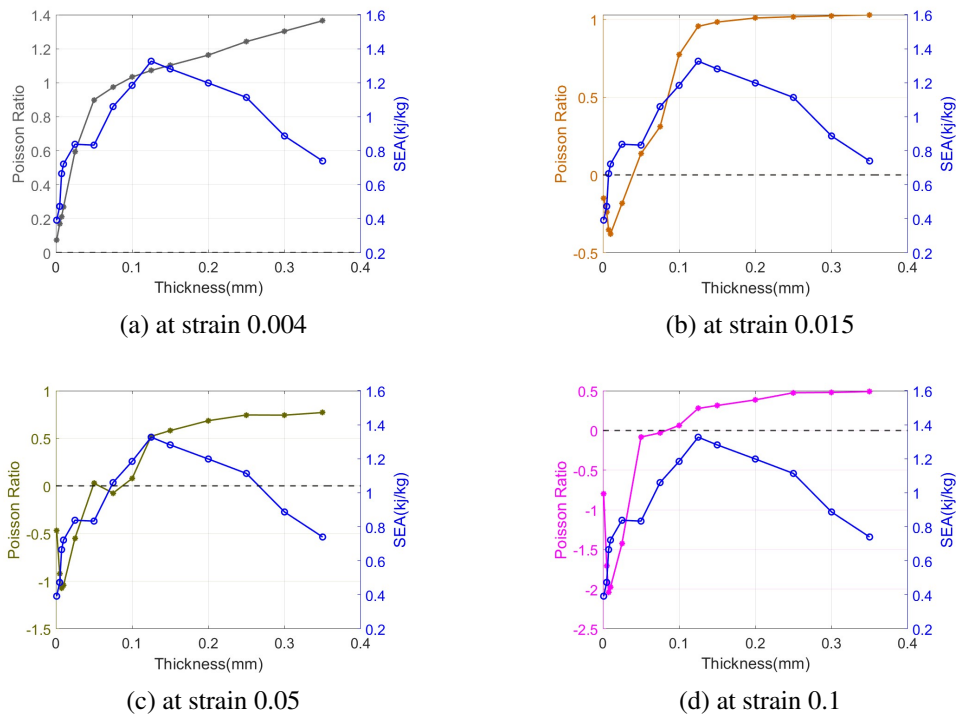


Figure A.1: Variation of Poisson's ratio and SEA values with the thickness change for the first parametric study of the hexagonal lattice



Thickness of Sections (mm)			SEA	Poisson's ratio	Poisson's ratio	Poisson's ratio	Poisson's ratio
Base	Hexagonal	Additional	(kj/kg)	at strain 0.004	at strain 0.015	at strain 0.05	at strain 0.1
0.3	0.300	0	0.89	1.30	1.02	0.74	0.48
0.3	0.299	0.001	0.96	1.25	1.02	0.73	0.47
0.3	0.297	0.005	0.96	1.11	1.02	0.74	0.47
0.3	0.293	0.01	1.12	1.00	1.01	0.74	0.45
0.3	0.267	0.05	2.06	0.86	0.86	0.45	0.20
0.3	0.251	0.075	2.07	0.63	0.30	0.04	-0.05
0.3	0.234	0.1	1.88	-0.02	-0.17	-0.12	-0.14
0.3	0.226	0.1125	1.85	-0.09	-0.18	-0.18	-0.19
0.3	0.218	0.125	1.62	-0.07	-0.13	-0.14	-0.15
0.3	0.210	0.1375	1.62	-0.11	-0.11	-0.14	-0.17
0.3	0.202	0.15	1.51	-0.05	-0.01	-0.06	-0.08
0.3	0.185	0.175	1.38	0.22	-0.18	-0.35	-0.28
0.3	0.169	0.2	1.30	0.36	-0.26	-0.49	-0.39
0.3	0.136	0.25	1.02	0.14	-0.12	-0.10	-0.11
0.3	0.103	0.3	0.73	0.04	-0.13	-0.11	-0.13
0.3	0.037	0.4	0.13	-0.08	-0.15	-0.16	-0.14

Table A.2: Model parameters, SEA, and Poisson's ratio for 0.004, 0.015, 0.05, and 0.1 strains of the second parametric study of the hexagonal lattice

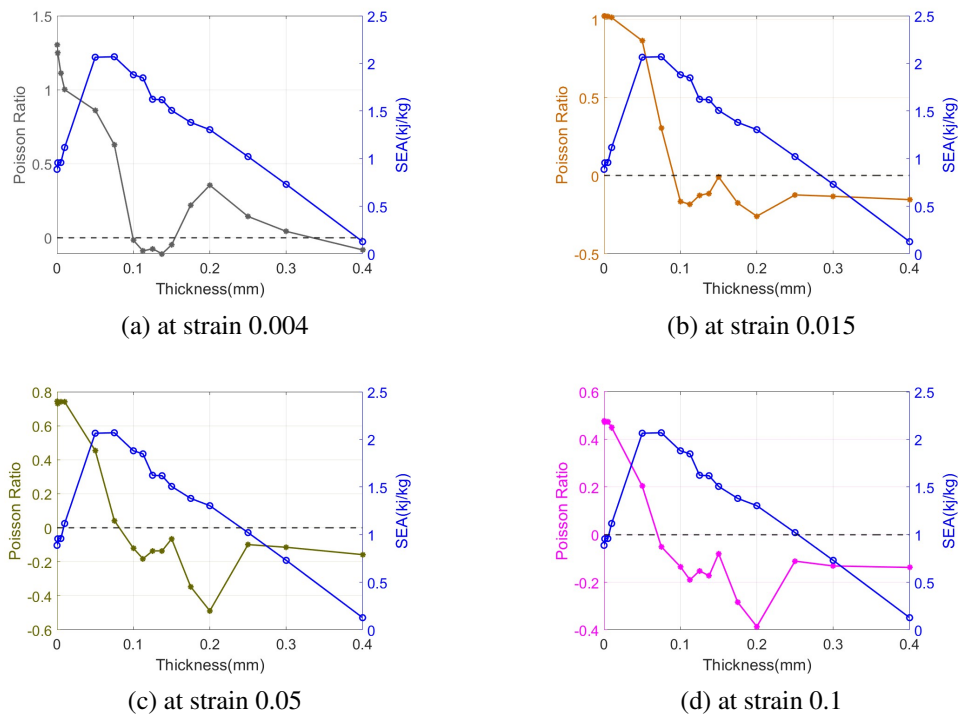


Figure A.2: Variation of Poisson's ratio and SEA values with the thickness change for the second parametric study of the hexagonal lattice

Thickness of Sections (mm)			SEA	Poisson's ratio	Poisson's ratio	Poisson's ratio	Poisson's ratio
Base	Hexagonal	Additional	(kj/kg)	at strain 0.004	at strain 0.015	at strain 0.05	at strain 0.1
0.3	0.300	0	0.89	1.30	1.02	0.74	0.48
0.3	0.299	0.001	0.90	1.30	1.02	0.74	0.48
0.3	0.297	0.005	0.87	1.29	1.02	0.74	0.48
0.3	0.294	0.01	0.85	1.28	1.02	0.74	0.48
0.3	0.272	0.05	0.84	1.09	1.03	0.79	0.51
0.3	0.243	0.1	0.95	1.13	0.97	0.73	0.49
0.3	0.215	0.15	1.26	1.00	0.65	0.33	0.21
0.3	0.186	0.2	1.45	0.91	0.48	0.18	0.15
0.3	0.158	0.25	1.64	0.94	0.36	0.09	0.09
0.3	0.129	0.3	1.66	0.86	0.36	0.00	-0.04
0.3	0.073	0.4	1.14	0.93	-0.13	-1.38	-2.12
0.3	0.044	0.45	0.91	0.97	-1.33	-2.77	-3.35
0.3	0.030	0.475	0.75	0.63	-1.35	-3.16	-3.66
0.3	0.016	0.5	0.56	0.35	-1.41	-3.42	-4.25
0.3	0.002	0.525	0.30	0.09	-0.59	-1.16	-1.79
0.3	0.001	0.526	0.30	0.09	-0.63	-1.07	-1.44

Table A.3: Model parameters, SEA, and Poisson's ratio for 0.004, 0.015, 0.05, and 0.1 strains of the third parametric study of the hexagonal lattice

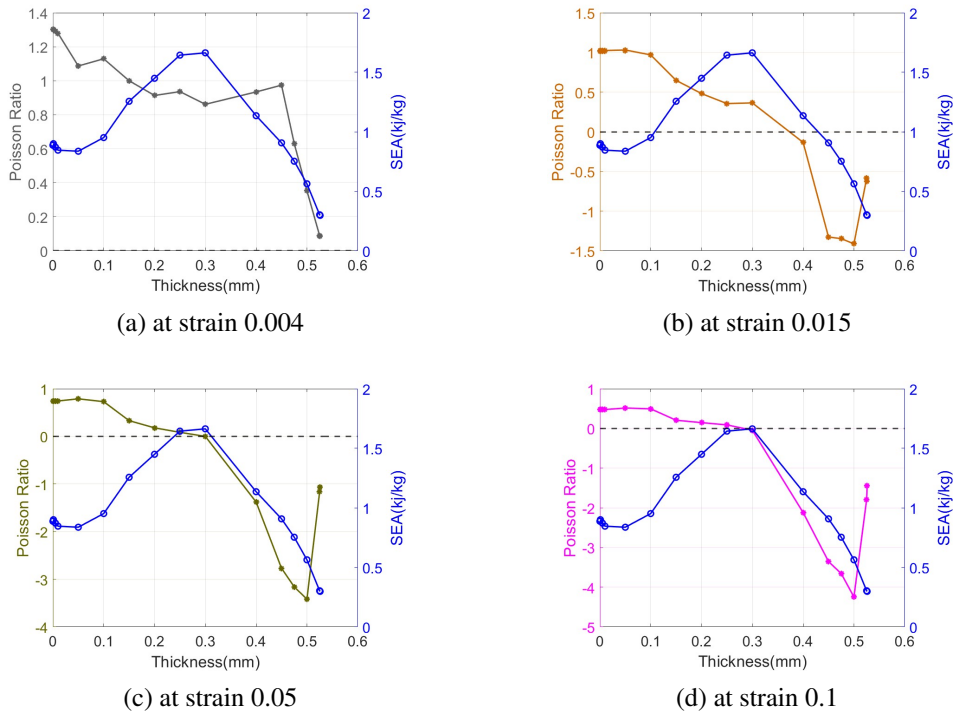


Figure A.3: Variation of Poisson's ratio and SEA values with the thickness change for the third parametric study of the hexagonal lattice

Angle (Degree)	Thickness (mm)	Relative Density	SEA (kJ/kg)	Poisson's ratio at strain 0.004	Poisson's ratio at strain 0.015	Poisson's ratio at strain 0.05	Poisson's ratio at strain 0.1
120	0.300	0.0693	0.89	1.30	1.02	0.74	0.48
115	0.300	0.0698	1.04	1.75	1.35	0.95	0.59
110	0.300	0.0714	1.17	2.36	1.81	1.23	0.75
105	0.300	0.0740	1.17	3.26	2.44	1.66	1.08
100	0.300	0.0779	1.43	5.22	3.23	1.81	1.01
97.5	0.300	0.0803	1.37	6.75	3.74	1.96	1.09
95	0.300	0.0831	1.41	7.86	4.35	2.11	1.24
93	0.300	0.0856	1.40	6.63	4.56	2.16	1.23
91	0.300	0.0885	1.50	2.60	1.00	0.40	0.19
90	0.300	0.0900	1.43	-0.18	0.25	0.28	0.28
89	0.300	0.0916	1.47	-2.78	-1.35	-0.71	-0.32
87	0.300	0.0951	1.40	-7.54	-4.66	-2.35	-1.64
85	0.300	0.0990	1.47	-9.64	-5.08	-2.72	-2.21
82.5	0.300	0.1044	1.25	-9.07	-4.64	-2.93	-2.31
80	0.300	0.1106	0.87	-7.72	-4.55	-3.06	-2.32
75	0.300	0.1257	1.18	-5.91	-4.23	-3.31	-2.51
70	0.300	0.1456	0.99	-5.24	-3.95	-3.45	-2.01

Table A.4: Model parameters, SEA, and Poisson's ratio for 0.004, 0.015, 0.05, and 0.1 strains of the fourth parametric study of the hexagonal lattice

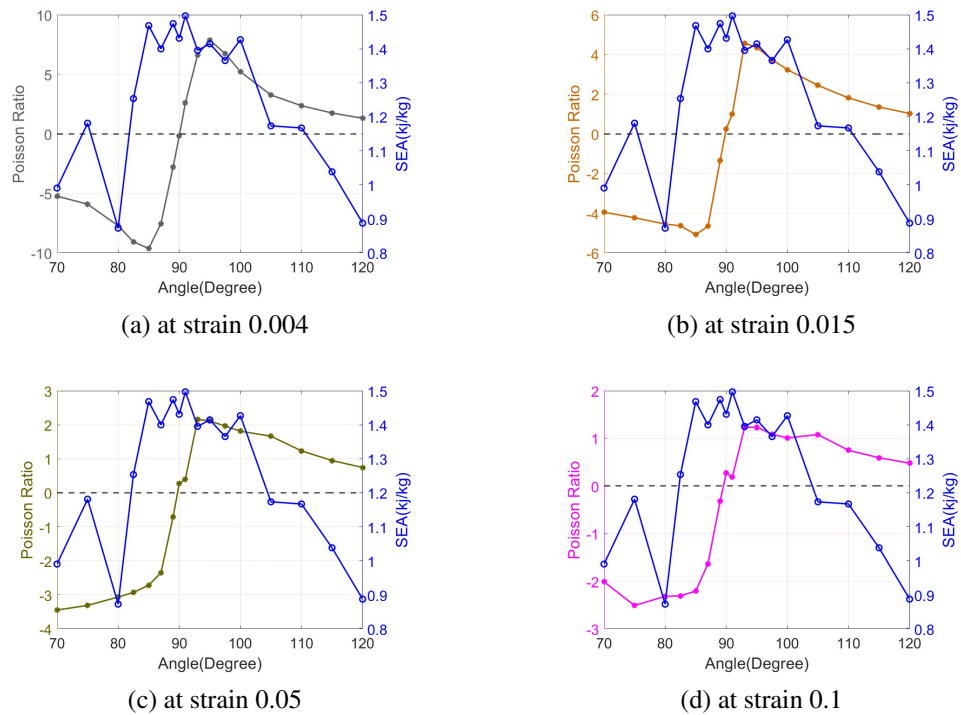


Figure A.4: Variation of Poisson's ratio and SEA values with the thickness change for the fourth parametric study of the hexagonal lattice

Angle (Degree)	Thickness (mm)	Relative Density	SEA (kJ/kg)	Poisson's ratio at strain 0.004	Poisson's ratio at strain 0.015	Poisson's ratio at strain 0.05	Poisson's ratio at strain 0.1
120	0.300	0.0693	0.89	1.30	1.02	0.74	0.48
115	0.298	0.0693	1.05	1.73	1.35	0.96	0.60
110	0.291	0.0693	1.16	2.28	1.81	1.27	0.79
105	0.281	0.0693	1.11	3.14	2.42	1.70	1.18
100	0.267	0.0693	1.24	4.86	3.19	1.98	1.15
97.5	0.259	0.0693	1.24	6.43	3.75	2.19	1.26
95	0.250	0.0693	1.28	6.80	4.50	2.37	1.38
93	0.243	0.0693	1.17	6.02	4.86	2.45	1.64
91	0.235	0.0693	1.21	2.18	1.41	0.65	0.27
90	0.231	0.0693	1.32	0.07	0.38	0.19	0.13
89	0.227	0.0693	1.22	-2.19	-0.76	-0.44	-0.16
87	0.219	0.0693	1.08	-6.55	-5.20	-3.09	-2.13
85	0.210	0.0693	1.13	-7.08	-5.51	-3.21	-2.43
82.5	0.199	0.0693	0.90	-8.20	-4.89	-3.00	-2.34
80	0.188	0.0693	0.81	-6.17	-4.69	-3.03	-2.31
75	0.165	0.0693	0.70	-5.10	-4.29	-3.17	-2.50
70	0.143	0.0693	0.41	-4.15	-3.96	-3.24	-2.10

Table A.5: Model parameters, SEA, and Poisson's ratio for 0.004, 0.015, 0.05, and 0.1 strains of the fifth parametric study of the hexagonal lattice

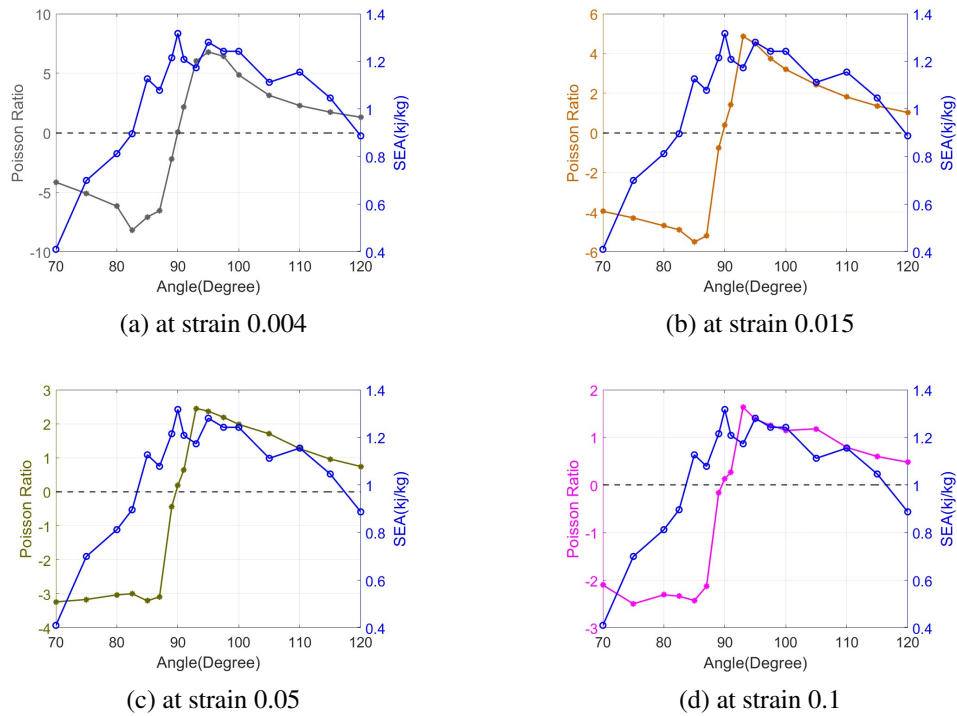


Figure A.5: Variation of Poisson's ratio and SEA values with the thickness change for the fifth parametric study of the hexagonal lattice

## A.2 Re-entrant Lattice

Thickness of Sections (mm)			SEA (kj/kg)	Poisson's ratio at strain 0.004	Poisson's ratio at strain 0.015	Poisson's ratio at strain 0.05	Poisson's ratio at strain 0.1
Base	Horizontal	Inclined					
0.225	0.4	0.056	0.10	-0.85	-1.07	-0.93	-0.80
0.225	0.35	0.104	0.19	-1.29	-1.21	-0.97	-0.80
0.225	0.3	0.152	0.26	-1.27	-1.03	-0.93	-0.73
0.225	0.25	0.201	0.45	-1.22	-1.02	-0.85	-0.63
0.225	0.225	0.225	0.56	-1.19	-1.02	-0.80	-0.63
0.225	0.2	0.249	0.76	-1.15	-1.02	-0.79	-0.62
0.225	0.15	0.298	0.70	-1.06	-0.99	-0.67	-0.53
0.225	0.1	0.346	0.60	-0.98	-0.94	-0.71	-0.59
0.225	0.05	0.394	0.77	-0.97	-1.22	-1.68	-1.41
0.225	0.01	0.433	0.71	-0.52	-1.45	-1.98	-3.31
0.225	0.001	0.442	0.31	-0.27	-0.81	-0.96	-1.07

Table A.6: Model parameters, SEA, and Poisson's ratio for 0.004, 0.015, 0.05, and 0.1 strains of the first parametric study of the re-entrant lattice

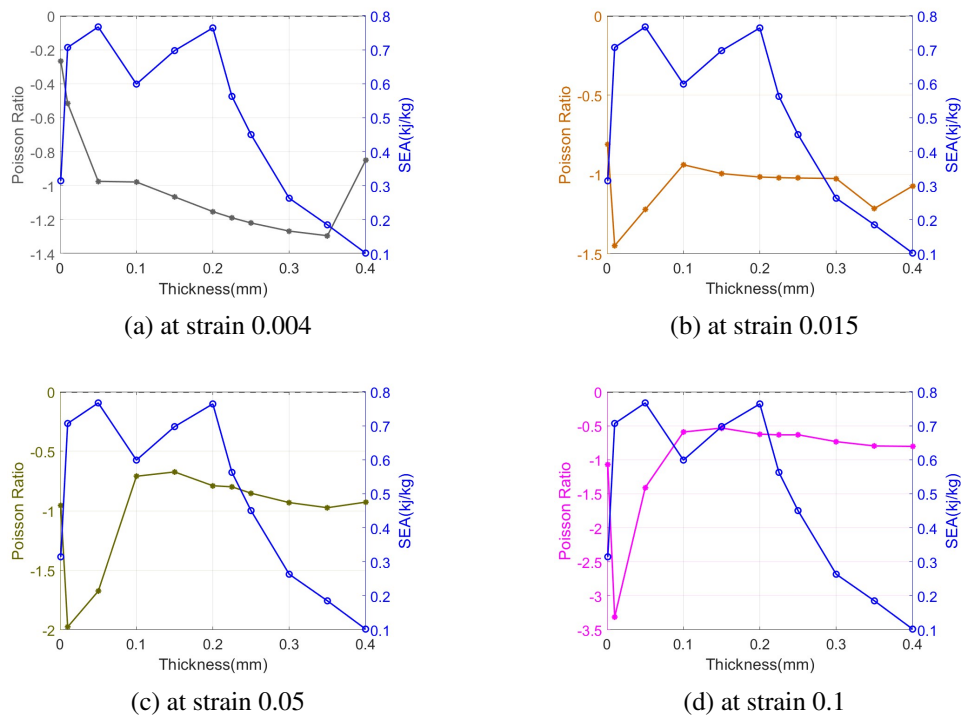


Figure A.6: Variation of Poisson's ratio and SEA values with the thickness change for the first parametric study of the re-entrant lattice

Thickness of Sections (mm)			SEA (kj/kg)	Poisson's ratio	Poisson's ratio	Poisson's ratio	Poisson's ratio
Base	Re-entrant	Additional		at strain 0.004	at strain 0.015	at strain 0.05	at strain 0.1
0.225	0.225	0	0.56	-1.19	-1.02	-0.80	-0.63
0.225	0.225	0.001	0.55	-1.19	-1.02	-0.81	-0.64
0.225	0.224	0.005	0.57	-1.20	-1.02	-0.82	-0.64
0.225	0.223	0.01	0.61	-1.22	-1.02	-0.84	-0.65
0.225	0.200	0.1	1.03	-0.50	-0.76	-0.49	-0.48
0.225	0.194	0.125	1.31	-0.08	-0.43	-0.37	-0.32
0.225	0.188	0.15	1.32	-0.02	-0.24	-0.20	-0.17
0.225	0.182	0.175	1.38	0.02	-0.15	-0.13	-0.15
0.225	0.175	0.2	1.28	0.03	-0.18	-0.14	-0.16
0.225	0.163	0.25	1.13	0.04	-0.20	-0.16	-0.16
0.225	0.151	0.3	1.27	0.03	-0.18	-0.16	-0.16
0.225	0.126	0.4	0.86	0.03	-0.07	-0.11	-0.10
0.225	0.101	0.5	0.62	0.01	-0.04	-0.12	-0.14
0.225	0.076	0.6	0.36	-0.06	-0.06	-0.12	-0.18
0.225	0.052	0.7	0.12	-0.02	-0.01	-0.10	-0.08
0.225	0.027	0.8	0.03	-0.06	-0.02	-0.07	-0.07

Table A.7: Model parameters, SEA, and Poisson's ratio for 0.004, 0.015, 0.05, and 0.1 strains of the second parametric study of the re-entrant lattice

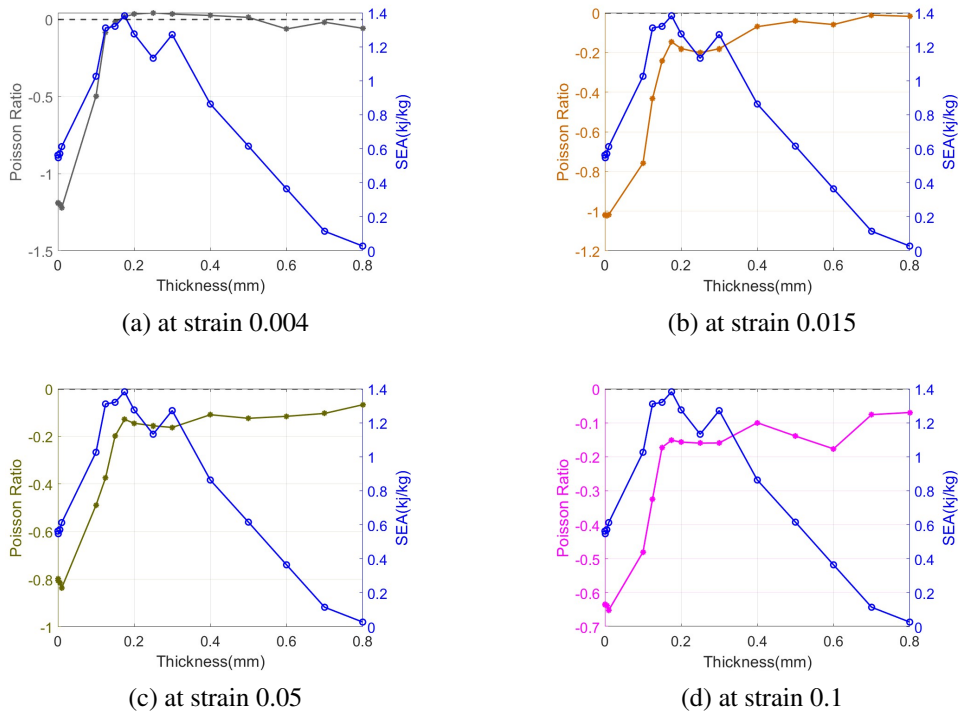


Figure A.7: Variation of Poisson's ratio and SEA values with the thickness change for the second parametric study of the re-entrant lattice

Thickness of Sections (mm)			SEA (kj/kg)	Poisson's ratio	Poisson's ratio	Poisson's ratio	Poisson's ratio
Base	Re-entrant	Additional		at strain 0.004	at strain 0.015	at strain 0.05	at strain 0.1
0.225	0.225	0	0.56	-1.19	-1.02	-0.80	-0.63
0.225	0.225	0.001	0.56	-1.17	-1.02	-0.79	-0.64
0.225	0.223	0.005	0.54	-1.13	-1.02	-0.78	-0.59
0.225	0.221	0.01	0.54	-1.11	-1.02	-0.81	-0.63
0.225	0.204	0.05	0.62	-1.04	-1.03	-0.89	-0.71
0.225	0.182	0.1	0.87	-1.04	-0.98	-0.65	-0.46
0.225	0.161	0.15	0.89	-1.16	-0.99	-0.60	-0.18
0.225	0.139	0.2	0.82	-1.24	-1.02	-0.76	-0.37
0.225	0.118	0.25	0.87	-1.27	-1.17	-1.40	-1.00
0.225	0.096	0.3	0.58	-1.33	-0.82	-0.85	-0.84
0.225	0.054	0.4	0.85	-1.05	-1.25	-0.69	-0.84

Table A.8: Model parameters, SEA, and Poisson's ratio for 0.004, 0.015, 0.05, and 0.1 strains of the third parametric study of the re-entrant lattice

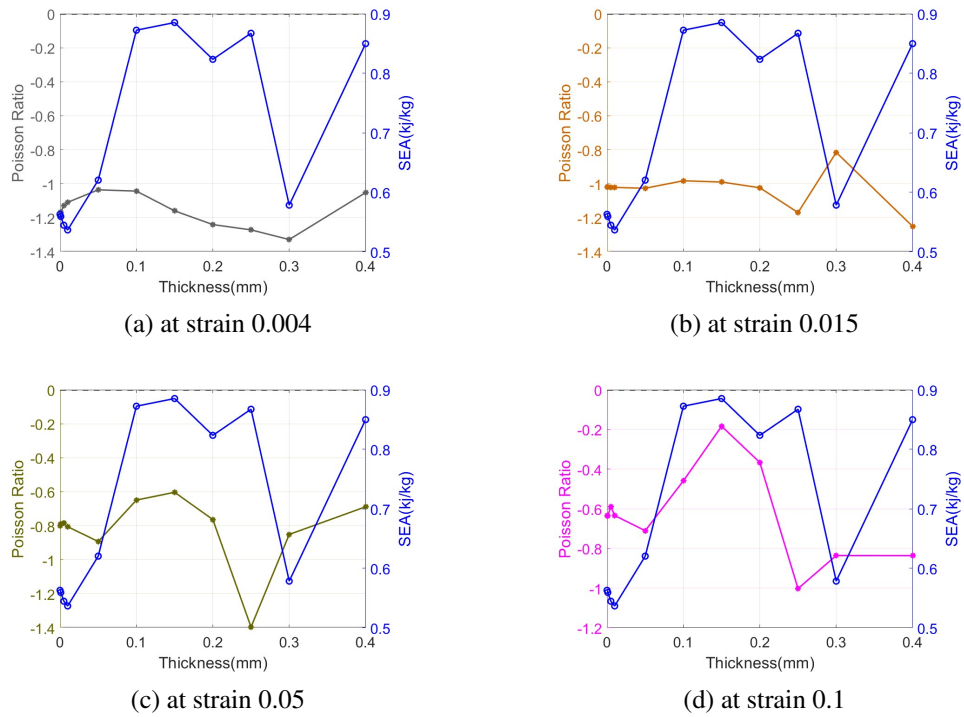


Figure A.8: Variation of Poisson's ratio and SEA values with the thickness change for the third parametric study of the re-entrant lattice

Angle (Degree)	Thickness (mm)	Relative Density	SEA (kJ/kg)	Poisson's ratio at strain 0.004	Poisson's ratio at strain 0.015	Poisson's ratio at strain 0.05	Poisson's ratio at strain 0.1
60	0.225	0.0693	0.56	-1.19	-1.02	-0.80	-0.63
65	0.225	0.0630	0.63	-1.53	-1.22	-0.90	-0.72
70	0.225	0.0578	0.84	-1.89	-1.47	-1.08	-0.78
75	0.225	0.0535	0.77	-2.25	-1.73	-1.10	-0.84
80	0.225	0.0500	0.80	-2.97	-2.06	-1.12	-0.84
82.5	0.225	0.0486	0.78	-4.33	-2.33	-1.20	-0.87
85	0.225	0.0472	0.85	-2.91	-2.69	-1.60	-1.08
87	0.225	0.0463	0.81	-2.10	-1.80	-0.82	-0.47
89	0.225	0.0454	0.83	-0.72	0.02	-0.01	-0.07
90	0.225	0.0450	0.90	0.02	-0.03	-0.16	-0.25
91	0.225	0.0446	0.92	0.86	0.47	0.21	0.14
93	0.225	0.0439	0.88	2.10	1.73	0.77	0.44
95	0.225	0.0433	0.92	2.53	2.30	1.16	0.73
97.5	0.225	0.0426	0.84	3.75	2.06	1.03	0.62
100	0.225	0.0420	0.83	2.43	1.69	0.91	0.54
105	0.225	0.0412	0.76	1.57	1.29	0.81	0.46
110	0.225	0.0409	0.69	1.20	0.99	0.73	0.50
115	0.225	0.0410	0.65	0.87	0.76	0.57	0.37
120	0.225	0.0416	0.62	0.60	0.58	0.46	0.29

Table A.9: Model parameters, SEA, and Poisson's ratio for 0.004, 0.015, 0.05, and 0.1 strains of the fourth parametric study of the re-entrant lattice

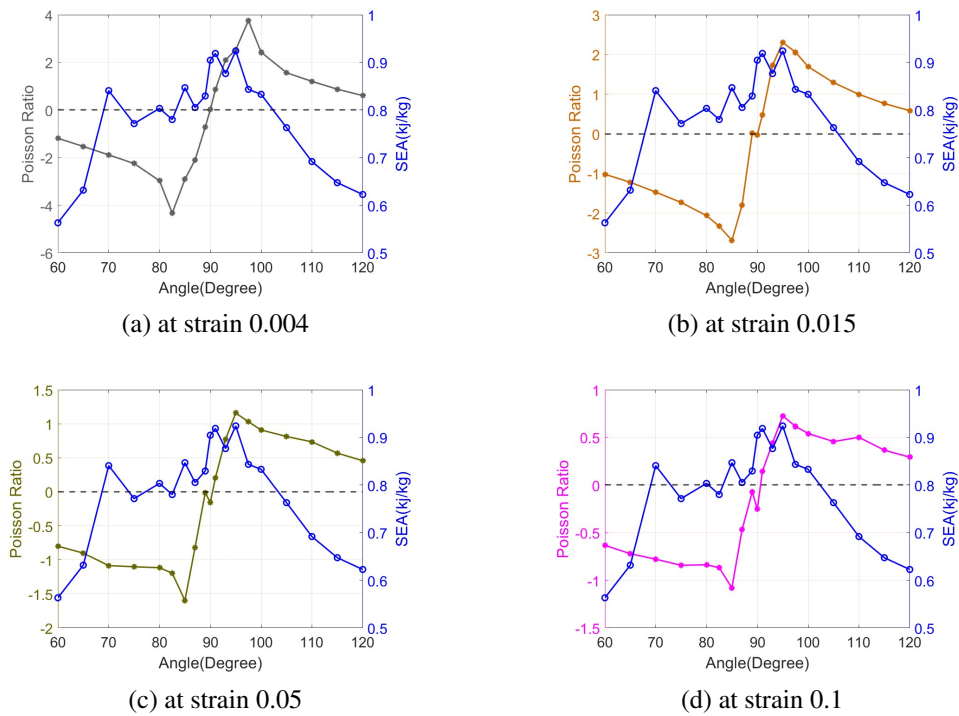


Figure A.9: Variation of Poisson's ratio and SEA values with the thickness change for the fourth parametric study of the re-entrant lattice



Angle (Degree)	Thickness (mm)	Relative Density	SEA (kJ/kg)	Poisson's ratio at strain 0.004	Poisson's ratio at strain 0.015	Poisson's ratio at strain 0.05	Poisson's ratio at strain 0.1
60	0.225000	0.0693	0.56	-1.19	-1.02	-0.80	-0.63
65	0.247613	0.0693	0.68	-1.60	-1.23	-0.89	-0.70
70	0.269852	0.0693	0.93	-1.97	-1.47	-1.05	-0.76
75	0.291305	0.0693	0.92	-2.61	-1.72	-0.98	-0.78
80	0.311528	0.0693	1.06	-3.59	-2.02	-1.07	-0.81
82.5	0.321032	0.0693	1.07	-3.91	-2.23	-1.14	-0.85
85	0.330054	0.0693	1.21	-3.89	-2.55	-1.29	-0.89
87	0.336883	0.0693	1.13	-2.57	-2.50	-1.36	-1.02
89	0.343335	0.0693	1.08	-0.74	-0.57	-0.25	-0.23
90	0.346410	0.0693	1.33	0.05	0.28	0.05	-0.05
91	0.349380	0.0693	1.35	0.76	0.57	0.08	-0.12
93	0.354988	0.0693	1.31	2.41	2.36	1.18	0.76
95	0.360130	0.0693	1.39	3.44	2.25	1.14	0.66
97.5	0.365861	0.0693	1.30	3.25	1.90	0.98	0.58
100	0.370767	0.0693	1.25	2.74	1.67	0.90	0.52
105	0.377908	0.0693	1.17	1.72	1.30	0.79	0.42
110	0.381186	0.0693	1.10	1.16	1.00	0.71	0.44
115	0.380296	0.0693	1.02	0.85	0.77	0.58	0.37
120	0.375000	0.0693	0.91	0.69	0.60	0.46	0.31

Table A.10: Model parameters, SEA, and Poisson's ratio for 0.004, 0.015, 0.05, and 0.1 strains of the fifth parametric study of the re-entrant lattice

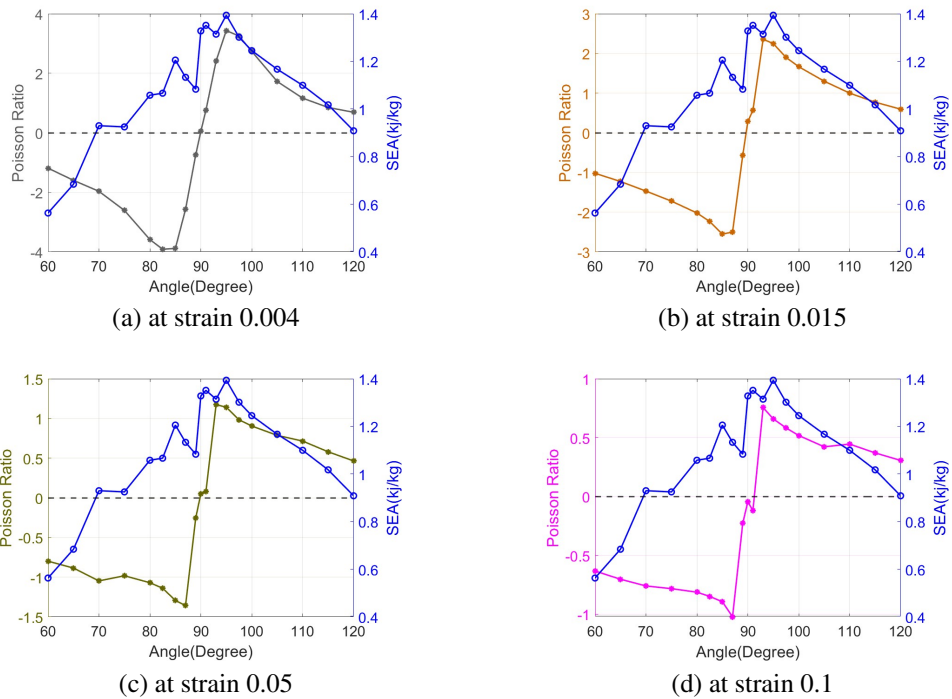


Figure A.10: Variation of Poisson's ratio and SEA values with the thickness change for the fifth parametric study of the re-entrant lattice

### A.3 Chiral Lattice

Thickness of Sections (mm)			SEA (kj/kg)	Poisson's ratio at strain 0.004	Poisson's ratio at strain 0.015	Poisson's ratio at strain 0.05	Poisson's ratio at strain 0.1
Base	Horizontal	Inclined					
0.15	0.275	0.025	0.44	0.11	0.12	0.12	0.10
0.15	0.25	0.050	0.47	0.16	0.18	0.08	0.10
0.15	0.225	0.075	0.51	0.24	0.23	0.12	0.11
0.15	0.2	0.100	0.65	0.36	0.35	0.17	0.13
0.15	0.175	0.125	0.71	0.49	0.57	0.34	0.23
0.15	0.15	0.150	0.74	0.55	0.66	0.41	0.32
0.15	0.125	0.175	0.67	0.51	0.70	0.28	0.26
0.15	0.1	0.200	0.69	0.40	0.58	0.22	0.22
0.15	0.075	0.225	0.51	0.27	0.16	0.25	0.12
0.15	0.05	0.250	0.48	0.19	0.32	0.13	-0.08
0.15	0.025	0.275	0.30	0.12	0.10	0.08	-0.69

Table A.11: Model parameters, SEA, and Poisson's ratio for 0.004, 0.015, 0.05, and 0.1 strains of the first parametric study of the chiral lattice

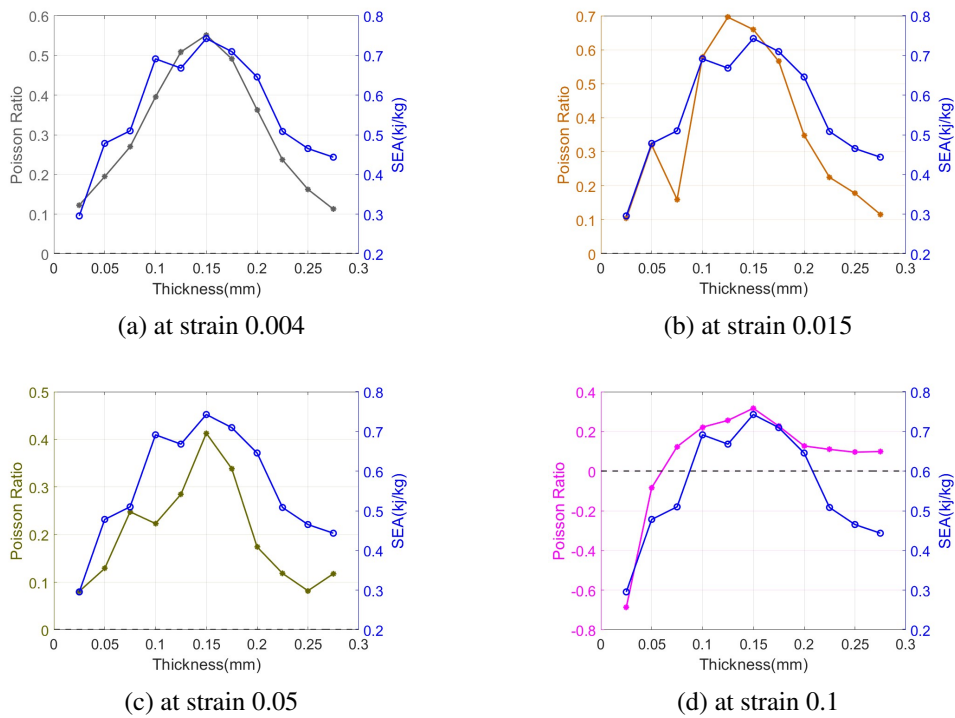


Figure A.11: Variation of Poisson's ratio and SEA values with the thickness change for the first parametric study of the chiral lattice

Thickness of Sections (mm)			SEA (kj/kg)	Poisson's ratio	Poisson's ratio	Poisson's ratio	Poisson's ratio
Base	Chiral	Additional		at strain 0.004	at strain 0.015	at strain 0.05	at strain 0.1
0.15	0.150	0	0.74	0.55	0.66	0.41	0.32
0.15	0.150	0.001	0.68	0.51	0.64	0.32	0.26
0.15	0.148	0.005	0.81	0.23	0.41	0.27	0.17
0.15	0.148	0.0075	0.86	0.04	0.19	0.19	0.14
0.15	0.147	0.01	0.98	-0.15	0.09	0.11	0.09
0.15	0.144	0.02	0.97	-0.45	0.00	-0.03	-0.04
0.15	0.141	0.03	0.91	-0.51	0.03	-0.07	-0.07
0.15	0.137	0.04	0.89	-0.56	0.03	-0.10	-0.09
0.15	0.134	0.05	0.78	-0.60	0.02	-0.10	-0.09
0.15	0.127	0.075	0.71	-0.67	-0.04	-0.10	-0.07
0.15	0.119	0.1	0.80	-0.73	-0.16	-0.12	-0.08
0.15	0.103	0.15	0.85	-0.79	-0.32	-0.17	-0.19
0.15	0.087	0.2	0.77	-0.79	-0.11	-0.27	-0.31
0.15	0.072	0.25	0.66	-0.64	-0.47	-0.33	-0.29

Table A.12: Model parameters, SEA, and Poisson's ratio for 0.004, 0.015, 0.05, and 0.1 strains of the second parametric study of the chiral lattice

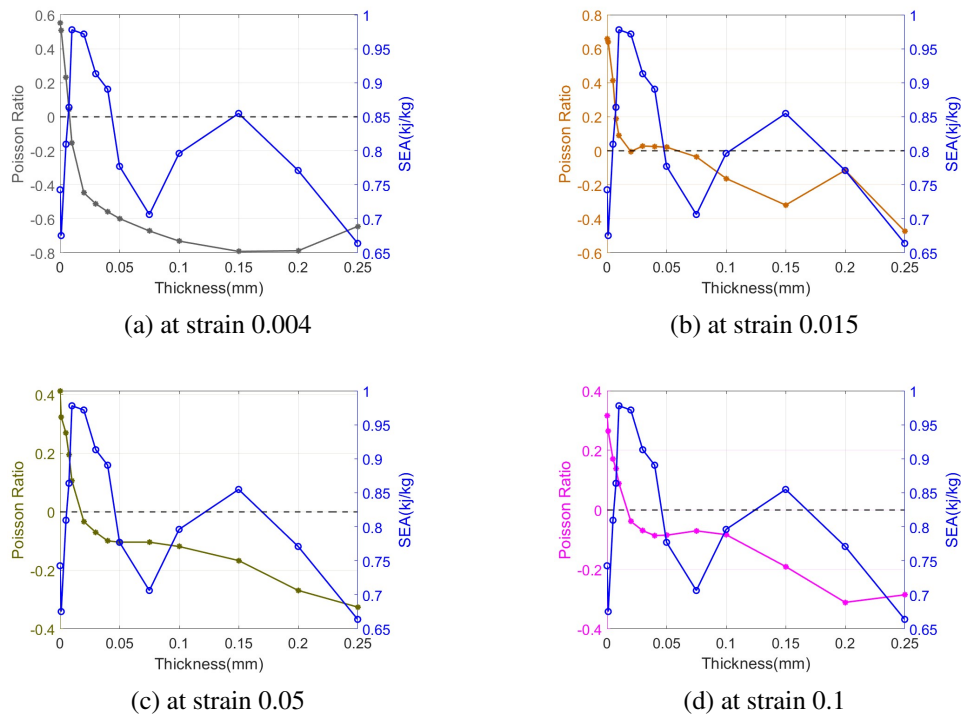


Figure A.12: Variation of Poisson's ratio and SEA values with the thickness change for the second parametric study of the chiral lattice

Thickness of Sections (mm)			SEA (kj/kg)	Poisson's ratio	Poisson's ratio	Poisson's ratio	Poisson's ratio
Base	Chiral	Additional		at strain 0.004	at strain 0.015	at strain 0.05	at strain 0.1
0.15	0.150	0	0.74	0.55	0.66	0.41	0.32
0.15	0.150	0.001	0.75	0.49	0.66	0.39	0.30
0.15	0.148	0.005	0.65	0.27	0.68	0.40	0.29
0.15	0.147	0.01	0.66	0.13	0.69	0.40	0.28
0.15	0.142	0.025	0.65	-0.02	0.67	0.38	0.27
0.15	0.134	0.05	0.69	-0.16	0.03	0.11	0.11
0.15	0.130	0.0625	0.74	-0.18	-0.06	0.00	0.04
0.15	0.127	0.075	0.81	-0.18	-0.09	-0.04	0.00
0.15	0.123	0.0875	0.96	-0.18	-0.10	-0.17	-0.08
0.15	0.119	0.1	1.12	-0.18	-0.09	-0.19	-0.16
0.15	0.111	0.125	1.36	-0.19	-0.09	-0.21	-0.31
0.15	0.103	0.15	1.44	-0.19	-0.15	-0.21	-0.31
0.15	0.087	0.2	1.69	-0.21	-0.20	-0.25	-0.31
0.15	0.072	0.25	1.45	-0.18	-0.23	-0.25	-0.31

Table A.13: Model parameters, SEA, and Poisson's ratio for 0.004, 0.015, 0.05, and 0.1 strains of the third parametric study of the chiral lattice

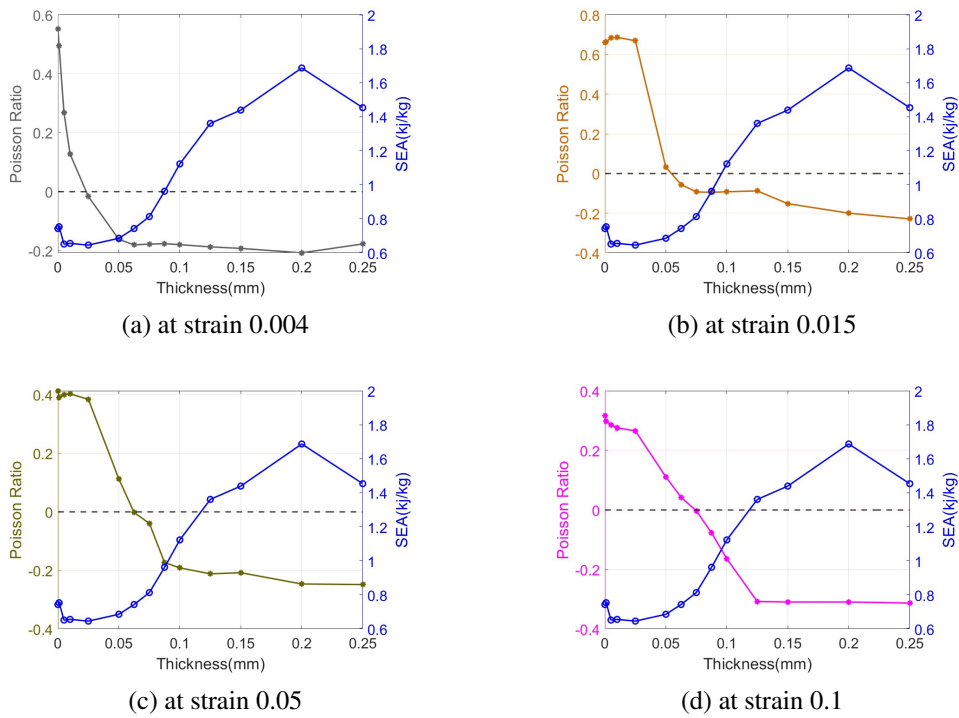


Figure A.13: Variation of Poisson's ratio and SEA values with the thickness change for the third parametric study of the chiral lattice

Angle (Degree)	Thickness (mm)	Relative Density	SEA (kJ/kg)	Poisson's ratio at strain 0.004	Poisson's ratio at strain 0.015	Poisson's ratio at strain 0.05	Poisson's ratio at strain 0.1
105	0.150	0.0953	0.47	0.17	0.59	0.55	0.56
115	0.150	0.0844	0.52	0.25	0.61	0.52	0.46
125	0.150	0.0763	0.59	0.36	0.67	0.42	0.38
135	0.150	0.0703	0.65	0.55	0.66	0.41	0.32
145	0.150	0.0660	0.74	0.77	0.69	0.42	0.12
155	0.150	0.0629	0.75	0.90	0.72	0.24	0.11
165	0.150	0.0610	0.82	0.81	0.47	0.11	0.03
170	0.150	0.0605	0.78	0.93	0.21	0.03	-0.01
175	0.150	0.0601	0.75	0.93	0.05	-0.02	-0.09
177	0.150	0.0600	0.78	0.75	-0.06	-0.06	-0.12
179	0.150	0.0600	0.78	0.78	-0.06	-0.05	-0.12
180	0.150	0.0600	0.71	0.09	-0.01	-0.13	-0.10
181	0.150	0.0600	0.78	0.77	-0.06	-0.05	-0.12
183	0.150	0.0600	0.78	0.74	-0.06	-0.06	-0.12
185	0.150	0.0601	0.74	-0.56	-0.35	-0.19	-0.17
190	0.150	0.0605	0.72	-0.12	-0.24	-0.13	-0.08
195	0.150	0.0610	0.89	0.01	-0.12	-0.14	-0.12
205	0.150	0.0629	0.78	0.36	0.21	0.00	-0.03
215	0.150	0.0660	0.73	0.37	0.31	0.14	-0.06
225	0.150	0.0703	0.64	0.25	0.35	0.24	0.15
235	0.150	0.0763	0.60	0.13	0.41	0.26	0.23

Table A.14: Model parameters, SEA, and Poisson's ratio for 0.004, 0.015, 0.05, and 0.1 strains of the fourth parametric study of the chiral lattice

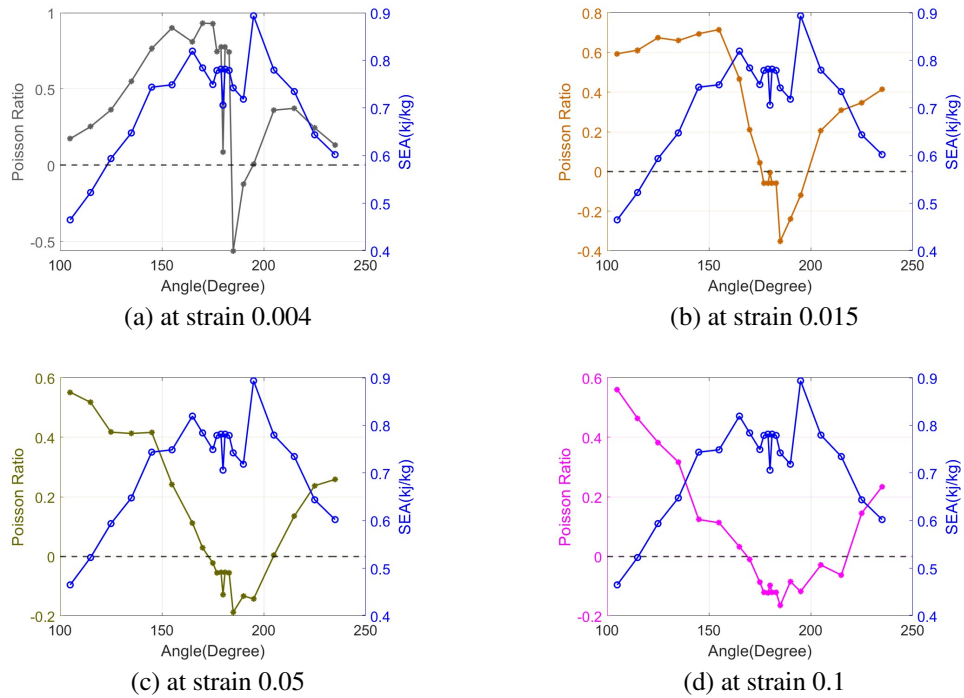


Figure A.14: Variation of Poisson's ratio and SEA values with the thickness change for the fourth parametric study of the chiral lattice

Angle (Degree)	Thickness (mm)	Relative Density	SEA (kJ/kg)	Poisson's ratio at strain 0.004	Poisson's ratio at strain 0.015	Poisson's ratio at strain 0.05	Poisson's ratio at strain 0.1
105	0.111	0.0703	0.35	0.13	0.71	0.57	0.13
115	0.125	0.0703	0.44	0.21	0.57	0.46	0.21
125	0.138	0.0703	0.56	0.33	0.67	0.40	0.33
135	0.150	0.0703	0.65	0.55	0.66	0.41	0.55
145	0.160	0.0703	0.79	0.78	0.69	0.41	0.78
155	0.168	0.0703	0.88	0.86	0.71	0.24	0.86
165	0.173	0.0703	0.94	0.81	0.42	0.09	0.81
170	0.174	0.0703	0.89	0.87	0.23	0.04	0.87
175	0.175	0.0703	0.91	0.88	0.01	-0.03	0.88
177	0.176	0.0703	0.91	0.69	-0.01	-0.04	0.69
179	0.176	0.0703	0.89	0.71	-0.01	-0.04	0.71
180	0.176	0.0703	0.76	0.16	0.07	0.02	0.16
181	0.176	0.0703	0.89	0.71	-0.01	-0.04	0.71
183	0.176	0.0703	0.91	0.68	-0.01	-0.04	0.68
185	0.175	0.0703	0.91	-0.49	-0.30	-0.13	-0.49
190	0.174	0.0703	0.90	-0.14	-0.23	-0.11	-0.14
195	0.173	0.0703	0.96	0.03	-0.14	-0.12	0.03
205	0.168	0.0703	0.88	0.33	0.20	-0.01	0.33
215	0.160	0.0703	0.78	0.40	0.30	0.13	0.40
225	0.150	0.0703	0.67	0.25	0.35	0.24	0.25
235	0.138	0.0703	0.57	0.11	0.41	0.24	0.11

Table A.15: Model parameters, SEA, and Poisson's ratio for 0.004, 0.015, 0.05, and 0.1 strains of the fifth parametric study of the chiral lattice

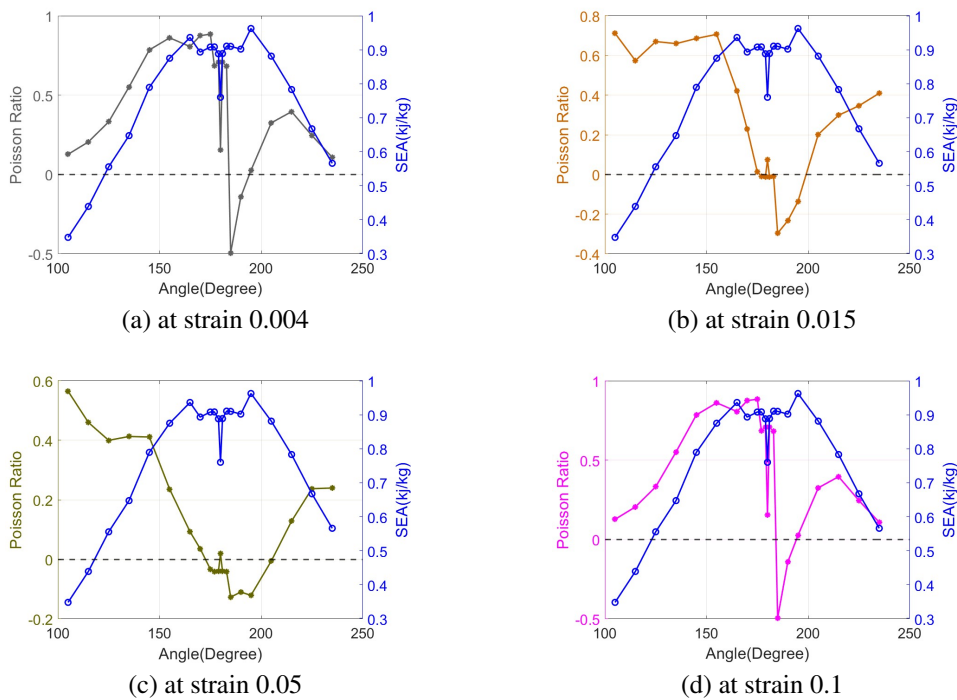


Figure A.15: Variation of Poisson's ratio and SEA values with the thickness change for the fifth parametric study of the chiral lattice

## Appendix B

### ENERGY CONSERVATION AND SEA CALCULATION

A comparison was made with two studies in the literature to check the accuracy of the analysis methods in the parametric studies in Chapter 2. In addition, the conservation of energy of the structures can be examined throughout the analysis. Especially in explicitly solved analyses, energy conservation should be checked throughout the analysis. Tables B.1, B.2, and B.3 give the energy results at different strain values during the compression analysis of the three base models in milijoules. The energy results are the values from Abaqus, and energy terms of a compressed structure are described in [24] as follows.

$$E_{TOTAL} = E_I + E_V + E_{KE} + E_{FD} - E_W \quad (B.1)$$

$$E_I = E_E + E_P + E_{CD} + E_A, \quad (B.2)$$

where  $E_W$  is external work,  $E_{FD}$  is frictional dissipated energy,  $E_{KE}$  is kinetic energy,  $E_V$  is viscous dissipated energy, and  $E_I$  is internal energy. Internal energy is given as the sum of four energies.  $E_E$  is elastic strain energy,  $E_P$  is plastic dissipated energy,  $E_A$  is artificial strain energy.  $E_{CD}$  is energy dissipated by viscoelasticity, but since the material model is elastic perfectly plastic, this energy was read as zero in all models.

$\epsilon$	$E_E$	$E_P$	$E_A$	$E_V$	$E_{FD}$	$E_{KE}$	$E_W$	$E_{TOTAL}$
$\epsilon_0$	0.0	0.0	0.0	0.0	0.0	1.6	0.0	1.6
$\epsilon_{0.004}$	7.1	1.6	0.1	0.3	0.6	7.0	15.1	1.6
$\epsilon_{0.015}$	19.0	39.1	0.8	1.0	2.0	6.6	67.1	1.6
$\epsilon_{0.05}$	12.8	167.9	0.9	1.1	2.0	9.0	192.2	1.6
$\epsilon_{0.1}$	14.7	317.9	1.1	1.2	2.4	6.0	341.8	1.6
$\epsilon_{0.2}$	15.6	647.2	1.6	3.0	2.9	6.7	673.4	1.6
$\epsilon_{0.5}$	22.8	1726.6	3.9	21.6	12.9	9.5	1771.5	1.6
$\epsilon_{0.75}$	24.5	2882.5	9.4	92.7	122.8	3.3	3029.7	1.7
$\epsilon_d$	27.3	3270.0	13.2	135.7	165.9	6.5	3465.0	1.7

Table B.1: Energy values in milijoules of the base hexagonal model at different strains

$\epsilon$	$E_E$	$E_P$	$E_A$	$E_V$	$E_{FD}$	$E_{KE}$	$E_W$	$E_{TOTAL}$
$\epsilon_0$	0.0	0.0	0.0	0.0	0.0	1.6	0.0	1.6
$\epsilon_{0.004}$	3.6	0.8	0.1	0.2	0.3	7.1	10.6	1.6
$\epsilon_{0.015}$	13.4	14.5	0.4	1.0	0.9	6.8	35.6	1.6
$\epsilon_{0.05}$	9.9	87.8	0.6	1.0	0.9	11.9	110.7	1.6
$\epsilon_{0.1}$	11.4	184.7	0.8	1.1	1.1	8.6	206.2	1.6
$\epsilon_{0.2}$	12.7	347.7	1.0	1.5	2.0	8.7	372.0	1.6
$\epsilon_{0.5}$	19.9	890.1	2.0	6.4	5.4	5.5	922.9	1.6
$\epsilon_{0.75}$	22.7	1629.5	5.0	37.7	30.3	4.8	1690.1	1.7
$\epsilon_d$	17.5	2052.8	10.0	102.0	123.1	3.8	2196.8	1.7

Table B.2: Energy values in milijoules of the base re-entrant model at different strains

$\epsilon$	$E_E$	$E_P$	$E_A$	$E_V$	$E_{FD}$	$E_{KE}$	$E_W$	$E_{TOTAL}$
$\epsilon_0$	0.0	0.0	0.0	0.0	0.0	1.6	0.0	1.6
$\epsilon_{0.004}$	4.5	0.3	0.1	0.1	0.8	7.4	11.6	1.6
$\epsilon_{0.015}$	26.5	14.8	0.4	0.1	3.0	4.6	48.0	1.6
$\epsilon_{0.05}$	27.9	121.3	1.1	0.2	17.5	4.2	170.7	1.6
$\epsilon_{0.1}$	35.0	288.4	2.1	1.5	31.0	2.9	358.3	1.6
$\epsilon_{0.2}$	32.3	614.1	3.7	7.9	34.6	3.1	684.8	1.6
$\epsilon_{0.5}$	38.3	1625.3	9.1	71.9	53.8	6.5	1711.9	1.7
$\epsilon_{0.75}$	41.5	2576.4	15.4	157.5	74.9	7.5	2674.4	1.6
$\epsilon_d$	47.5	3048.5	18.2	237.1	104.0	6.2	3158.3	1.5

Table B.3: Energy values in milijoules of the base chiral model at different strains

The total energy is conserved with small errors in Tables B.1, B.2, and B.3. Most of the work applied to the structures appears as plastic dissipated energy. The entire structure has undergone plastic deformation at high strain values. When looking at the kinetic energy values, there is initial kinetic energy in all models, and its value is 1.6 milijoules. Initial kinetic energy is the kinetic energy of the upper plate. The weight of the upper plate is 0.648 gr, its speed is 2.23 m/s. Accordingly, its kinetic



energy is calculated as 1.6 milijoules according to  $E_{KE} = 0.5mv^2$ .

The calculation of SEA is given in Section 3.3.1, but it can also be calculated from the energy results. The sum of the elastic dissipated, inelastic dissipated, viscous dissipated, and frictional dissipated energies in the locking strain of the models represents the absorbed part of the work applied to the structure. SEA is calculated by dividing the sum of the dissipated energies by the weight. The SEA value of the base hexagonal model is 0.89 kJ/kg when calculated from the stress output, and 0.89 kJ/kg is calculated from the energies. The SEA value of the base re-entrant structure is 0.56 kJ/kg when calculated from the stress and 0.57 kJ/kg when calculated from the energies. The SEA calculation for the base chiral model is 0.74 kJ/kg from the stress diagram and 0.82 kJ/kg from the energy. While almost identical values were calculated for the hexagon and re-entrant base models with the two methods, similar SEA values were calculated with a small error for the base chiral model. After finding the locking strain, both approaches can be preferred.



## Appendix C

### COMPUTATION OF POISSON RATIO FROM AREA AND AREA CHANGE OF DEFORMED SHAPE FOR THE PARAMETRIC HEXAGONAL STUDY

In this section, an alternative method for the computation of Poisson's ratio is presented. In the alternative method, displacements of all side boundary points of the lattice are used. To get all points on the lattice, black and white pixels in the images were separated with a code written in Matlab. Black pixels define the lattice geometry. Figure C.1 gives the undeformed hexagonal base model taken from ABAQUS and the image defined in Matlab. The red dots in Figure C.1b indicate the entire lattice geometry, and the blue dots indicate the points on the side boundaries of the lattice. As the lattice is compressed, the images are processed in Matlab, and the area change is calculated. Figure C.2 shows the base hexagonal model compressed by 0.2 strain taken from ABAQUS and processed in Matlab.

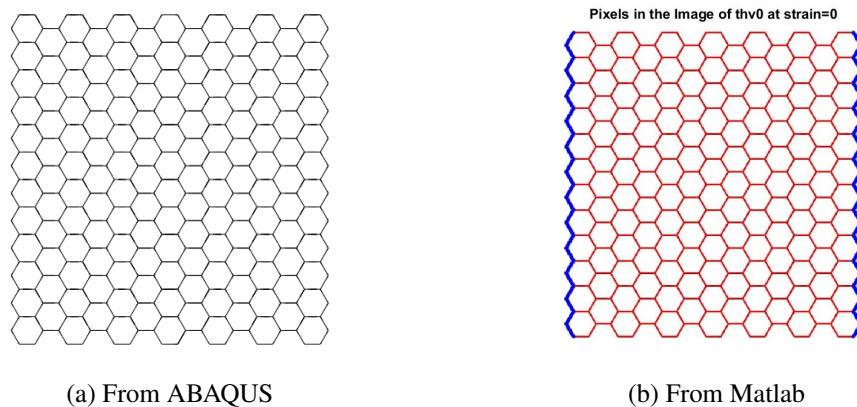


Figure C.1: Undeformed base hexagonal lattice

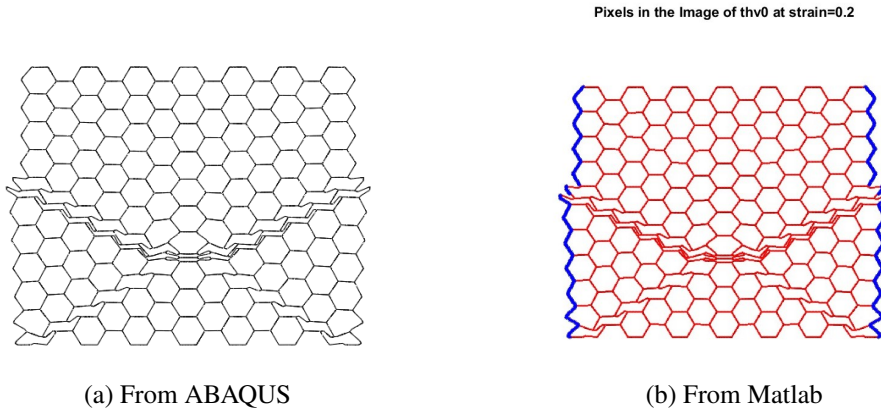


Figure C.2: Base hexagonal lattice compressed by 0.2 strain

While creating points on the lattice from pixels in Matlab, coordinate information of the points is also stored. Areas of structures can be calculated from these coordinates. Area change can be calculated from the computed areas at each strain value. Poisson's ratio can be calculated from the area changes by following the flow below. The geometrical parameters of the equations are given in Figure C.3.  $A_0$  is the initial area,  $A$  is the deformed area of the structure.  $\delta_x$  and  $\delta_y$  are displacements,  $L_{0x}$  and  $L_{0y}$  are initial lengths,  $L_x$  and  $L_y$  are deformed lengths in the x and y directions, respectively.

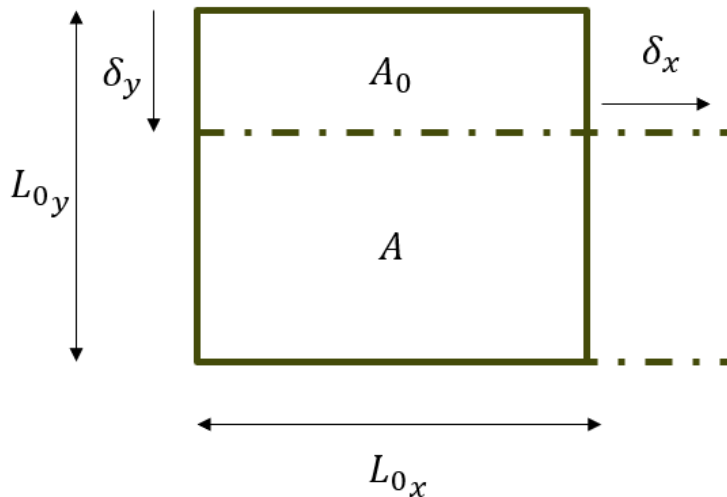


Figure C.3: Geometric parameters related with the initial and deformed structure

$$\nu_{yx} = -\frac{\epsilon_x}{\epsilon_y} \quad (C.1)$$

$$\epsilon_x = \frac{\delta_x}{L_{0x}} \quad (C.2)$$

$$\epsilon_y = \frac{\delta_y}{L_{0y}} \quad (C.3)$$

$$A_0 = L_{0y}L_{0x} \quad (C.4)$$

$$A = (L_{0x} + \delta_x)(L_{0y} + \delta_y) \quad (C.5)$$

$$A - A_0 = \delta_x L_{0y} + \delta_y L_{0x} + \delta_x \delta_y = \epsilon_x L_{0x} L_{0y} + \epsilon_y L_{0y} L_{0x} + \epsilon_x L_{0x} \epsilon_y L_{0x} \quad (C.6)$$

$$\Delta A = A - A_0 = L_{0x} L_{0y} (\epsilon_x + \epsilon_y + \epsilon_x \epsilon_y) = A \epsilon_y + A \epsilon_x (1 + \epsilon_y) \quad (C.7)$$

$$\Delta A - A \epsilon_y = A \epsilon_x (1 + \epsilon_y) \quad (C.8)$$

$$\epsilon_x = \frac{\Delta A - A \epsilon_y}{A(1 + \epsilon_y)} \quad (C.9)$$

$$\nu_{xy} = \frac{\Delta A - A \epsilon_y}{A \epsilon_y (1 + \epsilon_y)} \quad (C.10)$$

From Equation (C.10), Poisson ratio results for hexagonal lattice are given in Tables C.1-C.5. Poisson's ratios in Table A.1-A.5 are computed using forty-seven points. When the Poisson's ratio is calculated using all side boundary points, similar results are obtained.

Thickness of Sections (mm)			Poisson's ratio	Poisson's ratio	Poisson's ratio	Poisson's ratio
Base	Horizontal	Inclined	at strain 0.004	at strain 0.015	at strain 0.05	at strain 0.1
0.3	0.35	0.2758	1.711	0.985	0.687	0.439
0.3	0.3	0.3	0.936	0.883	0.703	0.452
0.3	0.25	0.3242	0.857	0.866	0.675	0.439
0.3	0.2	0.3484	0.800	0.849	0.621	0.335
0.3	0.15	0.3726	0.776	0.821	0.517	0.263
0.3	0.125	0.4588	0.744	0.793	0.464	0.226
0.3	0.1	0.3968	0.731	0.657	0.113	0.058
0.3	0.075	0.4830	0.692	0.298	-0.105	-0.064
0.3	0.05	0.4951	0.628	0.133	0.027	-0.125
0.3	0.025	0.5072	0.434	-0.156	-0.444	-1.207
0.3	0.01	0.4403	0.225	-0.579	-1.594	-2.511
0.3	0.0075	0.5157	0.189	-0.559	-1.711	-2.530
0.3	0.005	0.4427	0.178	-0.258	-1.434	-2.246
0.3	0.001	0.4464	0.124	-0.071	-0.611	-1.315

Table C.1: Poisson's ratio calculation from area change for the models of the first parametric study of the hexagonal lattice

Thickness of Sections (mm)			Poisson's ratio	Poisson's ratio	Poisson's ratio	Poisson's ratio
Base	Hexagonal	Additional	at strain 0.004	at strain 0.015	at strain 0.05	at strain 0.1
0.3	0.300	0	1.711	0.985	0.687	0.439
0.3	0.299	0.001	1.622	0.976	0.676	0.433
0.3	0.297	0.005	0.781	0.868	0.670	0.437
0.3	0.293	0.01	0.699	0.857	0.680	0.409
0.3	0.267	0.05	0.594	0.722	0.411	0.177
0.3	0.251	0.075	0.531	0.645	0.343	0.116
0.3	0.234	0.1	0.441	0.240	0.071	0.037
0.3	0.226	0.1125	0.265	-0.200	-0.369	-0.234
0.3	0.218	0.125	0.104	-0.052	-0.030	-0.014
0.3	0.210	0.1375	0.046	-0.056	-0.052	-0.043
0.3	0.202	0.15	0.002	-0.097	-0.056	-0.057
0.3	0.185	0.175	-0.018	-0.096	-0.089	-0.052
0.3	0.169	0.2	-0.026	-0.089	-0.086	-0.101
0.3	0.136	0.25	-0.019	-0.050	-0.063	-0.073
0.3	0.103	0.3	-0.050	-0.041	-0.090	-0.126
0.3	0.037	0.4	-0.043	-0.020	-0.049	-0.030

Table C.2: Poisson's ratio calculation from area change for the models of the second parametric study of the hexagonal lattice

Thickness of Sections (mm)			Poisson's ratio	Poisson's ratio	Poisson's ratio	Poisson's ratio
Base	Hexagonal	Additional	at strain 0.004	at strain 0.015	at strain 0.05	at strain 0.1
0.3	0.300	0	1.711	0.985	0.687	0.439
0.3	0.299	0.001	1.709	0.983	0.683	0.438
0.3	0.297	0.005	0.885	0.873	0.677	0.440
0.3	0.294	0.01	0.881	0.873	0.674	0.438
0.3	0.272	0.05	0.759	0.875	0.694	0.472
0.3	0.243	0.1	0.760	0.808	0.627	0.444
0.3	0.215	0.15	0.680	0.434	0.251	0.136
0.3	0.186	0.2	0.623	0.340	0.143	0.108
0.3	0.158	0.25	0.660	0.278	0.075	0.071
0.3	0.129	0.3	0.603	0.271	-0.012	-0.019
0.3	0.073	0.4	0.613	-0.319	-1.051	-1.516
0.3	0.044	0.45	0.611	-1.305	-2.370	-2.692
0.3	0.030	0.475	0.453	-1.385	-3.053	-3.177
0.3	0.016	0.5	0.302	-1.744	-3.433	-3.663
0.3	0.002	0.525	0.058	-0.375	-1.568	-2.071
0.3	0.001	0.526	0.064	-0.338	-1.412	-1.920

Table C.3: Poisson's ratio calculation from area change for the models of the third parametric study of the hexagonal lattice

Angle (Degree)	Thickness (mm)	Relative Density	Poisson's ratio at strain 0.004	Poisson's ratio at strain 0.015	Poisson's ratio at strain 0.05	Poisson's ratio at strain 0.1
120	0.300	0.0693	1.711	0.985	0.687	0.439
115	0.300	0.0698	1.166	1.141	0.831	0.529
110	0.300	0.0714	1.570	1.500	1.107	0.677
105	0.300	0.0740	2.088	1.938	1.414	0.912
100	0.300	0.0779	3.288	2.523	1.518	0.871
97.5	0.300	0.0803	4.235	2.831	1.616	0.921
95	0.300	0.0831	4.975	3.285	1.655	1.014
93	0.300	0.0856	4.451	3.473	1.690	0.991
91	0.300	0.0885	3.194	1.318	0.509	0.204
90	0.300	0.0900	-0.624	-0.271	-0.026	-0.004
89	0.300	0.0916	-3.827	-2.019	-0.893	-0.284
87	0.300	0.0951	-5.072	-3.499	-1.841	-1.216
85	0.300	0.0990	-5.944	-3.710	-2.092	-1.690
82.5	0.300	0.1044	-5.409	-3.358	-2.319	-1.853
80	0.300	0.1106	-4.686	-3.347	-2.428	-1.845
75	0.300	0.1257	-3.579	-3.126	-2.664	-2.009
70	0.300	0.1456	-6.069	-3.251	-2.741	-1.611

Table C.4: Poisson's ratio calculation from area change for the models of the fourth parametric study of the hexagonal lattice

Angle (Degree)	Thickness (mm)	Relative Density	Poisson's ratio at strain 0.004	Poisson's ratio at strain 0.015	Poisson's ratio at strain 0.05	Poisson's ratio at strain 0.1
120	0.300	0.0693	1.711	0.985	0.687	0.439
115	0.298	0.0693	1.160	1.138	0.846	0.536
110	0.291	0.0693	1.525	1.557	1.136	0.710
105	0.281	0.0693	2.027	1.921	1.445	0.981
100	0.267	0.0693	3.067	2.825	1.662	0.965
97.5	0.259	0.0693	4.045	3.098	1.806	1.026
95	0.250	0.0693	4.425	3.385	1.857	1.111
93	0.243	0.0693	4.259	3.665	1.917	1.337
91	0.235	0.0693	3.124	1.681	0.645	0.253
90	0.231	0.0693	-1.473	0.172	0.099	0.058
89	0.227	0.0693	-3.503	-1.827	-0.755	-0.262
87	0.219	0.0693	-4.749	-4.618	-2.564	-1.697
85	0.210	0.0693	-9.110	-4.586	-2.535	-1.889
82.5	0.199	0.0693	-4.923	-3.554	-2.350	-1.842
80	0.188	0.0693	-7.490	-3.933	-2.391	-1.861
75	0.165	0.0693	-6.043	-3.622	-2.501	-1.992
70	0.143	0.0693	-4.847	-3.379	-2.482	-1.622

Table C.5: Poisson's ratio calculation from area change for the models of the fifth parametric study of the hexagonal lattice

The hexagonal model's first and fourth parametric studies are presented to determine whether there is a relationship between SEA and area change. Area change is the difference between the area of the deformed structure and the undeformed structure,

and it is formulated in Equation (C.7). In Table C.6, the area change values of the first parametric study are given, and the areas of the models decreased in all strain values. The area change is directly proportional to Poisson's ratios given in Table C.1. When Poisson's ratio is around 1, there seems to be no area change, but the area decreases as Poisson's ratio values decrease. The fourth parametric study of the hexagonal lattice in Table C.7 revealed that the areas of models with an angle larger than  $90^\circ$  increased, and the areas of models smaller than  $90^\circ$  decreased. The size of the area change is again directly proportional to the Poisson's ratios given in Table C.4. Similar comments can be made as before. In other words, the area change of the lattice structures is directly proportional to Poisson's ratio. If Poisson's ratio is greater than 1, the area becomes larger; if it is smaller, the area becomes smaller.

Thickness of Sections (mm)			SEA (kj/kg)	Area Change	Area Change	Area Change	Area Change
Base	Horizontal	Inclined		at strain 0.004	at strain 0.015	at strain 0.05	at strain 0.1
0.3	0.35	0.2758	0.74	0.002	-0.001	-0.016	-0.055
0.3	0.3	0.3	0.89	0.000	-0.003	-0.015	-0.054
0.3	0.25	0.3242	1.11	-0.001	-0.003	-0.017	-0.055
0.3	0.2	0.3484	1.20	-0.001	-0.003	-0.019	-0.064
0.3	0.15	0.3726	1.28	-0.001	-0.004	-0.024	-0.069
0.3	0.125	0.4588	1.33	-0.001	-0.004	-0.026	-0.073
0.3	0.1	0.3968	1.18	-0.001	-0.007	-0.042	-0.087
0.3	0.075	0.4830	1.06	-0.002	-0.014	-0.052	-0.097
0.3	0.05	0.4951	0.83	-0.002	-0.017	-0.046	-0.102
0.3	0.025	0.5072	0.84	-0.003	-0.023	-0.067	-0.192
0.3	0.01	0.4403	0.72	-0.004	-0.031	-0.118	-0.300
0.3	0.0075	0.5157	0.67	-0.004	-0.031	-0.123	-0.301
0.3	0.005	0.4427	0.47	-0.004	-0.025	-0.111	-0.278
0.3	0.001	0.4464	0.39	-0.004	-0.018	-0.074	-0.201

Table C.6: Area changes for 0.004, 0.015, 0.05, and 0.1 strains of the first parametric study of the hexagonal lattice



Angle (Degree)	Thickness (mm)	Relative Density	SEA (kJ/kg)	Area Change at strain 0.004	Area Change at strain 0.015	Area Change at strain 0.05	Area Change at strain 0.1
120	0.300	0.0693	0.89	0.002	-0.001	-0.016	-0.055
115	0.300	0.0698	1.04	0.001	0.002	-0.010	-0.049
110	0.300	0.0714	1.17	0.003	0.009	0.003	-0.035
105	0.300	0.0740	1.17	0.005	0.018	0.016	-0.016
100	0.300	0.0779	1.43	0.011	0.029	0.021	-0.019
97.5	0.300	0.0803	1.37	0.016	0.035	0.025	-0.015
95	0.300	0.0831	1.41	0.020	0.044	0.028	-0.008
93	0.300	0.0856	1.40	0.017	0.048	0.030	-0.009
91	0.300	0.0885	1.50	0.011	0.006	-0.025	-0.074
90	0.300	0.0900	1.43	-0.008	-0.022	-0.048	-0.092
89	0.300	0.0916	1.47	-0.024	-0.052	-0.087	-0.115
87	0.300	0.0951	1.40	-0.030	-0.088	-0.136	-0.192
85	0.300	0.0990	1.47	-0.034	-0.092	-0.148	-0.237
82.5	0.300	0.1044	1.25	-0.032	-0.085	-0.151	-0.245
80	0.300	0.1106	0.87	-0.028	-0.085	-0.155	-0.245
75	0.300	0.1257	1.18	-0.023	-0.080	-0.166	-0.258
70	0.300	0.1456	0.99	-0.018	-0.073	-0.170	-0.226

Table C.7: Area changes for 0.004, 0.015, 0.05, and 0.1 strains of the fourth parametric study of the hexagonal lattice



## Appendix D

### EFFECT OF FRICTION COEFFICIENT ON PLATEAU STRESS AND SEA FOR HEXAGONAL BASE MODEL

In all parametric studies conducted within the scope of the thesis, it is stated in Section 3.2.1 that the friction coefficient is taken as 0.3. The increase in the friction coefficient is expected to increase the stress on the structure because extra forces arise due to the contact of the surfaces. The analyses were repeated in the base hexagonal model for the three additional friction coefficients. Except for 0.3, the friction coefficients were selected as 0.0, 0.6, and 1.0. The plateau stress and SEA results of the analyses are shown in Table D.1. The energy absorption value, which is 0.824 kJ/kg when the friction coefficient is 0.0, increased to 0.887 kJ/kg at the friction coefficient of 0.3 and 1.075 at 0.6. However, when the friction coefficient is 1.0, the SEA is slightly lower than 0.6. The plateau stress values of the models with 0.6 and 1.0 friction coefficients were 0.25 MPa. The SEA is found to be lower in the model with a 1.0 friction coefficient because the gap between the locking strain and critical strain is smaller. It can be concluded that the increase in the friction coefficient leads to larger SEA values up to a particular value beyond which SEA decreases.

Friction Coefficient	Plateau Stress (MPa)	SEA (kJ/kg)
0	0.1914	0.8235
0.3	0.2082	0.8873
0.6	0.2502	1.0751
1	0.2502	1.0654

Table D.1: Effect of friction coefficient on Plateau Stress and SEA in hexagonal base model



## Appendix E

### ELASTIC POISSON'S RATIOS OF UNIT CELLS

Analytical elastic Poisson's ratio of the hexagonal unit cell is given in [19] as:

$$\nu = \frac{\cos^2\theta}{(h/l + \sin\theta)\sin\theta}, \quad (\text{E.1})$$

where  $\theta$  is the unit angle,  $h$  is the horizontal edges,  $l$  is the inclined edges. In the parametric studies, edge lengths are constant at 5 mm, and  $h$  equals  $l$ . So, Equation (E.1) only depends on  $\theta$  and is calculated in the second column of Table E.2. In addition, unit cell compression analysis was performed for three randomly selected angles. Unit cell analyses were completed with ABAQUS/Implicit with 0.005 strain. The figure below shows the displacement of the 120° hexagonal unit cell under 0.005 strain. When calculating Poisson, the strain calculated from the displacements of the two extreme points in the vertical direction was divided by 0.005. Results for 120°, 105°, and 70° unit cell compression are given in the third column of Table E.2, also the y-displacement contour of the deformed hexagonal unit cell with undeformed geometry is shown in Figure E.1. A compression strain of 0.005 is determined to stay in the elastic region. From Table E.2, analytical Poisson's ratio and Poisson's ratio from unit cell analysis are consistent. According to Table A.4 and Table E.2, the strain value for the hexagonal lattice at which it can be assumed that the entire structure remains in the elastic region is 0.015.

Angle (Degree)	Analytical Poisson's Ratio	Unit Cell Poisson's Ratio
120	1.000	0.980
115	1.366	
110	1.924	
105	2.864	2.630
100	4.759	
97.5	6.661	
95	10.474	
93	18.107	
91	56.299	
90	-	
89	-58.299	
87	-20.107	
85	-12.474	
82.5	-8.661	
80	-6.759	
75	-4.864	
70	-3.924	-3.740

Table E.1: Analytical elastic Poisson's ratio and Poisson's ratio from unit cell analyses for hexagonal shape

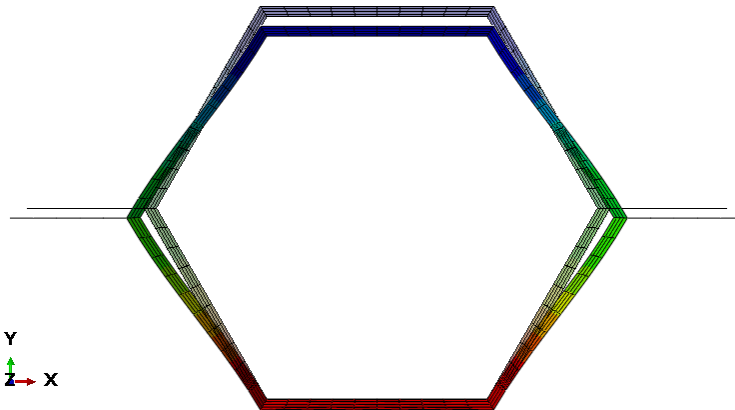


Figure E.1: Undeformed and deformed hexagonal unit cell at 0.005 strain

Analytical elastic Poisson's ratio of the re-entrant unit cell is calculated in [25] as:

$$\nu = \frac{h \sin^2 \theta}{(l - h \cos \theta) \sin \theta}, \quad (\text{E.2})$$

where  $\theta$  is the unit angle, again, but  $h$  is the inclined edges,  $l$  is the horizontal edges. In the parametric studies,  $h$  and  $l$  are also constant values for re-entrant unit cells.  $h$  is 5 mm, and  $l$  is 10 mm for the re-entrant configuration. Equation E.2 is calculated in Table E.2. A similar unit cell study is conducted for re-entrant lattice; results are

given in the third column of Table E.2, and the deformed shape is shown in Figure E.2. The results of analytical calculations and unit cell study are consistent. From Table A.9 and Table E.2, elastic region strain can be selected as 0.015.

Angle (Degree)	Analytical Poisson's Ratio	Unit Cell Poisson's Ratio
60	-1.000	-1.000
65	-1.232	
70	-1.557	
75	-2.070	-1.940
80	-3.058	
82.5	-4.028	
85	-5.953	
87	-9.784	
89	-28.893	
90	-	0.005
91	28.393	
93	9.285	
95	5.456	
97.5	3.535	
100	2.569	
105	1.596	1.490
110	1.102	
115	0.802	
120	0.600	0.590

Table E.2: Analytical elastic Poisson's ratio and Poisson's ratio from unit cell analyses for hexagonal shape

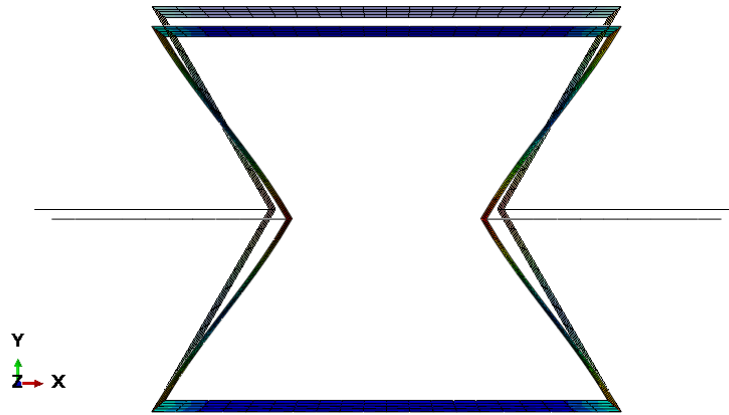


Figure E.2: Undeformed and deformed re-entrant unit cell at 0.005 strain

No analytical Poisson's ratio calculation is found in the literature for the chiral unit cell, but compression analyses are performed on the unit cell with a strain of 0.005 for six different angles. The analysis results are shown in Table E.3, and the visuals of the deformed and undeformed structures are shown in Figure E.3. From Table A.14 and Table E.3, to use the same value as the hexagonal and re-entrant cells, 0.015 strain can be used for the chiral lattice.

Angle (Degree)	Unit Cell Poisson's Ratio
105	0.726
135	0.710
155	0.654
170	0.430
180	0.001
225	0.710

Table E.3: Poisson's ratio from unit cell analyses for chiral shape



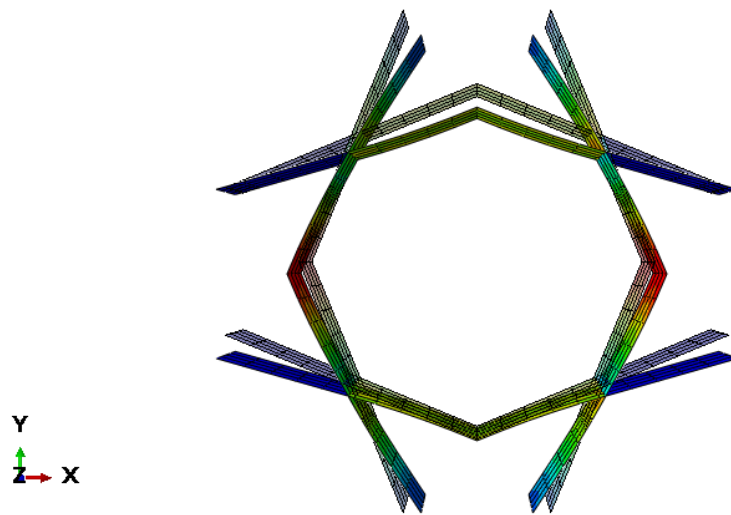


Figure E.3: Undeformed and deformed chiral unit cell at 0.005 strain



## Appendix F

### COMPARISON OF EXPLICIT AND IMPLICIT ANALYZES FOR BASE HEXAGONAL MODEL

In this section, a comparison of implicit and explicit solutions analyzed at small strain values of the hexagonal base model is given. Since it becomes difficult to perform implicit analysis as the strain value increases, comparing the strain values of 0.02, 0.04, 0.16, and 0.2 is sufficient. The geometries, mesh properties, and boundary conditions were applied in the same way in both solution methods. The reaction force on the upper plate is given in Table F.1. Since the plate moves downwards, the forces are negative. In the fourth column of the table, the difference between the explicit analysis and the implicit analysis is given. The difference of explicit solution is slightly high at 0.04 and 0.2 strain values, and the difference is negligible for 0.02 and 0.16. It clearly shows that the explicit analysis has adequate performance.

Strain	Reaction Force at Upper Surfaces (N)		Absolute Difference (N)	Difference in Percentage
	Implicit	Explicit		
0.02	-47.24	-49.80	2.56	5%
0.04	-41.79	-35.62	6.17	15%
0.16	-35.44	-35.81	0.37	1%
0.20	-34.40	-28.90	5.50	16%

Table F.1: Explicit and implicit analyzes results for the hexagonal base model at 0.02, 0.04, 0.16, and 0.2 strains



## Appendix G

### ILLUSTRATION OF SOME DEFORMED HEXAGONAL LATTICES

This chapter provides the deformed geometries of the hexagonal lattice under 0.2 and 0.5 strains of the two models in each of the five parametric studies. First, the undeformed hexagonal lattice is shown in Figure 3.8. The deformed geometries of the base hexagonal model are given in Figure G.1. While some models of other deformed geometries are stacked on each other, it can be seen that some models are not compressed stably. These models are models where the edge thickness changes are extreme. When the thickness changes reach extreme points, the load-carrying capacity of the structure decreases significantly. At the angle change studies, it is seen that the  $90^\circ$  models are compressed by deformation from the upper boundary, while there is buckling in models whose angle is far from  $90^\circ$ . Compression behavior is one of the reasons why the SEA is high at around  $90^\circ$  and a specific thickness variation.

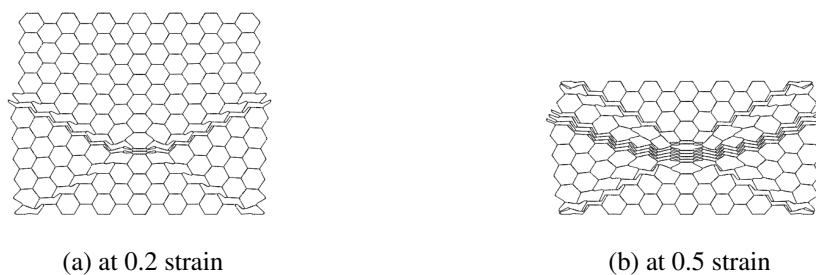
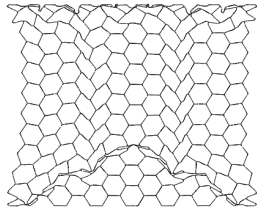
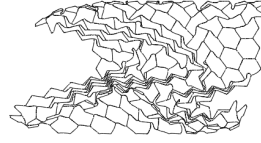


Figure G.1: Deformed geometry of the base hexagonal lattice

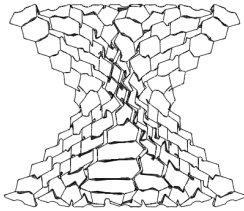


(a) at 0.2 strain

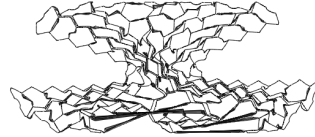


(b) at 0.5 strain

Figure G.2: Deformed geometry of hexagonal lattice of the first parametric study with the inclined edge thickness of 0.397 mm

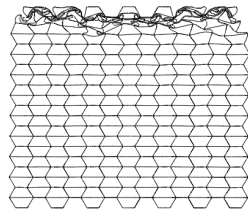


(a) at 0.2 strain

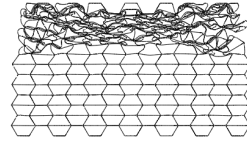


(b) at 0.5 strain

Figure G.3: Deformed geometry of hexagonal lattice of the first parametric study with the inclined edge thickness of 0.446 mm

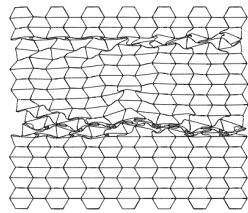


(a) at 0.2 strain

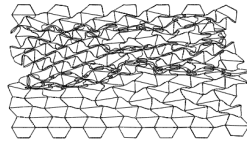


(b) at 0.5 strain

Figure G.4: Deformed geometry of hexagonal lattice of the second parametric study with the additional edge thickness of 0.1 mm

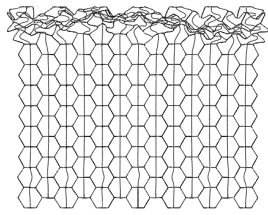


(a) at 0.2 strain

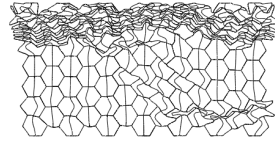


(b) at 0.5 strain

Figure G.5: Deformed geometry of hexagonal lattice of the second parametric study with the additional edge thickness of 0.25 mm

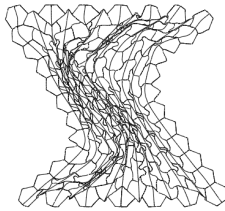


(a) at 0.2 strain

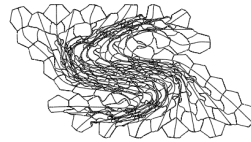


(b) at 0.5 strain

Figure G.6: Deformed geometry of hexagonal lattice of the third parametric study with the additional edge thickness of 0.15 mm



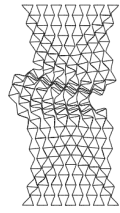
(a) at 0.2 strain



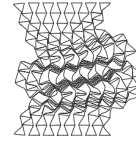
(b) at 0.5 strain

Figure G.7: Deformed geometry of hexagonal lattice of the third parametric study with the additional edge thickness of 0.475 mm



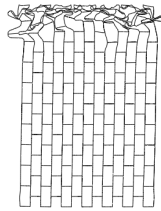


(a) at 0.2 strain

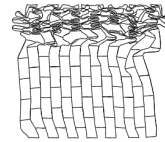


(b) at 0.5 strain

Figure G.8: Deformed geometry of hexagonal lattice of the fourth parametric study with the angle of  $70^\circ$

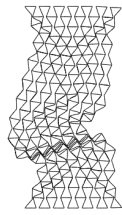


(a) at 0.2 strain

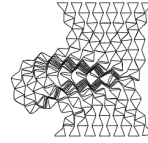


(b) at 0.5 strain

Figure G.9: Deformed geometry of hexagonal lattice of the fourth parametric study with the angle of  $90^\circ$

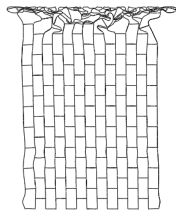


(a) at 0.2 strain

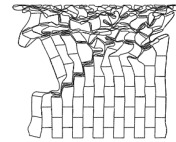


(b) at 0.5 strain

Figure G.10: Deformed geometry of hexagonal lattice of the fifth parametric study with the angle of  $70^\circ$



(a) at 0.2 strain



(b) at 0.5 strain

Figure G.11: Deformed geometry of hexagonal lattice of the fifth parametric study with the angle of  $90^\circ$